AdvSND
The Advanced Scattering and Neutrino Detector at High Lumi LHC

Letter of Intent

SND@LHC Collaboration

Abstract

The SND@LHC experiment has been taking data at the LHC since the beginning of Run 3. With the analysis of the data collected in 2022, the experiment has published the observation of collider muon neutrinos, thus paving the way for neutrino physics at the LHC. The results which will be obtained from Run 3 will provide the first measurement of neutrinos in an unprecedented energy range and will constrain the gluon Parton Distribution Function using neutrinos as a probe of charm production in an unexplored pseudo-rapidity domain. Nevertheless, the Run 3 measurements will be statistically limited, given the geometrical constraints of the current detector and the expected integrated luminosity. This document expresses the interest of the SND@LHC Collaboration to extend the physics reach of the LHC in the neutrino sector and proposes an upgrade of the detector to fully exploit the potential of the High Luminosity LHC (HL-LHC). The factor 5 increase of instantaneous luminosity foreseen by the HL-LHC is incompatible with the usage of nuclear emulsion films as the high-resolution tracking detector in the neutrino target region and we propose to replace them by silicon trackers. Along with the increase of statistical precision, we propose significant improvements of the experimental setup: we plan to add a magnetic spectrometer which would allow separate identification of neutrino and antineutrino interactions for both muon and tau neutrinos. In particular the addition of a magnetic spectrometer would allow the first experimental direct observation and the study of tau antineutrinos, while extending the range of flavour conservation tests. It will also extend the reach for the possible discovery of new exotic phenomena. The proposed modifications to the TII8 environment have two main justifications: the changes to the floor will enhance the acceptance of the detector, also in view of the possible changes in beam crossing angles, while the enlargement of the tunnel is needed to accommodate the magnetic spectrometer. As the feasibility of the tunnel enlargement is currently being investigated, we consider two versions of the upgraded detector, which we call *baseline* (including the magnetic spectrometer) and *minimal* (allowing only for the improved acceptance). The option of installing and running the upgraded detector in the current geometrical configuration, without performing any civil engineering work, was also examined.

The SND@LHC Collaboration

D. Abbaneo[9], R. Albanese[1,2], A. Alexandrov[1], F. Alicante[1,2], K. Androsov[6], A. Anokhina[3], T. Asada[1,2], C. Asawatangtrakuldee[38], M.A. Ayala Torres[32], C. Battilana[4,5], A. Bay[6], A. Bertocco[1,2], C. Bertone[9], C. Betancourt[7], D. Bick[8], R. Biswas[9], A. Blanco Castro[10], V. Boccia[1,2], M. Bogomilov[11], A. Boiano[1], D. Bonacorsi[4,5], W.M. Bonivento[12], P. Bordalo[10], A. Boyarsky[13,14], T. Bud[9], L. Buonocore[9], S. Buontempo[1], M. Campanelli[15], T. Camporesi[9], V. Canale[1,2], D. Centanni[1,16], F. Cerutti[9], M. Chernyavskiy[3], K.-Y. Choi[17], S. Cholak[6], F. Cindolo[4], M. Climescu[18], A.P. Conaboy[19], O. Crespo-Lopez[9], G.M. Dallavalle[4], D. Davino[1,20], P.T. de Bryas[6], G. De Lellis[1,2], M. De Magistris[1,16], A. De Roeck[9], A. De Rújula[9], D. De Simone[7], A. Di Crescenzo[1,2], D. Di Ferdinando[4], S. Di Luca[9], P. Di Meo[1], C. Dinc[23], R. Donà[4,5], O. Durhan[23], F. Fabbri[4], F. Fedotovs[15], M. Ferrillo[7], A. Fiorillo[1,2], R. Fresa[1,24], W. Funk[9], C. Gaignant[9], F.M. Garay Walls[25], A. Golovatiuk[1,2], A. Golutvin[26], E. Graverini[6,41], L. Guiducci[4,5], A.M. Guler[23], V. Guliaeva[3], G.J. Haefeli[6], C. Hagner[8], J.C. Helo Herrera[27,40], A. Herty[9], E. van Herwijnen[26], P. Iengo[1], S. Ilieva[1,2,11], A. Infantino[9], A. Iuliano[1,2], R. Jacobsson[9], H. Jeangros[9], C. Kamiscioglu[23,28], A.M. Kauniskangas[6], E. Khalikov[3], S.H. Kim[29], Y.G. Kim[30], G. Klioutchnikov[9], M. Komatsu[31], N. Konovalova[3], S. Kuleshov[27,32], L.Krzempek[1,2,9], H.M. Lacker[19], O. Lantwin[1], F. Lasagni Manghi[4], A. Lauria[1,2], K.Y. Lee[29], K.S. Lee[33], P. Lelong[9], G. Lerner[9], S. Lo Meo[4], V.P. Loschiavo[1,20], S. Marcellini[4], A. Margiotta[4,5], A.-P. Marion[9], A. Mascellani[6], F. Mei[5], A. Miano[1,2], A. Mikulenko[13], M.C. Montesi[1,2], F.L. Navarria[4,5], W. Nuntiyakul[39], S. Ogawa[34], N. Okateva[3], J. Osborne[9], M. Ovchynnikov[13], G. Paggi[4,5], K. Pal[9], J. Panigoni[9], B.D. Park[29], G. Passeggio[1], J. Pazzini[42,43,44,45], S. Pelletier[9], M. Perez Ornedo[42], A. Perrotta[4], D. Podgrudkov[3], N. Polukhina[3], A. Prota[1,2], O. Prouteau[9], A. Quercia[1,2], S. Ramos[10], A. Reghunath[19], T. Roganova[3], F. Ronchetti[6], L. Rottoli[9], T. Rovelli[4,5], O. Ruchayskiy[35], T. Ruf[9], M. Sabate Gilarte[9], Z. Sadykov[1], M. Samoilov[3], F. Sanchez Galan[9], V. Scalera[1,16], W. Schmidt-Parzefall[8], O. Schneider[6], G. Sekhniaidze[1], N. Serra[7], M. Shaposhnikov[6], V. Shevchenko[3], T. Shchedrina[3], L. Shchutska[6], H. Shibuya[34,36], G.P. Siroli[4,5], G. Sirri[4], G. Soares[10], J.Y. Sohn[29], O.J. Soto Sandoval[27,40], M. Spurio[4,5], N. Starkov[3], J. Steggemann[6], M. Szewczyk[9], I. Timiryasov[35], V. Tioukov[1], F. Tramontano[1,2,9], C. Trippl[6], A. Uluwita[9], E. Ursov[19], A. Ustyuzhanin[1,37], G. Vankova-Kirilova[11], G. Vasquez[7], C. Vendeuvre[9], V. Verguilov[11], N. Viegas Guerreiro Leonardo[10], C. Vilela[10], C. Visone[1,2], R. Wanke[18], E. Yaman[23], Z. Yang[6], C. Yazici[23], C.S. Yoon[29], E. Zaffaroni[6], J. Zamora Saa[27,32], M. Zanetti[42,43]

[1]Sezione INFN di Napoli, Napoli, 80126, Italy

[2]Università di Napoli "Federico II", Napoli, 80126, Italy

[3]Affiliated with an institute covered by a cooperation agreement with CERN

[4]Sezione INFN di Bologna, Bologna, 40127, Italy

[5]Università di Bologna, Bologna, 40127, Italy

[6]Institute of Physics, EPFL, Lausanne, 1015, Switzerland

[7]Physik-Institut, UZH, Zürich, 8057, Switzerland

[8]Hamburg University, Hamburg, 22761, Germany

[9]European Organization for Nuclear Research (CERN), Geneva, 1211, Switzerland

[10]Laboratory of Instrumentation and Experimental Particle Physics (LIP), Lisbon, 1649-003, Portugal

[11]Faculty of Physics,Sofia University, Sofia, 1164, Bulgaria

[12]Università degli Studi di Cagliari, Cagliari, 09124, Italy

[13]University of Leiden, Leiden, 2300RA, The Netherlands

[14]Taras Shevchenko National University of Kyiv, Kyiv, 01033, Ukraine

[15]University College London, London, WC1E6BT, United Kingdom

[16]Università di Napoli Parthenope, Napoli, 80143, Italy

[17]Sungkyunkwan University, Suwon-si, 16419, Korea

[18]Institut für Physik and PRISMA Cluster of Excellence, Mainz, 55099, Germany

[19]Humboldt-Universität zu Berlin, Berlin, 12489, Germany

[20]Università del Sannio, Benevento, 82100, Italy

[21]Sezione INFN di Bari, Bari, 70126, Italy

[22]Università di Bari, Bari, 70126, Italy

[23]Middle East Technical University (METU), Ankara, 06800, Turkey

[24]Università della Basilicata, Potenza, 85100, Italy

[25]Departamento de Física, Pontificia Universidad Católica de Chile, Santiago, 4860, Chili

[26]Imperial College London, London, SW72AZ, United Kingdom

[27]Millennium Institute for Subatomic physics at high energy frontier-SAPHIR, Santiago, 7591538, Chile

[28]Ankara University, Ankara, 06100, Turkey

[29]Department of Physics Education and RINS, Gyeongsang National University, Jinju, 52828, Korea

[30]Gwangju National University of Education, Gwangju, 61204, Korea

[31]Nagoya University, Nagoya, 464-8602, Japan

[32]Center for Theoretical and Experimental Particle Physics, Facultad de Ciencias Exactas, Universidad Andrès Bello, Fernandez Concha 700, Santiago, Chile

[33]Korea University, Seoul, 02841, Korea

[34]Toho University, Chiba, 274-8510, Japan

[35]Niels Bohr Institute, Copenhagen, 2100, Denmark

[36]Present address: Faculty of Engineering, Kanagawa, 221-0802, Japan

[37]Constructor University, Bremen, 28759, Germany

[38]Chulalongkorn University, Bangkok, 10330, Thailand

[39]Chiang Mai University , Chiang Mai, 50200, Thailand

[40]Departamento de Física, Facultad de Ciencias, Universidad de La Serena, La Serena, 1200, Chile

[41]Also at: Università di Pisa, Pisa, 56126, Italy

[42]Università di Padova, Padova, 35122, Italy

[43]Sezione INFN di Padova, Padova, 35122, Italy

[44]Department of Engineering, Università di Padova, Padova, 35122, Italy

[45]Department of Information Engineering, Università di Padova, Padova, 35122, Italy

Contents

1 Motivation and overview of the AdvSND detector

The objective of the SND@LHC experiment [1] is the detection of high-energy neutrinos produced by the LHC to study neutrino properties and to probe charm production in the very forward region. The experiment was approved in 2021 and ready to take data in 2022. The adopted detector technology is hybrid which combines nuclear emulsions as a high resolution vertex detector with an electronic readout calorimeter and muon identification system. [2]. By using only the data taken with the electronic detectors in 2022, the SND@LHC Collaboration recently reported the observation of collider muon neutrinos [3], demonstrating the effectiveness of such compact detectors and paving the way for new physics studies with higher statistics.

At the same time, the measurement of the muon flux [4] provided an important validation of the very complex simulation of all the machine elements along the beam line from the interaction point to the TI18 tunnel. Remarkably, the agreement between data and simulation is within 25%. Moreover, it was an essential ingredient for the observation of neutrinos, since muon interactions are the origin of most background sources. The muon flux was also measured with emulsion films which confirmed the measurement carried out with electronic detectors.

These first results provide a clear picture of the signal and background environment for further exploitation of the neutrino physics potential at the LHC. The physics program in Run 3 will be statistically limited in most channels. The exploitation of the potential of the High Luminosity LHC (HL-LHC) with some key improvements will largely extend the physics reach of the experiment both in neutrino physics and in BSM searches.

With this Letter of Intent, the Collaboration proposes to extend the physics case of the experiment by upgrading the detector for running at the HL-LHC. The current SND@LHC detector exploits all the space available in the TI18 tunnel to cover the desired range in pseudo-rapidity, but its design in 2021 assumed that no civil engineering could be performed in time for operation in Run 3. The proposed upgrades are meant to improve the detector performance and to overcome the geometrical constraints imposed by the tunnel geometry and the sloping floor. Figure 1 shows a schema of AdvSND.

The measured muon rate sets the maximum achievable integrated luminosity at about 20 fb^{-1} for the reconstruction of emulsion data. This limit comes from the pile-up of muons which produce parallel tracks on average only about 10 micron apart from each other at the above-mentioned integrated luminosity. The alignment of consecutive films, which is required to follow the tracks along their path in the Target walls, is limited to this precision. As a consequence, five emulsion Targets were installed overall in 2022 and 2023 to collect about 70 fb^{-1}, with a maximum of 21 fb^{-1} integrated in one Target exposure.

With the HL-LHC operating at an expected instantaneous luminosity five times larger than the current SND@LHC will collect this integrated luminosity in approximately one week. The frequent replacement of emulsion films, even if financially manageable by the Collaboration, would require a correspondingly frequent stop of the machine to provide access, which is not compatible with an efficient operation of the LHC machine. For this reason, the use of an electronic readout technology as a high-precision vertex detector is envisaged.

The energy measurement and the muon identification determine the minimum length of the current detector. With the constraints from the tunnel and the sloping floor, this requirement competes with the azimuthal angular acceptance of the Target that determines the overall flux intercepted and therefore the total number of observed interactions. These effects limit the achievable mass of the Target to about 800 kg and have affected the performance of the
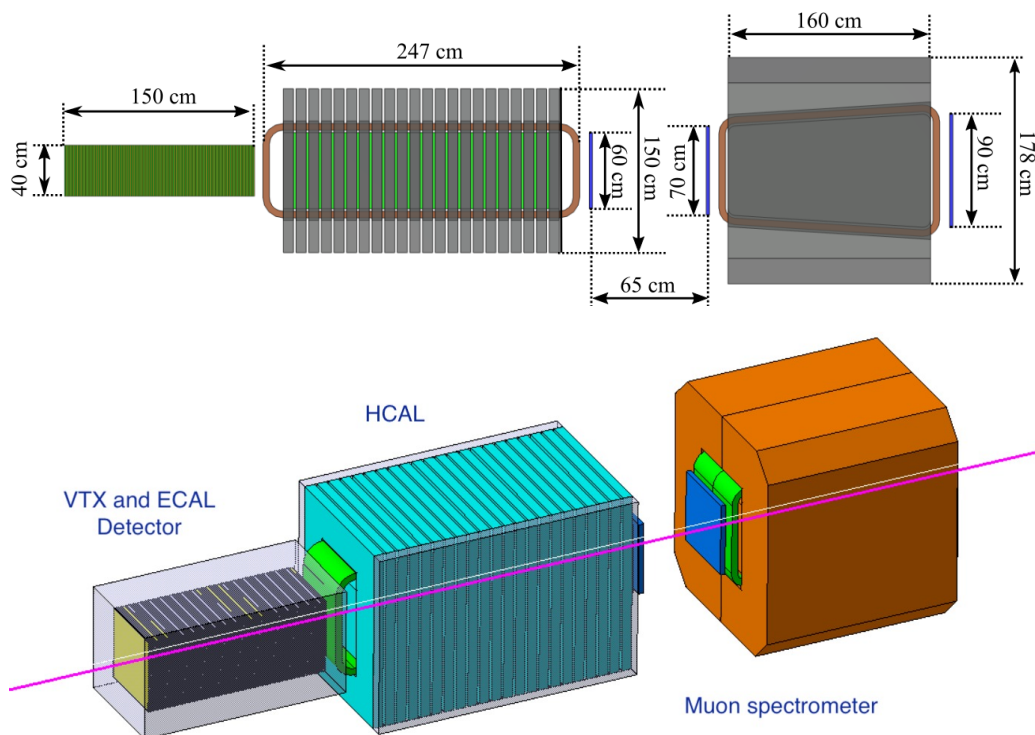
Figure 1: Outline of the proposed detector for AdvSND.

Veto system in the first two years of the run. Indeed, due to the sloping floor, the Veto does not cover the entire Target region, and it does not have any rejection power against charged particles entering the lower part of the Target, where the neutrino flux is higher. Recently the Collaboration has added a third Veto station and dug a small trench in order to cover the bottom part and increase the fiducial volume of the Target.

Presently the LHC operates with a vertical crossing angle of the beams in ATLAS of -160 μrad which defines the azimuthal acceptance of the detector (see Figure 2). The operation of the LHC in Run 4 foresees a crossing angle of the beam in the ATLAS interaction region which will be $+250$ μrad in the horizontal plane. This will affect the acceptance of the detector in its present position, further reducing its azimuthal coverage and enhancing the issues related to the sloping floor. For this reason we propose to excavate the floor to minimize the effect of the crossing angle foreseen in Run 4 and also mitigate the effect of a possible switch to a vertical crossing angle in Run 5: see Figures 3 and 4. More details on the proposed civil engineering modifications and physics reach are given in Sections 3 and 4 respectively.

The environment of TI18 did not permit the installation of a magnetic spectrometer. This limits the precision of the measurement of the neutrino energy and does not permit the separation of neutrinos from anti-neutrinos. We have studied the constraints of replacing the present Muon Tagger with a Spectrometer with adequate acceptance. Our baseline proposal for AdvSND contains a Magnetic Spectrometer which can be accommodated if the TI18 tunnel is enlarged to make space for the magnet. We have optimized the design of the magnet to minimize its dimensions. The proposed Spectrometer is based on an iron core magnet providing a magnetic field of 1.5 Tesla. The choice of iron core limits the power dissipation to $\sim$1kW. In addition, we propose to magnetize the Hadron Calorimeter (HCAL). This will constrain the
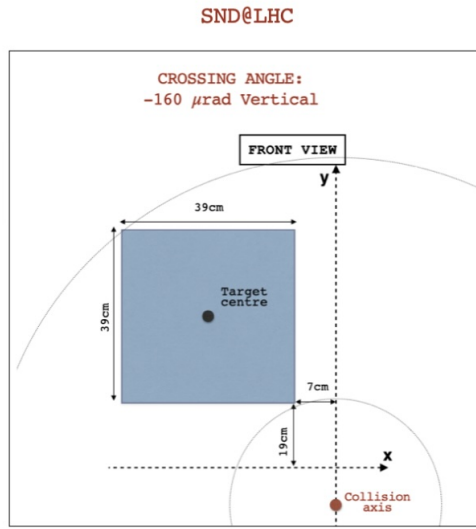
Figure 2: The current position of SND@LHC in Run 3 with an outline of the position of the luminous region with the vertical crossing angle in the ATLAS interaction point of $-160\,\mu$rad.
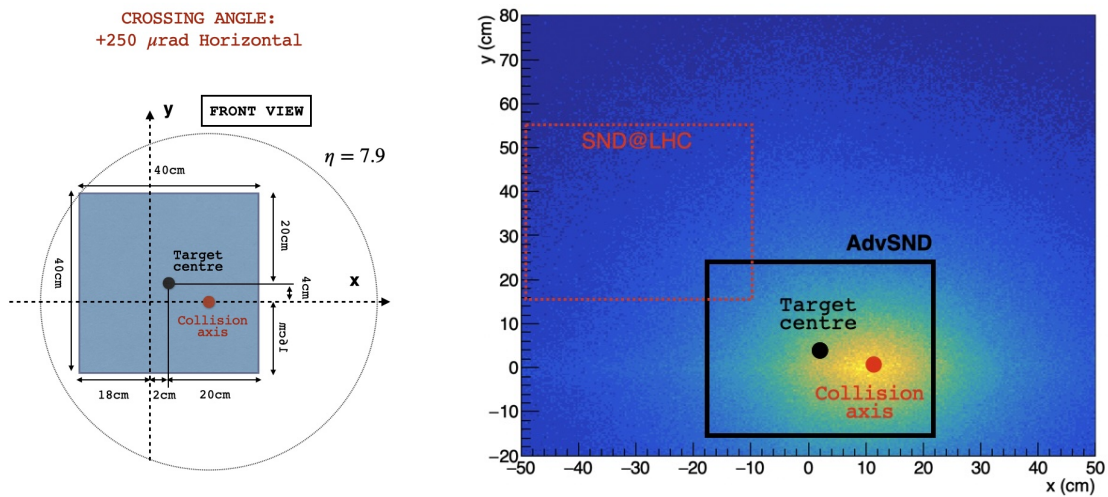

Figure 3: The proposed position of AdvSND. Left: Overlay with the collision axis. Right: Simulated distribution of ν_μ interactions with in the black square the proposed position of AdvSND and in the red-dashed square the present position of SND@LHC. Both left and right assume a crossing angle configuration for Run 4 ($+250\,\mu$rad horizontal).
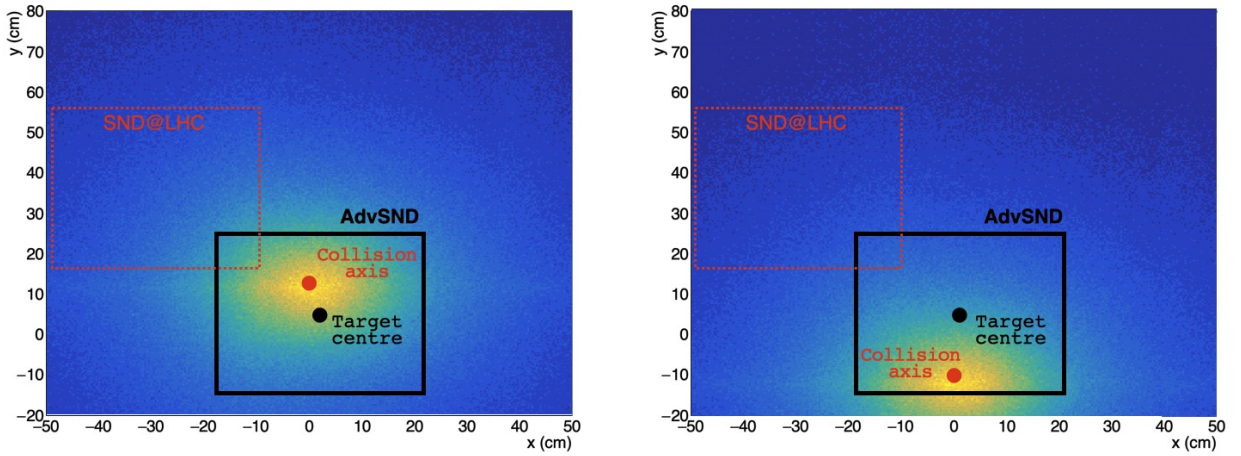
Figure 4: Simulated distributions of ν_μ interactions for vertical crossing angle configurations anticipated during HL-LHC: +250 μrad (left) and -250 μrad (right). The position chosen for AdvSND optimizes the coverage of all configurations.

origin of the interaction vertex and improve the momentum resolution. This setup will allow a measurement of the muon momentum with a precision of 20% for a 1 TeV muon and allow a better than 3σ determination of the muon charge over the whole range of expected momenta.

The proposed baseline detector is shown in Figure 5.
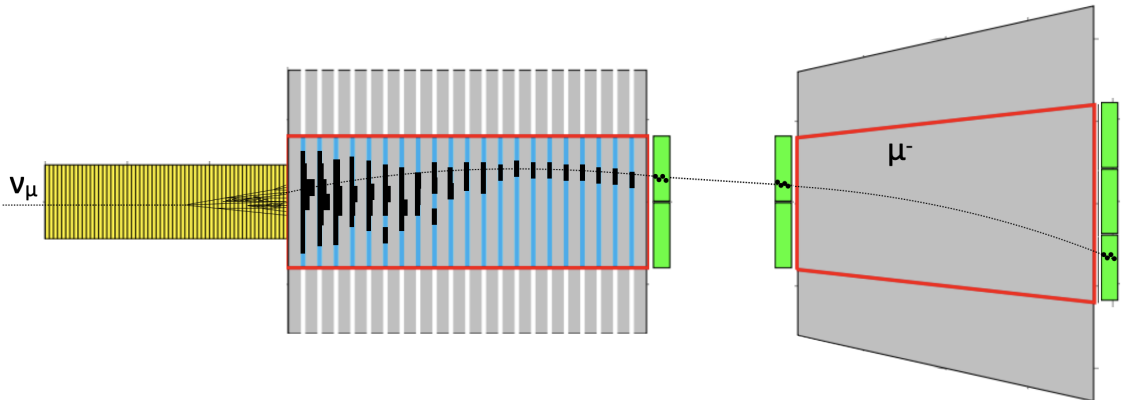

Figure 5: Sketch of the proposed baseline layout of the AdvSND detector with a simulated ν_μ interaction. The red lines show the outline of the coils that magnetize the Hadron Calorimeter and the Muon Spectrometer.

2 Detector design

The requirements for an optimal neutrino detector are imposed by the characteristics of the interactions of the various neutrino species:

- A highly efficient Veto detector in front of the Target to veto/tag charged particles entering the detector.

- A Target consisting of a vertex detector embedded in a high mass stack. The Target will act as an Electromagnetic Calorimeter (ECAL) with good timing resolution and will be part of the trigger of the experiment.

- The identification of electron neutrino charged current (CC) interactions requires a good ECAL with sufficient spatial resolution to separate electrons from π^0. A Hadronic Calorimater (HCAL) is needed to contain and sample the hadronic shower resulting from the CC ν interaction.

- The identification of muon neutrino CC interactions requires at least 10 λ_{int}s of material in front of a Muon Spectrometer to measure the muon momentum and identify the charge of the muon and a good HCAL to estimate the energy of the incoming neutrino. The simulated ν_μ interactions shown in Figure 6 illustrate the diverse topologies of hadronic showers associated to the interaction vertex.

- Tau neutrino CC interactions require a vertex detector that is able to separate the ν_τ vertex from the τ decay vertex.

- A magnetic spectrometer to separate neutrinos from anti-neutrinos (for the 18% of τ leptons which decay into μ).

The design of the upgraded detector closely resembles the current detector, comprising a neutrino Target serving as both a Vertex Detector and an Electromagnetic Calorimeter. The major enhancement (see Figure 1) consists of the addition of a magnet to measure the momentum of the muons produced by the neutrino interactions.

The detector fits in the same area (the TI18 tunnel). The modifications to the concrete structure of the tunnel can be separated into two steps. Firstly, to improve the acceptance of the detector, the base of the tunnel needs to be excavated. Secondly, to allow the installation of a magnet, the tunnel section needs to be enlarged. The study of the civil engineering implications of these modifications is currently ongoing. Depending on the outcome, two designs are possible: one (*AdvSND* or *baseline*) that fully exploits the research potential, including a magnetized Hadron Calorimeter and a magnetic Muon Spectrometer, or one (*AdvSNDReduced* or *minimal*) with a reduced potential in case the proposed tunnel enlargement cannot be implemented. Both options will share the same Target structure but differ in the conception of the hadron calorimeter and the muon measurement station.

2.1 Veto system

The upgraded Veto system uses the same technology as the current detector: stacked scintillating bars coupled to Silicon PhotonMultipliers (SiPMs). Currently, the Veto system (shown in Figure 7) comprises three layers: two horizontal and one vertical.
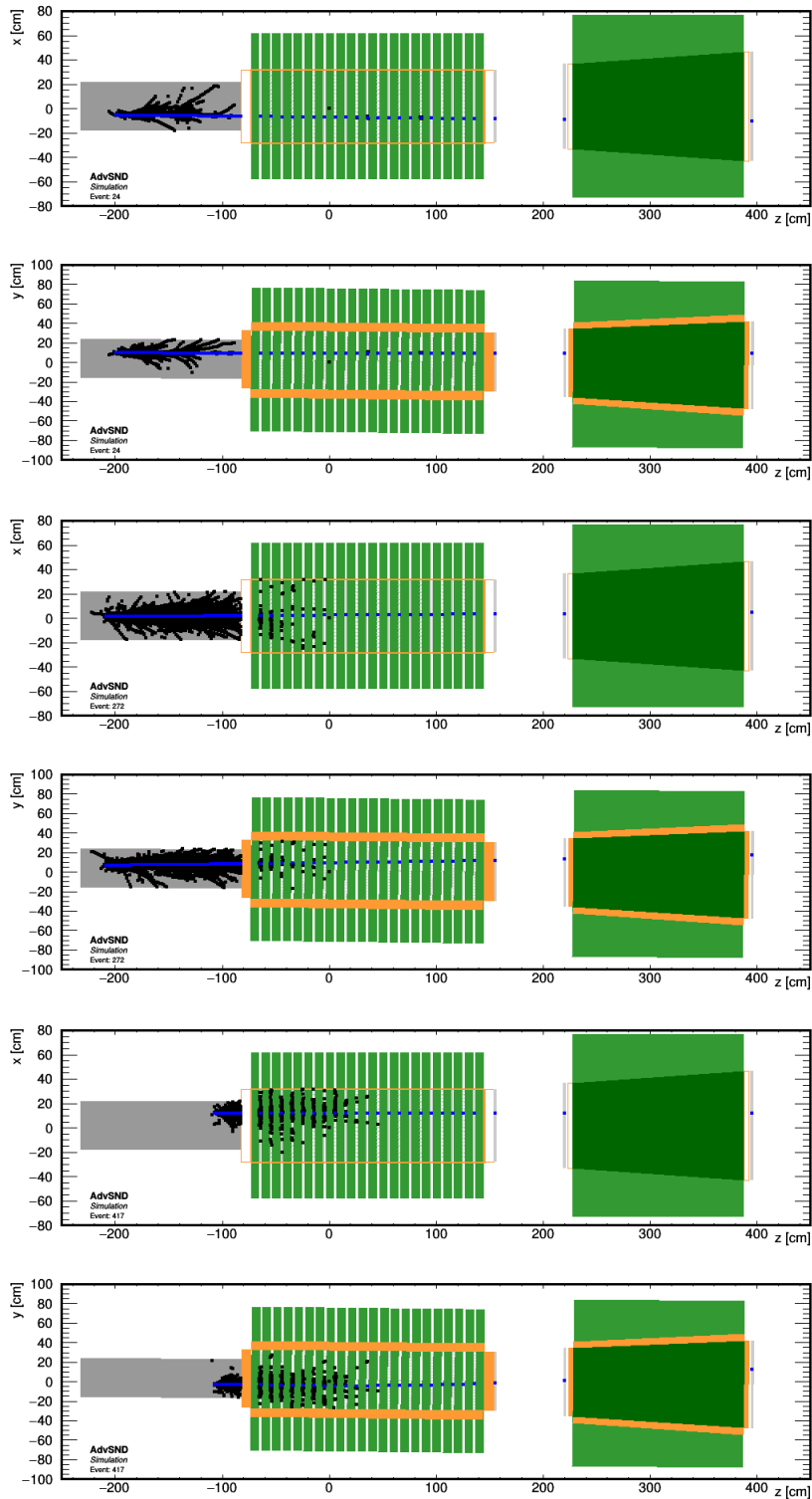
Figure 6: Three different simulated ν_μ interactions (top and side views for each event) highlighting the complexity of pattern recognition and tracking due to the fluctuations of the hadronic shower development. The design of the Hadron Calorimeter and Muon Spectrometer have been optimized to reduce the overall length of the detector.

The two horizontal bar modules are readout on both end of the bar while the vertical bar module is readout only at the top due to space constraints.
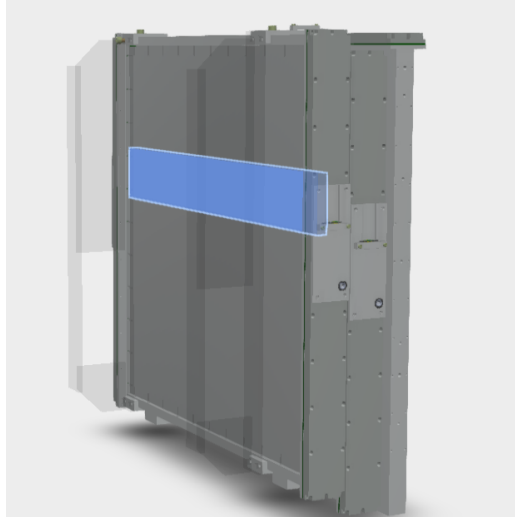

Figure 7: Veto system of SND@LHC highlighting one scintillating bar.

One significant factor affecting the Veto system is the electronics dead time, estimated at a minimum of 220 ns. Given a muon rate of 4 kHz, the anticipated inefficiency is approximately 8.8×10^{-4}. Reference [5] discusses examples of events where the Veto system failed to tag the background muons entering the acceptance of SND@LHC: one such event is shown in Figure 8. To mitigate such Veto failures we propose to reduce the width of the bars from 6 cm to 3 or 2 cm. Each bar is readout by several SiPMs (4 on each bar end) with each SiPM readout individually as to allow a multiplicity logic to reduce the effect of individual SiPM noise. Care shall be taken in stacking the planes of scintillators to cope with the inefficiencies of the single planes due to the dead space between the scintillator bars (see Figure 9).
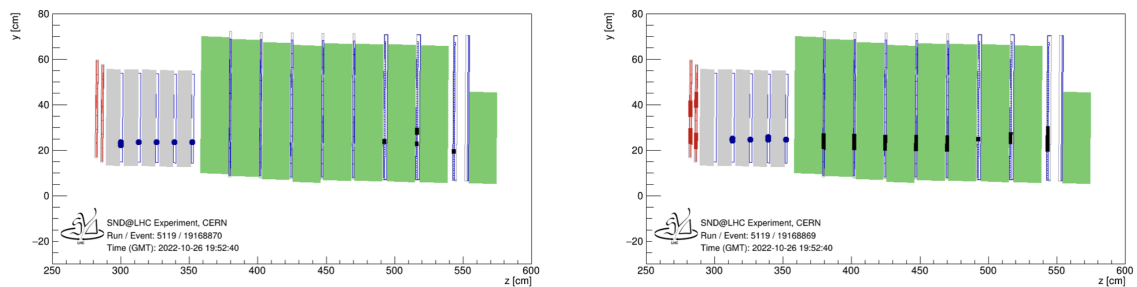
Figure 8: A muon candidate which the Veto system failed to detect (left). We assign the failure due to deadtime: the figure on the right shows another muon candidate entering the same area 4 clock cycles earlier (100 ns).

2.2   Vertex Detector and ECAL

As in the current detector, the passive element of the Target will be tungsten. The mass of the Target will be increased by as much as available space allows. We estimate that doubling
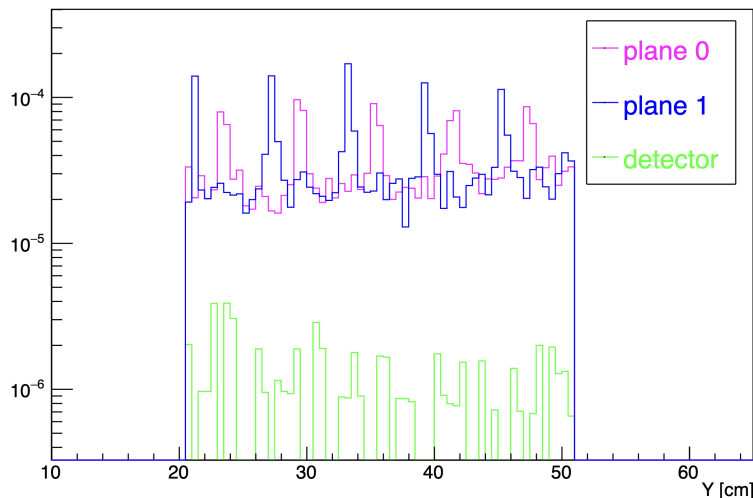
Figure 9: Inefficiency along the vertical axis of the present Veto system, showing the effect of the dead zone between bars. The green line, shows the combined inefficiency.

the total mass to reach approximately 2 tons is feasible. The active detector for the Target, the vertex detector, will consist of silicon detector planes interleaved with tungsten plates. The thickness of the tungsten plates will be around 5 mm, subject to optimization based on test beam exposure and extensive simulations. To trigger the readout of the silicon detectors, we will insert 4 planes of fast timing detectors in the Target stack (see Section 2.3 for the options being considered). We are considering two types of silicon detectors for use as vertex detectors in the Target: $x - y$ planes of silicon strips and planes of high-resolution silicon pixel detectors. The number and positioning of silicon pixel detectors are part of an ongoing optimization study.

We plan to use a tungsten alloy with a density $\sim$18 g/cm^3, facilitating the machining of tungsten plates and ensuring adequate thermal conductivity. For the silicon strip planes, we intend to re-purpose the silicon strip modules of the Outer Barrel tracker of CMS, which will be dismantled at the end of Run 3 of the LHC.

2.2.1   Baseline: Silicon Microstrips

The CMS Tracker   The CMS silicon strip tracking system is housed in a support cylinder approximately 5.5 m in length and 2.2 m in diameter. It consists of several subsystems as shown in Figure 10. The Tracker Outer Barrel (TOB) spans the central section, covering the radial region from 50 cm to 110 cm. Inside the TOB are housed the Tracker Inner Barrel (TIB) and Tracker Inner Disks (TID).

Within the TOB, silicon modules are organized into six concentric cylindrical layers. Of interest for Advanced SND@LHC are the modules populating the two outermost layers of the TOB.

In the TOB, modules are fixed with tiny screws to mechanical structures termed "rods" (Figure 11), which provide structural support and cooling. The absence of adhesives or thermal interface materials in the assembly of the modules onto the rods facilitates relatively straightforward disassembly, posing minimal risk of module damage.

Within a rod, electronic signals from each module are converted into optical signals by an Analogue Opto-Hybrid (AOH), which is plugged into the adjacent interconnection board. Con-
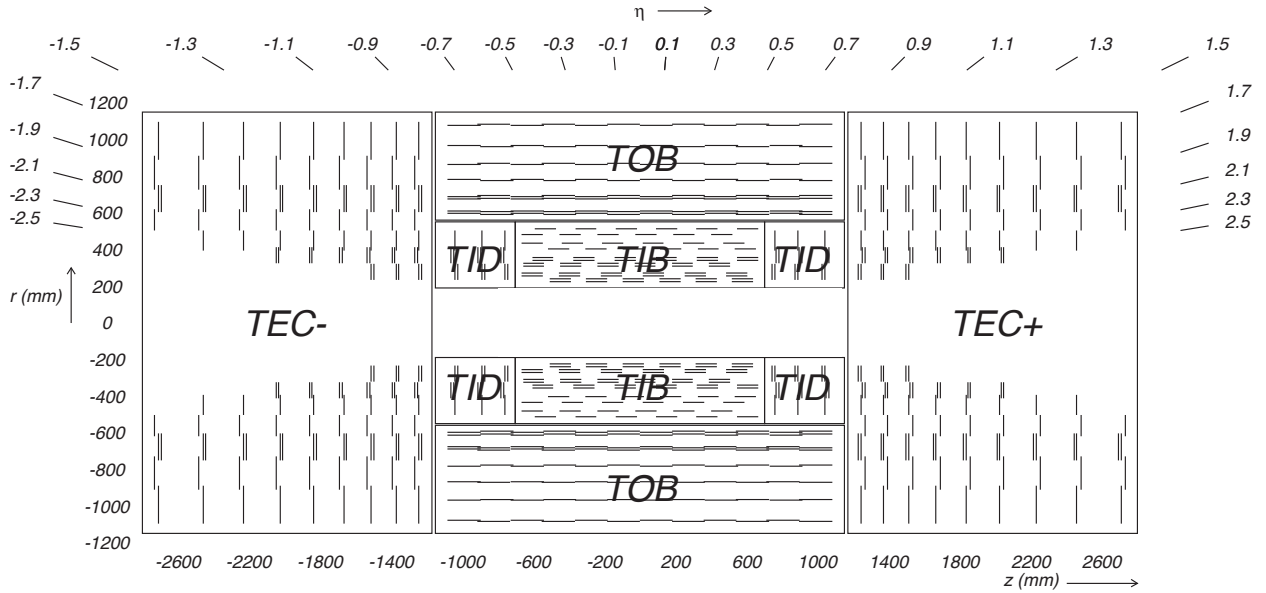
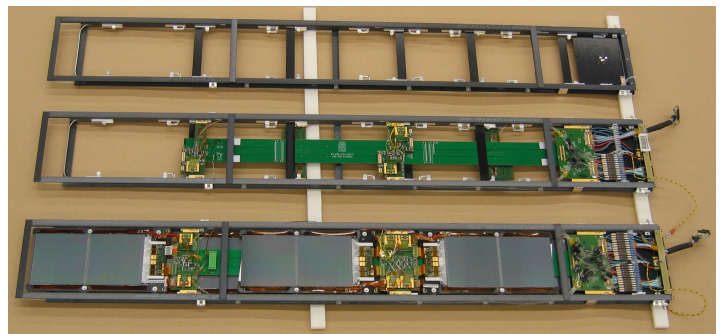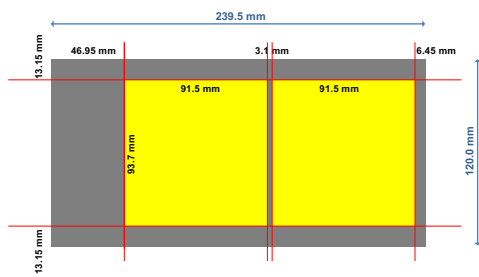Figure 10: Layout of the CMS Strip Tracker.

Figure 11: CMS Tracker modules. Left: The dimensions of two modules. The sensor's active area is represented in yellow. Right: A "rod", the mechanical structure housing the modules in the TOB. The image shows a standalone structure (top), with electronics boards (center), and fully equipped with silicon modules (bottom).

trol signals are distributed to the detector modules from the Communication and Control Unit Module (CCUM) situated at the end of the rod. CCUMs of adjacent rods are interconnected in a ring configuration, typically comprising 5 – 10 CCUMs per ring. This ring is completed by a Digital Opto-Hybrid Module (DOHM), which converts electrical control signals into optical signals and communicates with the back-end control electronics.
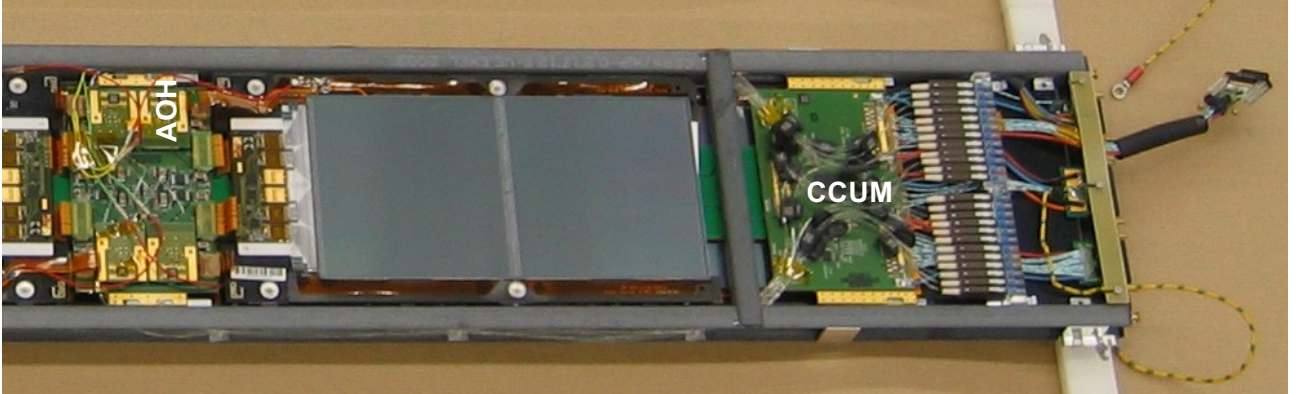

Figure 12: The electrical signals from each CMS module are converted into optical signals by an Analogue Opto-Hybrid (AOH). The Communication and Control Unit Module (CCUM) generates control signals for all the modules within a rod.

Each rod is powered by a power cable that connects to a Power Supply Unit at the backend. DOHMs are individually powered by dedicated power cables and power supplies.

In addition to the modules, it is proposed to repurpose AOHs, CCUMs, DOHMs, and all backend electronics for power, readout, and control. However, the integration of these components into the AdvSND detector geometry and experimental site requires new interconnection boards, power cables, and optical fiber cables.

The CMS TOB silicon tracker modules of interest for AdvSND and the corresponding electronic components will be provided to the Collaboration at no cost. The specifics of this arrangement are outlined in a Memorandum of Understanding, which was approved by the CMS Collaboration Board [6] on February 9th, 2024.

In CMS, silicon sensors are subjected to radiation damage from the hadrons originating in the proton-proton collisions. The fluence of hadrons per unit surface is roughly inversely proportional to the square of the distance from the beam axis. Therefore, the sensors in the two outermost layers will have consumed only a fraction of their radiation lifetime by the end of Run 3. However, the management and operation of silicon modules with irradiated sensors demand special attention.

To minimise reverse annealing, irradiated sensors must be consistently kept in a controlled, cold environment, even when not under bias. The time constant for reverse annealing damage increases exponentially with temperature. Below 0°C, the effect is essentially halted.

Figure 13 shows the expected evolution of the full depletion voltage for the sensors of layers 5 and 6 of the TOB, as a function of time spent at three different test temperatures after the Tracker's extraction from CMS. This forecast is based on the premise that an integrated luminosity of 3000 fb^{-1} will be collected by the end of Run 3. The sensors can be safely operated up to a voltage of 600 V. The results of the simulations show that a good control of the temperature is mandatory during the disassembly and assembly phase, to ensure that some

budget of time at room temperature is preserved for later maintenance interventions, during the exploitation of the detector.

When biased, the sensors dissipate power due to the dark current induced by the radiation damage, which also scales exponentially with temperature. In operational conditions, sensors shall be maintained below 0°C, which requires a thermal enclosure with an effective cooling system and a dry atmosphere to prevent condensation and ensure optimal functionality.
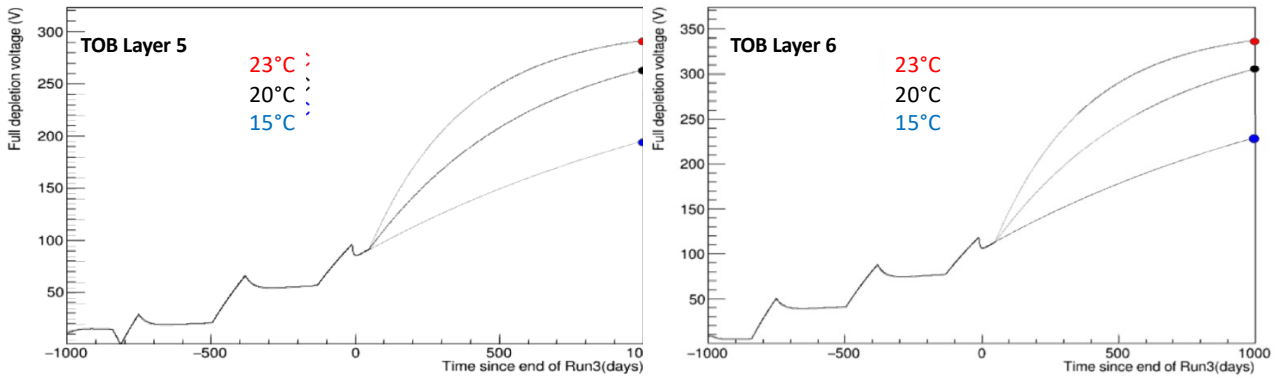
Figure 13: Expected evolution of the full depletion voltage for the sensors of layers 5 and 6 of the TOB, as a function of time spent at three different test temperatures after the Tracker's extraction from CMS.

The AdvSND Target design   The Target features a modular design, with the fundamental unit being a "station", that consists of a tungsten alloy plate supporting silicon modules (see Figure 11) on the front and back surface (Figure 14). The modules on the rear of one station, in conjunction with those on the front of the subsequent station, form an "active layer".
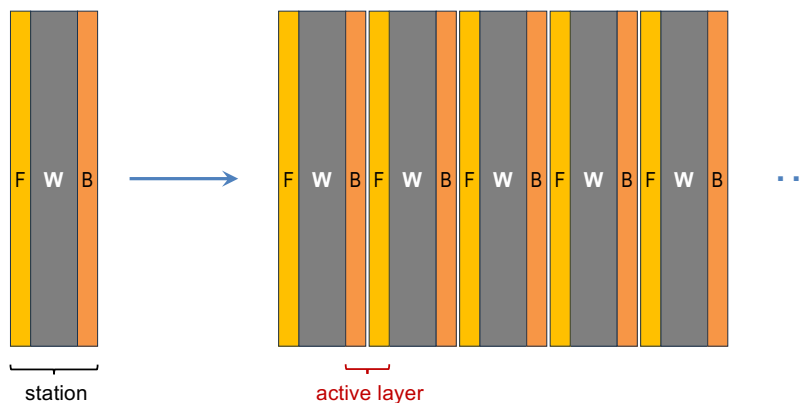
Figure 14: Schematic of a station, featuring a tungsten alloy plate that supports silicon modules both surfaces. Together, the modules from the back of one station and the front of the next form an "active layer."

Each station is equipped with four modules on each surface, with modules on opposite surfaces of a station oriented orthogonally to each other. All stations are identical, and each

consecutive station is rotated by 90 degrees to ensure hermetic active layers that alternately measure the x and y coordinates. The arrangement of modules within a station and the orientation of consecutive stations are shown in Figure 15.

Figure 15: Layout showing the positioning of modules within a station and the orientation of consecutive stations to create hermetic active layers for x and y measurements. The tungsten plate and supporting mechanics are omitted for clarity.

The modules are directly mounted onto the tungsten plate using four screws and washers, similar to the assembly in the CMS Tracker. The plate itself is secured by a steel fram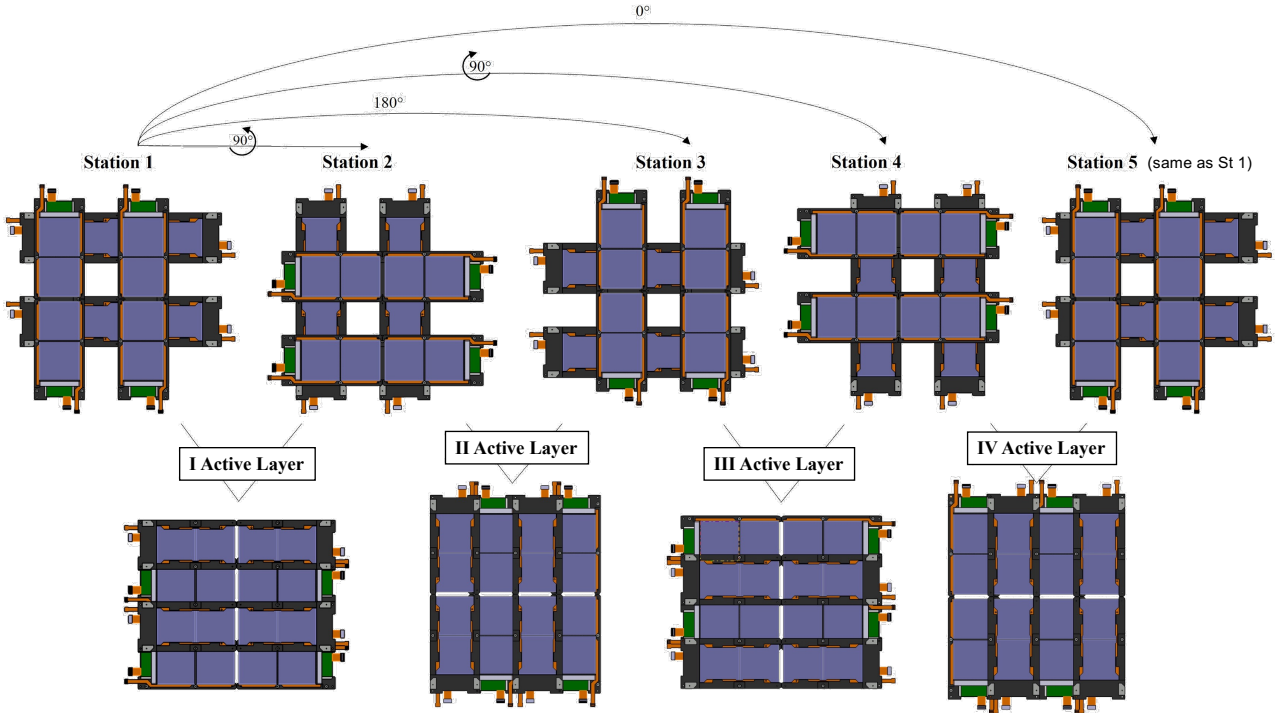e, which also provides support for four ReadOut Boards (ROBs), housing the AOHs, and four optical connectors that aggregate fibers from the AOHs (Figure 16). A single Station Control Card (SCC), equipped with the CCUM, is electrically connected to the nearest ROB with a flat cable. Each ROB is in turn connected to the next one, with a similar flat cable, along the periphery of the steel frame. The SCC, powered by a single cable from the backend, distributes current to the modules via the ROBs and is mounted on one side of the steel frame with a bracket. The CCUMs from eight consecutive stations are interconnected, completing the ring architecture with a DOHM. Each DOHM connects to the backend through a dedicated power cable and an eight-fiber bundle.

A tungsten alloy suitable for machining flat surfaces and threaded holes at an affordable cost will be selected, with a density of approximately 18 g/cm^3. The dimensions of the tungsten plate are 45×45 cm^2, while the outer dimensions of the steel frame are 60×60 cm^2.

The structure supporting the stations will take the form of a horizontal rack allowing individual stations to be inserted and removed easily. This design facilitates maintenance by enabling interventions on any station irrespective of its position within the detector. The thickness of the tungsten plate is assumed to be 7 mm for detector modeling and cost estimation, and will be optimized through simulations. The detector mechanics can be readily adapted to the final
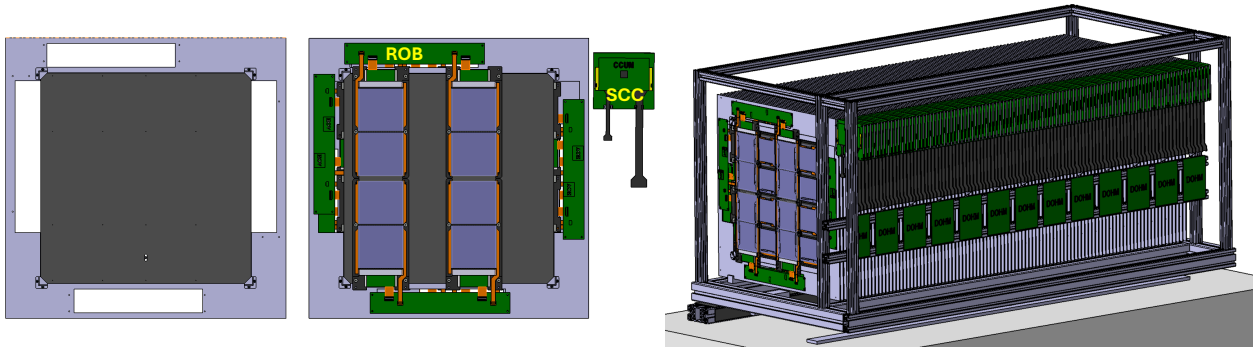
Figure 16: From left to right: The tungsten plate within its supporting steel frame; a station equipped with modules and ROBs; the full stack of 100 stations. The SCC is placed externally on the top-right corner, independently of the station's orientation.

choice of thickness by adjusting only the angular supports for the plate and the pitch of the supporting rack.

The Target will be encased in an insulated enclosure, ventilated with dry, filtered air and cooled to approximately $-20°$C to ensure optimal conditions for the operation of irradiated sensors. The choice of the most effective cooling technology is currently under study, and will be validated through detailed thermal simulations. The dry air system, critical for the detector's safe operation, will be connected to an uninterruptible power supply and supported by a backup battery of bottles.

With 7 mm thick tungsten plates and considering the silicon modules 3.5 mm height, the distance between consecutive stations is set at 1.5 cm, including a 1 mm clearance. The complete Target comprises 100 stations, leading to a total length of 170 cm, which includes 20 cm for the thermal enclosure, and results in a total tungsten mass of 2.55 tons, with 1.75 tons covered by the active silicon sensor area. A total of 800 silicon modules will be used, compared to the 1680 modules available from dismantling TOB layers 5 and 6.

Should a different tungsten thickness be selected, the overall Target length will remain unchanged. For instance, with a tungsten thickness of 3.5 mm the Target would be instrumented with 130 stations, utilizing 1040 silicon modules, and the total tungsten mass would be 1.66 tons, with 1.13 tons beneath the active sensor area. Simulations will determine the optimal balance between sampling frequency and Target mass.

Most of the cross-sectional area of the services is occupied by the 100 power cables (one cable per station). Additionally, the setup includes 25 fiber optic cables for the data readout, 13 power cables and 13 fiber bundles serving the Digital Opto-Hybrid Modules (DOHMs). At the backend, power supply units are accommodated within two racks, while readout and control boards are housed in a single rack. The racks require water-assisted air cooling.

A Programmable Logic Controller (PLC)-based Detector Safety System, installed in a separate rack, oversees the operation of the dry air system along with its emergency backup and generates an interlock for the power supplies in response to cooling system failures.

Detector construction   The CMS Tracker will be delivered to the SND@LHC team, supported by a cradle on wheels. The initial phase involves extracting the two Tracker EndCaps (TECs) and the Barrel section —comprising the Tracker Outer Barrel (TOB) and the Tracker

Inner Barrel plus Tracker Inner Disks (TIB+TIDs) — from the Tracker Support Tube. This operation requires three smaller cradles on wheels to receive the three subsystems. Once the subsystems are removed, the Tracker Support Tube will be relocated. One TEC is expected to be reclaimed by the CMS Tracker Collaboration for outreach activities. To enable these operations and ensure the mobility of the subsystems alongside the Tracker Support Tube, a workspace of approximately 8×14 m^2 is deemed adequate, equipped with a large access door and a minimum ceiling height of 3.5 m. Subsequently, the extraction of rods from both ends of the Barrel can commence. The disassembly of modules from rods and the assembly of AdvSND stations should proceed in parallel with rod extraction. This is to avoid the need for additional storage and handling infrastructure for rods and modules. The spatial requirements for Tracker disassembly match well with the needs for rod disassembly and station assembly after the removal of the Tracker Support Tube, as shown in Figure 17.
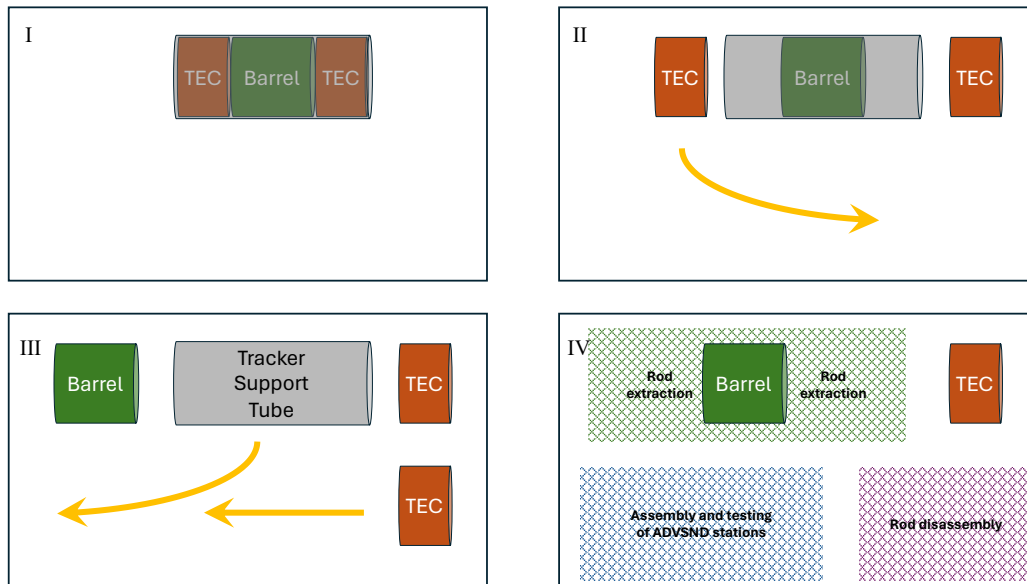
Figure 17: The sequential tracker disassembly, rod disassembly, and station assembly phases.

The assembly area requires filtered ventilation alongside a robust air conditioning system with humidity control. To mitigate further damage to the irradiated sensors, it is desirable to maintain the room temperature at around 18°C during operational hours, lowering it to approximately 14°C during non-working hours. Figure 18 provides a simplified view of the detector construction schedule.

Table 1 lists the detector components and tools necessary for constructing the Target, accompanied by a cost estimate. Not included in the estimate is the cost of the assembly room. Should a suitable facility not be available at CERN, investments may be required to create an appropriate construction space.

It is noteworthy that the tungsten plates represent the primary cost driver, with their expense largely correlating with the mass of tungsten used. Consequently, should the optimal design require a Target with increased sampling and reduced mass, the overall cost would be smaller. The estimated cost of the tungsten is derived from a quote from a manufacturer specialized in mechanical components made of tungsten alloys, covering precision machining,

Figure 18: Simplified timeline for the construction of the AdvSND detector.

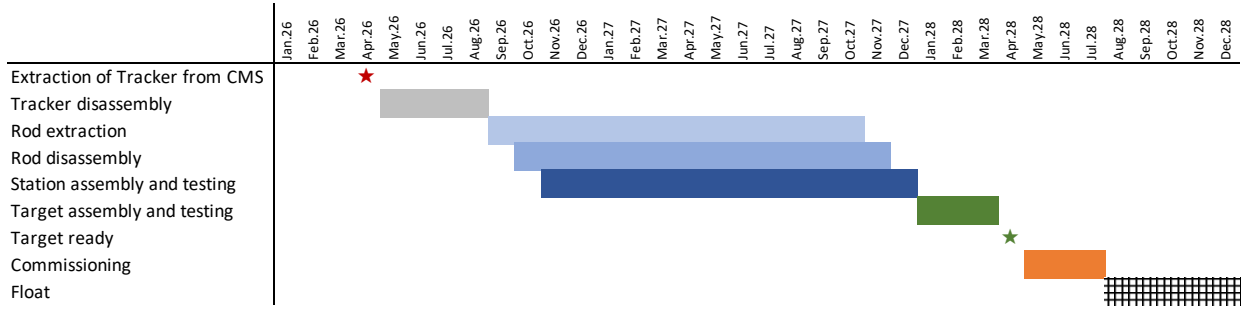| Detector elements and services	In detector	Extra	Total	Unit cost CHF	Total cost kCHF
Tungsten plates	100	10	110	3000	330.0
Steel frames	100	10	110	100	11.0
ROBs	400	40	440	90	39.6
SCCs	100	10	110	50	5.5
Flat cables	400	40	440	25	11.0
Power cables	100	15	115	150	17.3
Control power cables	13	5	18	150	2.7
Optical fiber connectors*	2504	255	2759	19	52.4
Optical fibres**	25040	2505	110	0.25	6.9
Mechanical structure			1	15000	15.0
Thermal enclosure			1	6000	6.0

*The cost of optical connectors is given per channel.

**The cost of optical fibers is given per channel per meter.

Detector backend systems	Number	Unit cost CHF	Total cost kCHF
Dry air system	1	10000	10.0
Dry air bottles	1	4000	4.0
Cooling system	1	25000	25.0
Detector Safety System	1	10000	10.0
Racks	4	1800	7.2

Tools	Number	Unit cost CHF	Total cost kCHF
Barrel cradle	1	10000	10.0
Rod extraction	2	3000	6.0
Rod handling	2	600	1.2
Rod disassembly	1	7000	7.0
Module handling	3	800	2.4

Total estimated cost: 580 kCHF

Table 1: Cost estimate for constructing the Target using CMS Tracker silicon modules.

surface finishing, and the creation of the threaded holes for module mounting. A comprehensive market survey could potentially yield more competitive pricing, hence the tungsten plate cost can be considered as an upper limit, based on today's tungsten market price. In the perspective of construction, it still carries a non-negligible uncertainty due to the volatility of the market price of tungsten. The cost estimates for the other project components are derived from catalog prices, where available, or from previous experience with similar productions. The largest source of uncertainty in the project's total cost arises from potential fluctuations in the market price of tungsten, which is an unavoidable risk.

Development roadmap Ahead of the CMS Tracker decommissioning, the development of the Target stands to benefit significantly from 42 functional modules left over from the Tracker's construction, which have been made available by the CMS Tracker Collaboration. Notably, these modules have not been irradiated, allowing for their operation at room temperature.

The initial phase involves constructing a full-size station demonstrator, opting for a cost-effective and easily machinable material like aluminium in place of tungsten. This station will be fully populated with modules and electronic boards, connected to the power and readout systems, and operated in the lab. The construction and subsequent operation of this station demonstrator aim to validate the design and geometry, confirm the functionality of the electronic boards, and commission the entire readout chain. Additionally, it will be valuable tool

for the Collaboration to gain familiarity with the CMS Tracker electronics and readout system.

Following the successful demonstration of the station design and functionality, the available modules can be utilized to construct a "mini-detector" consisting of 21 layers of stations, with modules installed in only one of the four quadrants (yielding active layers of approximately $20 \times 20 \, \text{cm}^2$). The potential use of spare tungsten plates, owned by the Collaboration, as passive material is currently under evaluation. This device is suitable for operation with electron or pion test beams, aiming to assess the detector response to physics signals, validate the simulation and facilitate the optimization of reconstruction algorithms.

2.2.2 Vertexing performance

The main task of the Target is identifying the primary ν interaction vertex and potential secondary vertices to allow differentiation of different signal processes. The environment for the vertexing is challenging, as the large material budget of the tungsten between tracking planes introduces showering between measurements. As a result, many hits are registered around the vertex, and isolated hits are rare in the stations closest to the primary vertex. Instead of attempting to reconstruct all tracks in this environment, which would require a detector with lower occupancy per channel such as the pixel detector presented in Section 2.2.4, the vertexing strategy focuses on reconstructing a few, good tracks per event, seeded using isolated hits further downstream, in order to determine the location of the primary and potential secondary vertices. All results presented here are for the baseline option of CMS TOB strips.

To study the tracking and vertexing performance, a sample of 1 000 000 muon neutrino CC events in the tracker acceptance are generated using the SND@LHC simulation framework, and digitised. The tracking and vertexing performance is then studied with and without a leading-hit clustering to understand best and worst case tracking performance. Once track candidates are identified, they are fit using a Kalman fitter from the GenFit track fitting framework[7].

The resulting residuals for the x projection are shown in Figure 19. The track residual and resulting resolution is compatible with the expectation of $122 \, \mu\text{m}/\sqrt{12} \approx 35 \, \mu\text{m}$.

These first results indicate the capability of the tracker to reconstruct muons and the vertex in muon neutrino CC events. Reconstruction of displaced vertices due to tau or charm decays is under study, and will likely require further optimisation in the vertexing resolution and efficiency.

2.2.3 ECAL performance

In addition to its role as Vertex Detector, the Target needs to function as an Electromagnetic Calorimeter, i.e. it needs to be able to reconstruct electromagnetic showers, estimate their energy and distinguish between different types of showers.

With a more detailed study of the ECAL performance underway, a proof-of-concept study has been completed to demonstrate its capability to differentiate between showers originating in π^0 and e, to differentiate between ν_e CC scattering and other processes. All results presented here are for the baseline option of CMS TOB strips.

Using simulated samples of ν_e CC and ν_μ neutral current (NC) (100 000 each) interactions occurring in the AdvSND target, hits belonging to showers in both samples are identified, and several simple features are constructed. A minimal selection is applied to cut showers with fewer than 6 hits in each view and in fewer than 4 stations, to remove showers outside of the detector acceptance. The samples are combined in a ratio of 2 between π^0 and electron
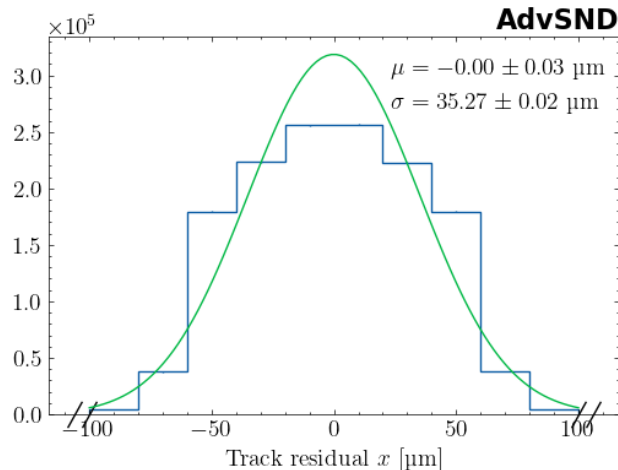
Figure 19: Track residuals in the x projection showing the best fit values for the resolution.

showers, to match the expected abundance in data, discarding the excess of electron events. The identification of showers was outside of the scope of this study. The features include the total number of strips activated, as shown in Figure 20 (Right), the asymmetry in the number of strips activated in each view as proxy for the transverse shower shape, the number of stations registering the shower as a proxy for the longitudinal shape, the total, average and maximum density of hits per station, and the total energy loss registered by the tracker.

Many other features are imaginable, and the list will be optimised in the future, also in regard as to potential biases introduced by this selection. Independently, a regression algorithm may be trained to estimate the shower energy. For simplicity, we use the constructed features to train a boosted decision tree (BDT), to find the optimal hyperparameters for the problem.

After training on the full dataset, the BDT values shown in Figure 20 (Left) are obtained on the test sample. On the same test sample, an area under the curve (AUC) of the Receiver Operating characteristic (ROC) of 0.99 is achieved.

The training was performed with approximately equal numbers of signal and background showers. The optimal cut on the BDT will depend on the expected signal and background abundance in data. The BDT output may be used as an input into a higher level selection at the event level. These results demonstrate the feasibility of identifying electron and pion induced showers using only the silicon strip detectors.

2.2.4 Option: Pixel planes

In order to improve the tracking and vertex reconstruction we consider the possibility to insert pixel planes in the Target structure: the number of planes will depend on the resources that he Collaboration will secure (ideally with enough resources one would like to have, if not all, half of the planes, i.e. ~50, in the Target be pixel ones). For the Pixel planes, we plan to adopt the CMOS MAPS detector being developed for the ALICE collaboration ITS3 tracking upgrade. The ITS3 pixel modules are designed following their successful experience for the present ITS2 tracker based on the ALPIDE CMOS Monolithic Active Pixel Sensors (MAPS). The major innovation is the adoption of stitching: stitching is an industrial procedure to connect reticle sized (30 mm × 30 mm) ASICs with each other to propagate power and signals and thus create wafer scale sized sensors. In the most extreme case, this allows the suppression of the High
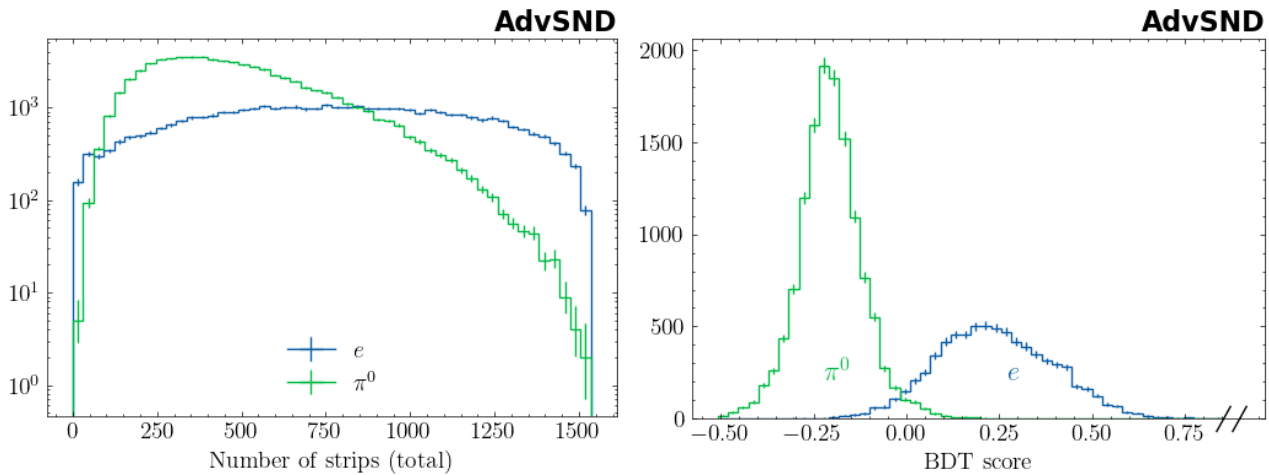
Figure 20: Left: Comparison of the total number of strips registering the shower. Right: BDT score distribution from optimised AdaBoost classifier trained on equal numbers of π^0 and e showers.

Density Interconnect circuitry which is standard in the traditional silicon pixel detectors in the sensitive area. The implementation technology is the 65 nm TowerJazz providing 300 mm wafers which allows the fabrication of sensors of 260 mm length. The silicon wafer floor-plan of the sensors is shown in Figure 21.
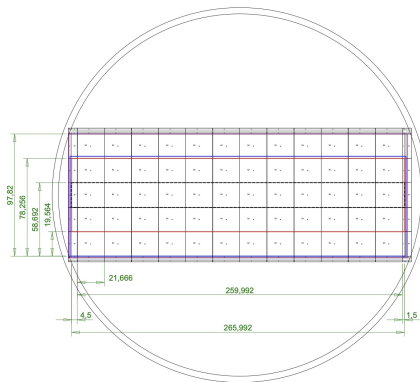
Figure 21: The floor plan of the silicon wafer with the ITS3 module: shown are the dimensions in mm, the black dotted rectangle shows one of the five segments and the colored contours possible groupings: in our case we would group all the segments together to be readout as a single module.

The transverse cross-section of the Target (40x40 cm) can be covered by a sensor plane composed of 8 modules allowing also an overlap of 12 cm in the middle of the plane (allowing reconstruction of tracklets in this region). On each module the pixel segments can be grouped together for the readout. The output line is compatible with the e-link input of the LPGBT developed by the CERN microelectronics group. Each module will be coupled to a relatively straightforward printed circuit board which will stick out of the side of the detector and which will provide configuration, power and readout of the module through wire bonds to the module. The low expected occupancy rate will allow grouping all the segments on one module such that

it will require, following the specs of the ALICE ITS3 module, 4 fibers to readout each module (hence 32 fibers per plane). The power needed (2 analogue, 2 digital and one bias) could also be fanned out to the whole detector from a single distribution crate. The low power consumption of the modules and the low radiation environment will allow operation at room temperature: the relatively low heat dissipated on the modules will be evacuated through the tungsten absorber planes which will be air cooled.

The environmental and research constraints of SND@LHC differ significantly from the ones of ALICE, which allow simpler -and cheaper- solutions. In particular AdvSND does not care about the material budget of the sensors: in fact we can keep the nominal wafer thickness of 750 microns which allows a more robust handling. Moreover the sensor planes are accessible on 3 sides with ample space hence allowing structures for servicing the detector which can sit at the edge of the detector hence simplifying the chain service connections (fiber, power).

For the backend readout we plan to re-use the microTCA modules being used by the CMS Collaboration and which will be replaced by the upgraded ATCA modules foreseen for the CMS Phase II upgrades. The interface to the LPGBT driven fiber will require a simple adapter to adapt LPGBT to the optical input of the CMS modules. Services (power. fiber bundles, racks, cooling) are assumed to be similar to the one needed by the silicon strips setup.

The cost for each plane of pixel is estimated to be:

- CMOS MAPS Stitched Pixels: 8 modules, i.e. 16 wafers assuming 50% yield, is estimated to cost 60k Chf

- PCB housing LPGBT for the readout/configuration and power regulation for each module: 8x250 CHF for a total of 2k CHF

- Power supply : 5k CHF

- The total estimated cost for a pixel plane comes to less than 70k CHF

2.3 Timing detector

Fast timing related to the neutrino interactions will be essential for triggering the logging of the various detector data. In particular we aim to have timing resolutions which could allow sharing the trigger with ATLAS in case this would be considered useful for specific studies. The latency foreseen by ATLAS for their first level trigger ($10~\mu s$) is sufficient to accomplish this task. A timing resolution of $\sim 50ps$ should match the resolution of the foreseen ATLAS forward time-of-flight detector. At this moment two different techniques are being considered by the Collaboration subject to ongoing R&D. The final choice will be made depending on the expected performance and ease of integration in the experiment.To this extent we plan to have dedicated prototype to be tested with particle beams at CERN.

2.3.1 Fast Plastic scintillator detectors

Hexagonal Scintillator modules   Silicon Photon Multipliers (SiPMs) hold significant promise for achieving excellent time resolution, especially when coupled with fast plastic scintillators. This approach enables a concentrated effort on minimizing photon travel jitter, crucial for precise timing measurements.

The achievable timing resolution with slowly decaying (on the order of nanoseconds) scintillators is primarily limited by the statistical nature of photon production converted into electrons within the detector [8, 9]. Poisson statistics govern the most probable time interval (t_Q) for detecting a threshold number (Q_{th}) of converted photons. This interval is influenced by the probability density of detecting individual photo-electrons (R) and their emission rate, which collectively determine their timing uncertainty. Therefore, the intrinsic time resolution hinges on two key parameters: the scintillator decay time (τ) and the total photon yield.

$$t_Q = \tau_f \times \ln\left[\frac{1}{2}\left(Q - R + \sqrt{(Q-R)^2 + 4R}\right)\right]$$

The optimal t_Q is attained when both τ and Q are minimized, and R is maximized. Among these factors, only τ and R depend on the scintillator material. Hence, selecting EJ-204 emerges as a favorable choice. Table 2 presents a comparison of properties between leading organic and inorganic scintillator materials.

To achieve the anticipated time resolution and reduce channel dead time, increasing the granularity of the scintillating material becomes imperative. We propose the utilization of hexagonal pads, specifically with dimensions of 30 mm per side and 20 mm thickness, to enhance granularity (see Figure 22). The hexagonal shape has demonstrated efficient internal reflection properties while ensuring uniform light distribution across the cross section [10].

Property	EJ-204	EJ-200	LYSO	BGO
τ_{decay} [ns]	1.8	2.1	36	16
Light Yield [kγ/MeV e-]	10.4	10.0	33	9

Table 2: Scintillators properties
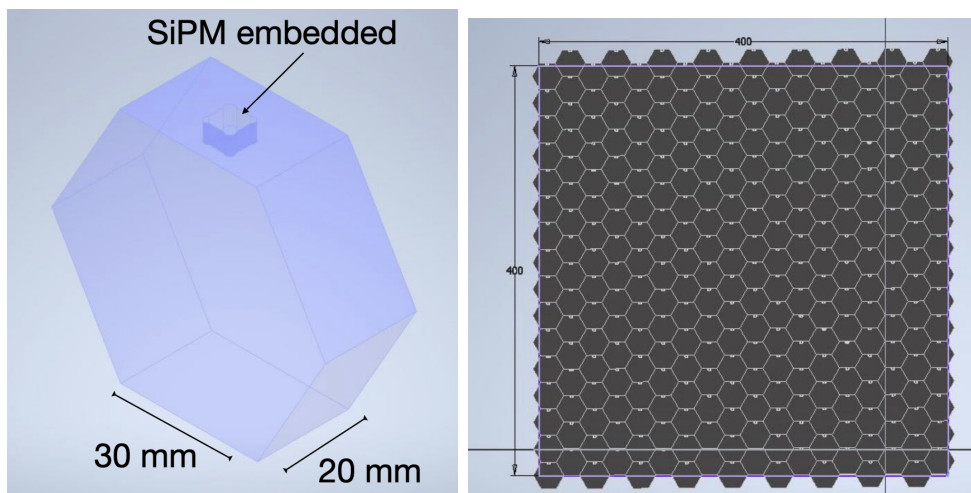
Figure 22: Hexagonal scintillator with SiPM embedded on top (left picture). A full single layer of a timing detector with a total of 288 single modules.

For this reason the proposal includes hexagonal modules as shown in Figure 22 (left) where the light readout will be done with a SiPM. The thickness of the hexagonal tiles/pads can be from 10 to 20 mm. A full layer of a timing detector can be built from 288 single modules to cover the Target area of 40 x 40 cm^2 as shown in Figure 22 (right).

Figure 23 illustrates the expected time resolution for various thicknesses from 10 mm to 20 mm, projecting a detector time resolution (σ_{det}) of approximately 40 ps. To enhance photon collection efficiency, SiPMs can be attached using optical glue with a similar refractive index (1.58), while the scintillator surfaces can be coated with EJ-510.
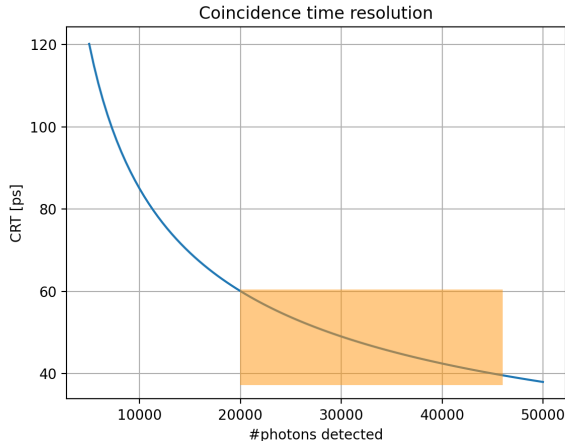
Figure 23: Estimated coincidence time resolution for a EJ-204 organic scintillator.

Moreover, addressing electronic time resolutions is crucial. We will adopt a dedicated Application-Specific Integrated Circuit (ASIC), TOFHIR2, recently developed for CMS[11], boasting a remarkable 15-20 ps time resolution. This ASIC is tailored to work seamlessly with SiPMs, featuring advanced functionalities such as dark count rate cancellation and leading-edge discriminators to mitigate time walk.

	Cost/Unit	Total Units	Total [kCHF]
SiPM	3.6	1260	45
Scintillator material	0.490	2	0.9
Machined material			5
Mechanical frame	1.0	4	4
Front-end	2.0	8	16
Total			71

Table 3: Breakdown cost of hexagonal scintillators.

The readout and power distribution for each SiPM can be managed via twisted pair cables behind each timing layer. These cables can be routed to a front-end PCB, housing four TOFHIR2 chips (32 channels) on each side of the layer.

Considering these factors, we anticipate constructing a timing detector layer with a granularity of $r = \sqrt{3}/2 \times 30$ mm. To eliminate dead zones between hexagonal shapes, each layer can be shifted by half or quarter hexagons, ensuring comprehensive coverage.

In summary, this comprehensive approach combining SiPMs and hexagonal scintillator modules offers a promising avenue for achieving exceptional time resolution in detector systems.

Plastic Scintillators Bars   Planes of stacked scintillating bars read out by silicon photomultipliers (SiPM) are able to cover a large area while maintaining fast timing. Such technology

has already been utilized in various experiments, including the timing detector of SHiP [12], the ToF detector for the ND280/T2K upgrade [13], and the Veto and Muon systems of SND@LHC [2]. Depending on the scintillator length, number of SiPM channels, and readout electronics, such detectors are able to achieve a timing resolution of 100 ps or better [14].

The Veto and Muon/HCAL systems of SND@LHC are composed of stacked scintillating bars read out on both ends by SiPMs. Both were originally conceived from the prototype of the SHiP timing detector, seen in Figure 24. The prototype comprised 22 vertically staggered EJ 200 scintillating bars of dimensions 168 cm × 6 cm × 1 cm and read out on both ends by an array of 8 SiPMs. The SiPMs were placed on custom built PCBs attached to an eMUSIC readout board and signal digitization was performed with SAMPIC. A timing resolution of 85 ps was measured for a single bar and 90 ps between adjacent bars. We are studying ways to improve on the timing resolutions.
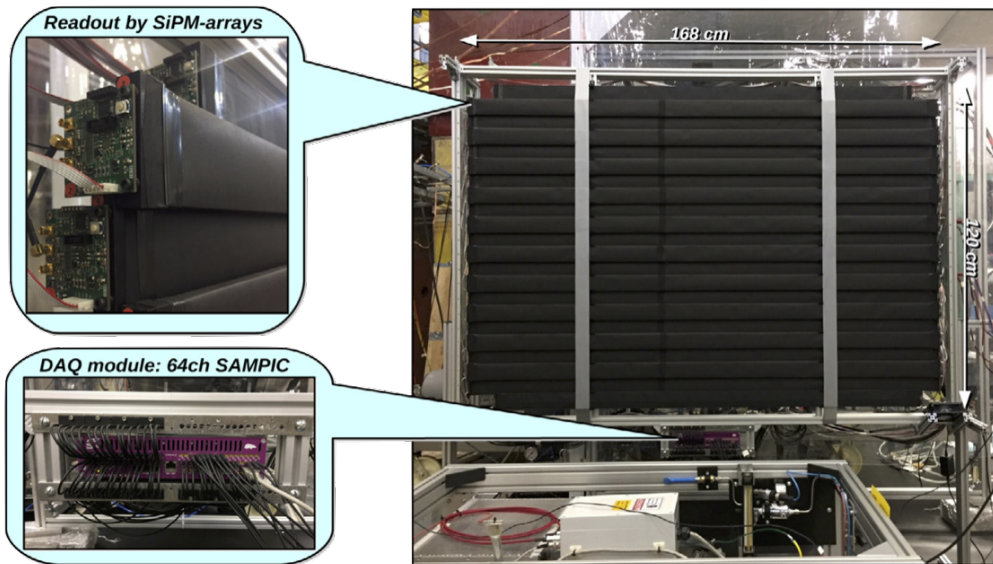

Figure 24: The prototype developed for the SHiP timing detector which could be easily adapted to the AdvSND geometry.

2.3.2   Fast Gas detector: Timing Resistive Plate Chamber

Timing Resistive Plate Chambers (tRPCs) are detectors known for their excellent time resolution that can be better than 50 ps. This is possible both in small pad-like detectors [15] and in large-area detectors such as the timing detector prototype for the SHiP experiment [16].

Due to the large number of particles produced in the Target, the only valid configuration for reading out the RPCs will be through relatively small pads, as the strip readout does not work in environments with a high particle density. To correctly extract the signal from the pads and thus preserve the time resolution, the only way is laterally as shown in [15] or as implemented in the ALICE TOF [17].

With these considerations in mind, we propose the construction of the timing detector based on RPC modules of approximately 8 x 40 cm^2 active area, see Figure 25a, equipped with at least four gas gaps of 0.3 mm but which could go up to twelve gaps as in the case of the SHiP timing prototype. Each module would be readout by pads of about 4 x 4 cm^2, with a total of
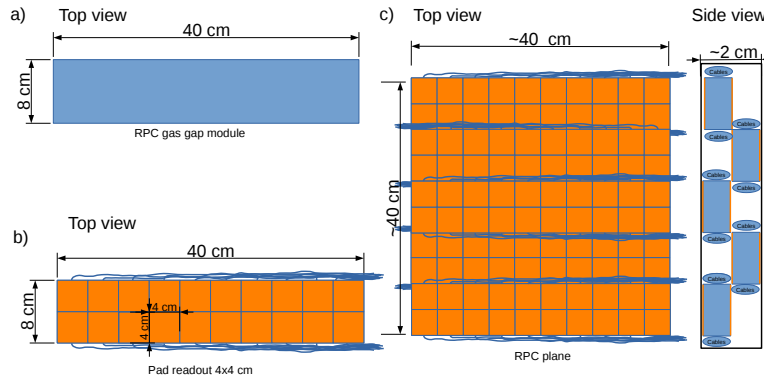
Figure 25: a) Top view of a RPC gas gap module. b) RPC module equipped with twenty 4 x 4 cm^2 pads readout from the side. c) RPC plane built from five RPC modules with a total area of 40 x 40 cm^2 and readout by hundred pads.

twenty pads, the signal being extracted with a coaxial cable or an impedance-controlled PCB, from each of them laterally, see Figure 25b. Each of the planes will consist of five modules with a certain overlap, see Figure 25c, with a total area of 40 x 40 cm^2. The side view of the plane shows the five modules with overlap in two layers leaving space for cable routing. The total thickness of the detector will be about 2 cm. In total each of the time planes comprise hundred readout channels.

Signal readout could be performed with well-tested and well-established fast electronics as described in Reference [18] and a multi-hit TDC. The total system will consist of four identical detection planes. With this configuration, we expect a time resolution below 50 ps, compared to a previous result of the group in a similar setup [15] and an efficiency close to 100 %.

The degree of maturity of the sealed RPC technology [19] does not allow us to decide, at this stage, whether the gas gap will be sealed or standard, operated with an eco gas [20]. This will be a fundamental aspect of the RD performed.

Table 4 shows an estimate of the cost of each of RPC plane with a value of about 13 kCHF/plane, including: FEE, RPC modules, mechanics and cabling. This value is dominated by the FEE which has been calculated with a budget corresponding to few channels, so we expect this value to be reduced considerably. The value of the overall system is about 70 kCHF, including: four RPC planes, data acquisition system based on the TRB board [21] and low and high voltage system.

Item	Nb Units	Unit price	Plane price	Total [kCHF]
nb planes	4			
FEE(MB+DB)	4	2	8	32
RPC plane	1	3	3	12
Cabling	1	0.5	0.5	2
Mechanics	1	1.5	1.5	6
Total detector		7	13	52
LV	2	1	2	2
HV	2	3	6	6
TDCs plane	4	3	12	12
Total		14	33	72

Table 4: Breakdown cost of the timing detector based on RPC technology.

2.4 HCAL

2.4.1 Neutrino Interactions and Hadron Showers

For all neutrino flavors, energetic νN collisions produce hadronic showers, which develop across the Target and the HCAL, the share depending on the interaction depth in the Target.

Neutrinos impinging on SND@LHC can have energies up to a few TeV, and cause hadronic showers bringing on average half of the neutrino energy. A total absorber thickness of 10 λ_{int} is required to contain an energy fraction larger than 95%. Since neutrinos can also interact late in the Target, the HCAL itself has to be large enough for shower containment.

Active layers in both the Target and the HCAL contribute to measure shower properties, as illustrated in Figure 5. The sampling frequency in SND@LHC is tuned for an energy resolution of about 20% in the range 100 to 300 GeV (Figure 27). Ideally, for detector response uniformity, the Target and HCAL regions should have comparable resolutions, and, for the quality of their relative calibration, no absorber should be present in between the last active layer of the Target and the first of the HCAL, so that they can be directly cross-calibrated.

Deviations from linearity are observed in SND@LHC for showers originated in the final depth (about 1 λ_{int}) of the Target and energies larger than 150 GeV (Figure 27). In such events the deposited energy is maximal in the initial section of the HCAL, the first 3 λ_{int}, and the collected light in those layers can saturate the readout (RO) electronics of the Silicon PMs. This effect can be mitigated with a finer granularity of the scintillating bars.

In very energetic ν_μ interactions, the hadronic shower development can leak in the muon detectors, which constitute the most downstream section of the SND@LHC HCAL and which exploit the same scintillator technology. For these rare events, muon tagging becomes less performant; an additional detector further downstream, using an independent ad-hoc technology, can improve the efficiency (see Section 2.5).

ν_e interactions in the Target as well as ν_τ with subsequent $\tau \to e$ decay produce concurrent electromagnetic and hadronic showers. The latter extend longitudinally much further than the former. Therefore, good reconstruction of the shower centroid in the HCAL, with about 1 cm accuracy, is critical for disentangling the electron shower.

Figure 26: Energy measurement calibration of the SND@LHC test detector in the H6 test beam of the CERN North Area (NA): (top) Digitized charge deposit (QDC) in the active layers of the Target (SciFi) vs QDC in the HCAL active layers (US) for 180 GeV pions; (bottom) Calibrated total energy distribution.

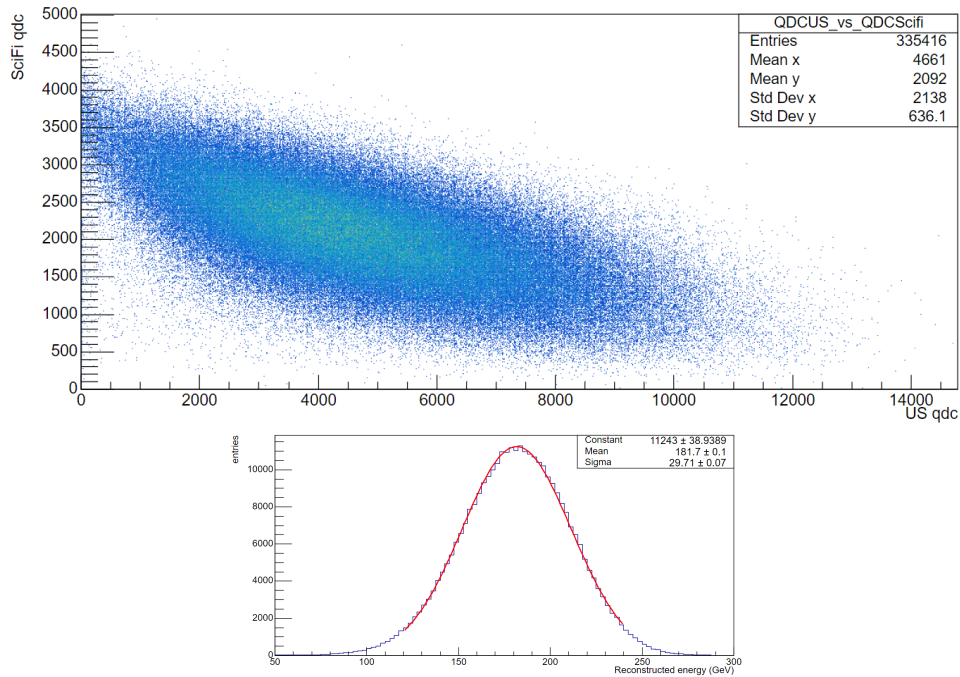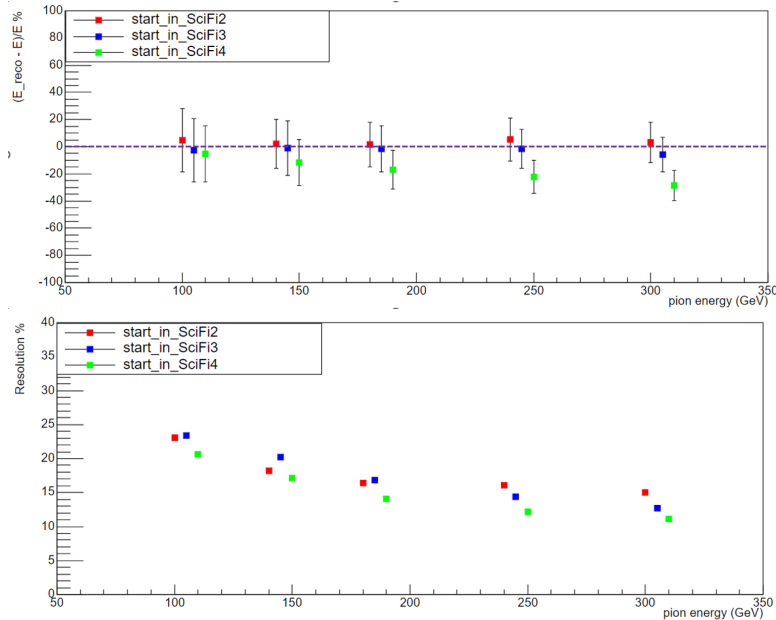Figure 27: Energy measurement calibration of the SND@LHC test detector in the H6 test beam of the CERN North Area (NA): (top) response linearity and (bottom) resolutions for 100, 140, 180, 240 and 300 GeV pions. Differently from the SND@LHC set-up taking data in LHC, the test detector in NA had only three Target walls, instead of five.

2.4.2   HCAL Overview

We propose a very mild upgrade of the SND@LHC HCAL, for use in AdvSND. In most parts, the existing detectors will be re-used, albeit in a new configuration. The active layers of the AdvSND HCAL will consist of scintillating bars, interleaved with iron absorbers and read out with SiPMs.
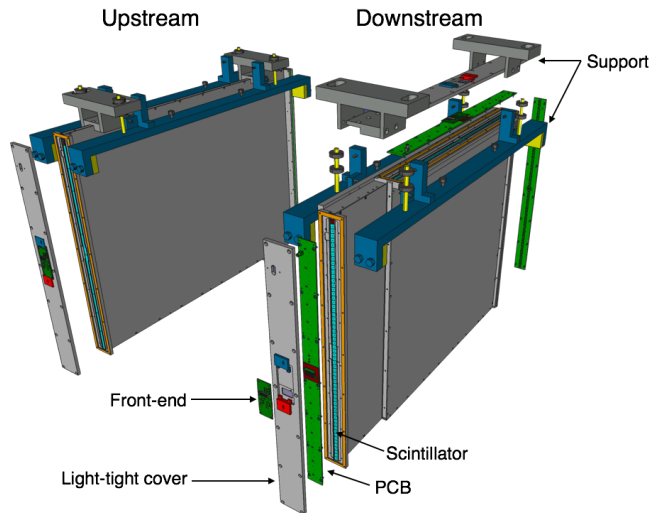

Figure 28: Upstream Station (US) (single plane of large scintillating bars) and Downstream Station (DS) (two planes (horizontal and vertical) of thin scintillating bars). There are five US and three DS stations (plus a fourth with only one plane) installed in the current SND@LHC detector.

An iron thickness of 200 cm is required to build up the ten units of pion interaction length deemed necessary for containing the most energetic hadronic showers. However, a large fraction of showers for the interesting events are initiated in the Target. As discussed in Section 2.4.1, the granularity of the scintillating bars within the active layers and the longitudinal segmentation of the absorber need to be optimized together with the thickness of the Target. Studies are ongoing that take into account the constraints on the space available for AdvSND in the LHC TI18 site. If a shower originates in the most upstream, middle or most downstream layer, it will be contained within about 4, 7 or 10 λ_{int} of the HCAL, respectively.

The radius of the lateral shower profile for an average energy containment of 85% is predicted to be one λ_{int}, i.e. 10 cm in W, 17 cm in Fe. The HCAL transverse size should exceed the Target dimensions by at least 10 cm on all sides. The Target acceptance is 40×40 cm^2.

The Upstream and Downstream Stations (US, DS) (Figure 28) of the SND@LHC HCAL and muon filter will be fully recycled. There are five US stations, each made of a stack of 6 cm wide bars, 1 cm thick, horizontally aligned and filling an area of 60×80 cm^2. There are four DS stations, each consisting of 1 cm thick bars arranged in two planes, except for the fourth which has only one plane: in three out of seven planes the bars are stacked horizontally (DSH), in four the bars are vertical (DSV). A DSH plane fills an area of 60×80 cm^2, while a DSV subtends 60×60 cm^2.

The twelve planes US+DSH+DSV of scintillating bars will be used to populate twelve layers of the AdvSND HCAL (Figure 29). The transverse area is 60×60 cm^2, and the entire length fits in 230 cm. The finer scintillator granularity of the thin bars in the initial layers downstream

the Target provides a good shower centroid measurement and prevents saturation effects in the electronics. H and V planes alternate. Up to a depth of six pion interaction lengths, the absorber layers are 0.5 λ_{int} thick, while beyond that they are 1 λ_{int}. In the middle region four layers of scintillating tiles are introduced.
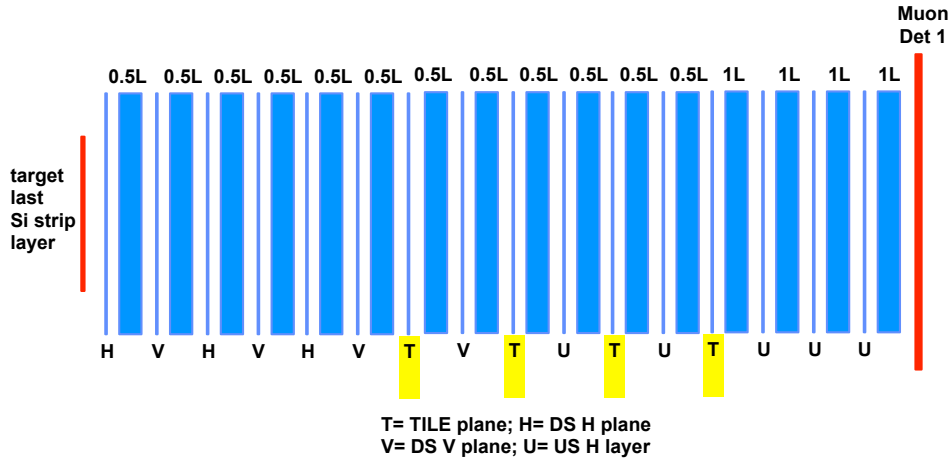

Figure 29: Sketch of the HCAL proposed for AdvSND. In most parts, the existing detectors US and DS of the SND@LHC HCAL will be utilized, but in a novel configuration. The four T layers are new detectors consisting of large scintillating tiles.

Each of the four planes with scintillating tiles are expected to have a matrix of 6 by 6 tiles of $10 \, \text{cm} \times 10 \, \text{cm}$, each tile will have a Wavelength Shifter (WLS) Fiber (BCF-91a, 1 mm diameter) embedded in it, and this WLS will be glued to improve the refractive index transition. The light collected by the WLS is transported to the edge of the plane and readout by a SiPM. Every tile will be wrapped to keep light tightness and opacity. The length of each WLS needs to be kept fixed for all tiles, no matter the distribution inside the plane to keep the same light attenuation. The extra length is kept behind the tiles (see Figure 30 Left). The HCAL for NA64 [22] was made in a similar way. Each SiPM signal can be readout by a 64-channel TOFPET ASIC. A front-end card will contain 36 SiPMs (see Figure 30 Right) and 2 TOFPET connectors.

The front-end and read-out electronics for the H, V and U planes will be recycled from the DSH, DSV and US electronics of the SND@LHC detector. New electronics will be designed for the four tile planes.

In AdvSND we also envisage to magnetize the iron of the HCAL (see Section 2.6). A coil will run through all layers. The HCAL should fit inside the coil and the FE electronics will have to be accommodated within the magnet volume; different solutions are being studied.
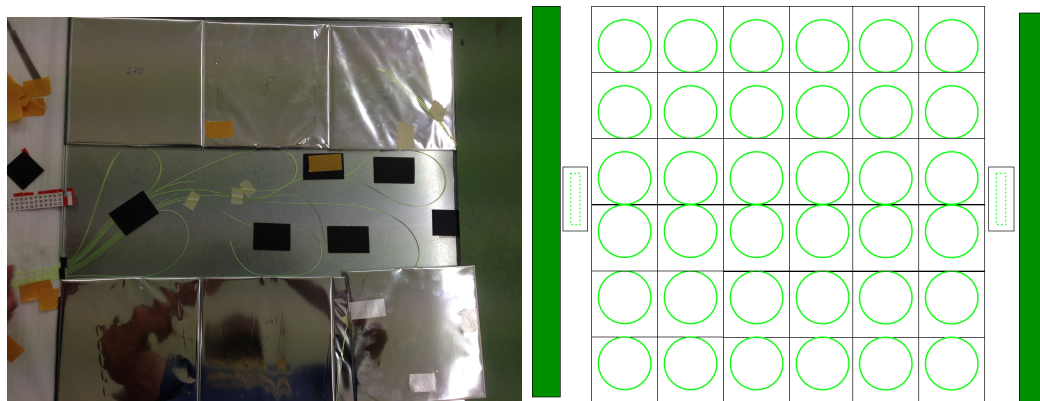
Figure 30: Left: Array of scintillating tiles exposing wavelength shifter routing inside one layer of the HCAL, Right: Sketch of a scintillating tile layer. The exit of the WLS are in the center on each side, reading out 18 tiles per side (36 fibers). Readout PCB in green, and in the middle a plastic matrix which contains all the WLS to be lined up with SiPMs.

Cost estimate   The estimated costs for the HCAL are summarized in Table 5.

	Quantity	Value (CHF)	Cost (CHF)
US+DSH+DSV planes	12		
Scintillating bars	650	47750	-
SiPMs	1200	35329	-
FE PCBs	20	10500	-
Mechanics	9	15000	-
Tile planes	4		
Scintillating tiles + WLS	144		14400
SiPMs	288		8640
FE PCBs	8		4200
Mechanics	4		6600
TOTAL HCAL		108579	33840
DAQ electronics			
DAQ boards for H+V+U planes (including TOFPET ASICs)	6	26100	
RO PCBs for H+V+U planes and cables	20	2800	
DAQ boards for T planes (including TOFPET)	2		4350
RO PCBs for T planes and cacles	8		1120
CAEN PS			
Mainframe	1	5400	
Mainframe booster	1		1400
LV channels	8		3300
available HV channels	30	11400	
new HV channels	12		3765

Table 5: Value of the existing HCAL system and estimated cost of its upgrade. Spare parts are not included. DAQ electronics and power supply costs are to be counted in the DAQ costs.

2.5 Muon Spectrometer

We plan to equip the spectrometer with Drift Tubes providing the required spatial resolution. In the collaboration there is established expertise in this domain: the Hamburg group built the drift tubes for OPERA and INFN teams built the barrel Drift tubes for CMS [23, 24]. Some existing prototype chambers built for CMS, and described below, could be reused while the geometry of our spectrometer will require building some from scratch. The CMS 'MiniDTs' were built in INFN Legnaro Laboratories, using the same design and materials as for the Drift Tubes chambers for the CMS detector. MiniDTs were used in test beams [25] and cosmic ray telescopes in Legnaro [26] and Bologna [27], and proved to be robust, low noise and easy to operate.

One MiniDT consists of 4 layers of 16 drift tube cells, of rectangular cross section, for a total of 64 channels. Adjacent layers are staggered with a relative shift of half cell width, ensuring standalone tracking and time tagging capability. Chambers are operated with a mixture of Ar (85%) and CO_2 (15%) at atmospheric pressure. The sensitive area is about 65×70 cm^2, while the external footprint, including internal high voltage distribution and front-end electronics and the aluminium enclosure, is about $75 \times 85 \times 8$ cm^3.

Single hit resolution is about 250 μm [28]; track reconstruction in a single MiniDT (using four layers) achieves a position resolution of about 150 μm and a direction resolution of about 10 mrad.

2.5.1 Baseline option: magnetic spectrometer

Two chambers spaced at least 25 cm can be used to achieve a direction resolution better than 1 mrad in the bending plane. Assuming a dipole field with $L = 1.6$ m and $B = 1.75$ T and two such direction measurements, before and after the magnet, a momentum resolution term of $\delta p/p \simeq 15\%$ will be achieved averaged over the expected momentum spectrum.

Before the dipole magnet, one additional MiniDT measuring the non-bending coordinate will allow a precise $x - y$ measurement of the muon trajectory for improved matching with Tracking and HCAL systems.

After the dipole magnet, a larger sensitive area (about 90×70 cm^2) is foreseen and two MiniDTs with more channels will be needed. The proposed configuration, with the MiniDTs in green, is shown in Figure 5. It consists of:

- a first station consisting of a pair of MiniDTs with perpendicular wires, providing an optimal $x - y$ position measurement, right after the HCAL;

- a gap of about 35 cm followed by a second station built with a single MiniDT with vertical wires right before the muon dipole;

- a third station right after the muon dipole, consisting of an increased-size MiniDT with vertical wires;

- a fourth and last station identical to the third one, after a gap of 25 cm.

.

As an alternative, the last two stations could be built using 4 small MiniDTs in a staggered configuration to avoid dead areas or a fullsize drift tube chambers developed on purpose.

Each MiniDT includes electronics for internal HV distribution, front-end boards and a control/power interface. No cooling is needed. Front-end electronics generates one discriminated signal per channel, in Low Voltage Differential Signal lines (LVDS). In summary, each MiniDT is operated with the following infrastructure:

- Low Voltage power: 12 Volts, < 10 W;

- High Voltage: a minimum of three channels providing for anode (+3600 V), cathode (−1200 V) and strip (+1800 V) voltages;

- Gas: Ar/CO_2 85/15 at atmospheric pressure, a flux of about 1 l/h per MiniDT ensures one volume per day of fresh gas;

- Slow Control: I2C interface to configure front-end thresholds, widths, and masking of individual channels;

- Readout: triggerless time to digital conversion with resolution $\lesssim$ 1 ns.

The proposed configuration would thus require 15 (21) HV channels, about 7 l/h of fresh gas (e.g. a standard bottle of premixed lasting between 2 and 3 months) and a readout system for 384 (448) channels, where numbers in brackets refer to the alternative solution with 4 standard-size MiniDTs in the last two stations.

2.5.2 Minimal option: no magnetic spectrometer

If no magnet is present, a Muon Tagger could be implemented using a single measurement station, implemented with two MiniDTs with perpendicular wires, as in the first station proposed in Section 2.5.1.

Cost estimate A total of 8 MiniDT chambers were built and are available; only repairs of broken channels and recommissioning will be needed. This is sufficient for the baseline option, which is assumed in the following cost estimates.

For the High Voltage and Low Voltage needs, a single CAEN system composed of one small mainframe, three HV boards and one LV board is needed, for a total cost of about 15 kCHF. In addition, about 2 kCHF will be needed to produce further on-chamber LV and control boards, as not all available MiniDTs are presently equipped.

The readout system can be based on the reuse of CMS modules: two "OBDT" [29] boards for the time-to-digital conversion and a single back-end board developed for the present CMS integration tests. Such a system is able to stream hits to a server in triggerless mode. It will also be possible to generate a trigger, if needed, by adding to the back-end firmware an adaptation of trigger algorithms developed for CMS Drift Tubes.

Additional costs for the integration of services with the MiniDT chambers, such as power, front-end and test pulse cables, and gas piping, are estimated to be about 5 kCHF. If new chambers were to be built to match better the acceptance at the back of the magnet the cost is estimated to be < 40 kCHF.

2.6   Magnetic spectrometer system

In this Section we summarize the main features of the proposed magnetic spectrometer system. Its design is optimized to be compact due to stringent space constraints in the TI18 cavern, to have adequate performance and to minimize power consumption and the usage of raw materials. More details on the design are given in Reference [30], where all the major choices are discussed and the analytical and semi-analytical optimization framework is detailed. To save space, part of the magnetized region was integrated into the HCAL. An iron core magnet is adequate, given the expected muon momentum distribution, as the effect of multiple scattering on the overall detection accuracy is acceptable. Therefore a design with two iron core electromagnets is proposed, as drawn in Figure 31.

2.6.1   Muon identification performance

In order to benefit from the large statistics, the magnets shape and cross section have been adapted to the expected angles of muon tracks from neutrino interactions in the Target from GEANT4 simulations. This results in a muon geometrical acceptance above 90 %.

    In this configuration the muon charge identification efficiency and muon momentum resolution have been studied simulating muon neutrino Charged Current (CC) interactions in the Target region. Neutrinos produced by charmed hadron decays are considered here, since they are the main signal sample. Their momentum spectrum is much harder than the corresponding spectrum of all muon neutrino interactions (see Section 4). Assuming a position resolution of $100\,\mu$m for all tracking stations, a muon charge identification efficiency of about 80 % is estimated with a 3 sigma cut. Notice that the uncertainty of 100 μm includes also the contribution from the alignment procedure.

    An overall muon momentum resolution of about 17 % is achieved as shown in Figure 32. It is relatively constant as a function of the true muon momentum. For neutrinos from charmed hadrons the muon momentum resolution is about 18 %.

    There are three main sources of error in the measurement of the momentum, namely: *i*) the energy loss, *ii*) the deflection of the muon due to multiple scattering, *iii*) the finite position resolution of the trackers.

    Energy loss mostly affects the low energy muons and causes a systematic error in the measured momentum. The scattering error causes a uniform reduction of the resolution independent
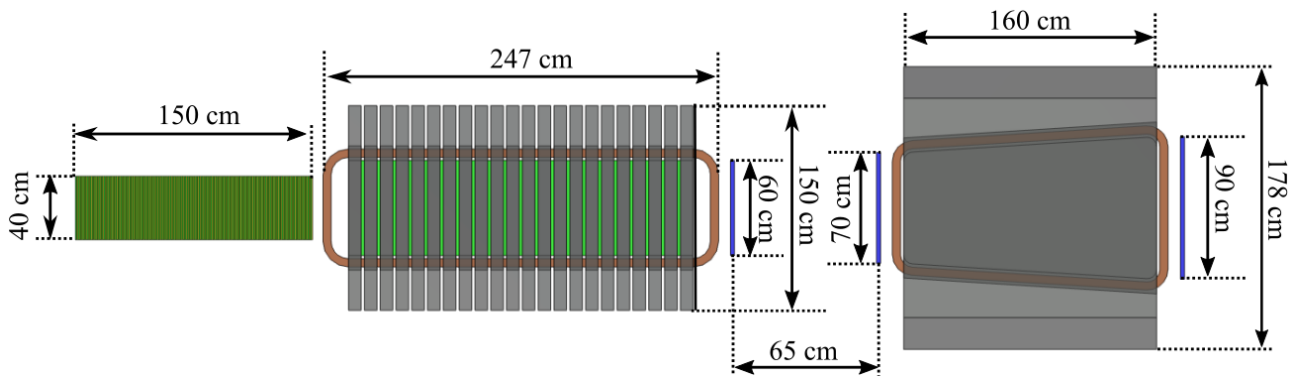

Figure 31: Schematic layout of the proposed integrated magnetic system for AdvSND.

from the momentum. Finally, the finite resolution of the trackers introduces an additive error on the measured displacements recorded by the detectors. The resolution error mostly affects high momentum muons, with measurable momenta up to 1000 GeV/c.

The choice of a iron core magnet (as opposed to air core) came from space optimization and power consumption (air core would require power of MW instead of kW) given that the multiple scattering is a subleading effect at the LHC energies.
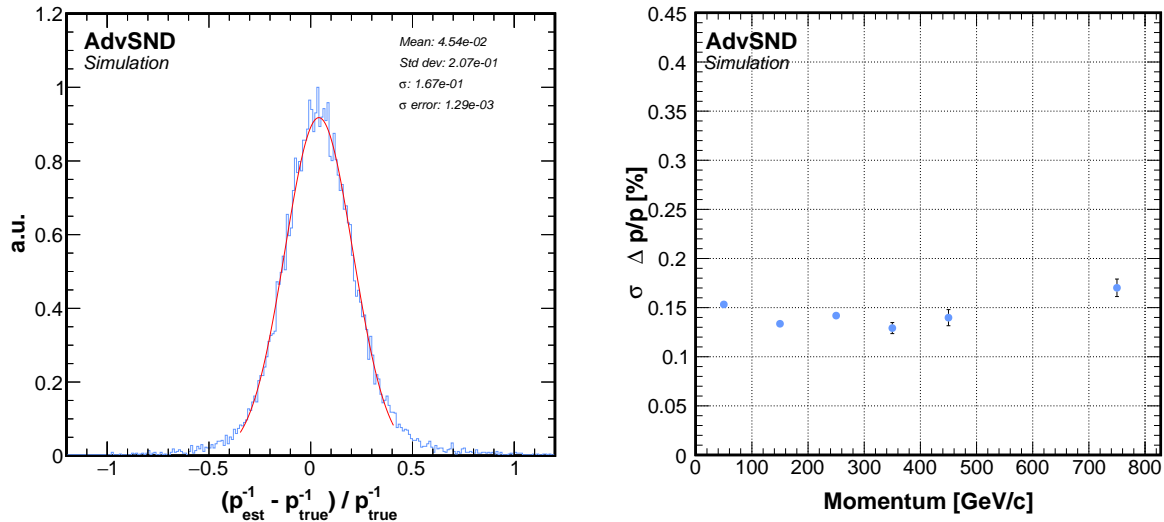
(a) *Overall muon momentum resolution* (b) *Momentum resolution w.r.t. momentum*

Figure 32: Muon momentum resolution achievable by the spectrometer system as estimated by GEANT4 simulation of ν_μ CC interactions in the Target: (a) overall and (b) as a function of the true momentum of the muon.

2.6.2 Iron core magnetic properties

The proposed iron core magnet solution requires a careful management of the iron quality choice, as proper modeling into the field simulation, staying critical for the correct prediction of the useful region field map and to cost issues. The choice is presently a weakly saturated iron: this will reduce the field uncertainties and limit the stray fields around the magnet. Concerning the magnetic characteristics of candidate iron types, we adopted the same conservative assumption as in Reference [31]. Figure 33 shows the H-B characteristic for the best case (ARMCO ATLAS) and worst case (ST1010 ATLAS) of commonly used iron materials. The choice between these iron qualities significantly impacts the required electric current and power consumption, with ARMCO being superior, but also significantly more expensive. On the other hand, approaching the saturation region the differences in the two magnetic characteristics tend to diminish, as expected. Given the limited expected power consumption of both magnets of the spectrometer system, AISI 1010 or a European equivalent grade iron can be an economical and, at the same time, acceptable choice. A working point is assumed for both magnets ($H \approx 9$ kA/m), where most of the H-B curves for AISI 1010 sheats, including ST1010 ATLAS, converge to a similar range of flux density values ($B \approx 1.7$ T).
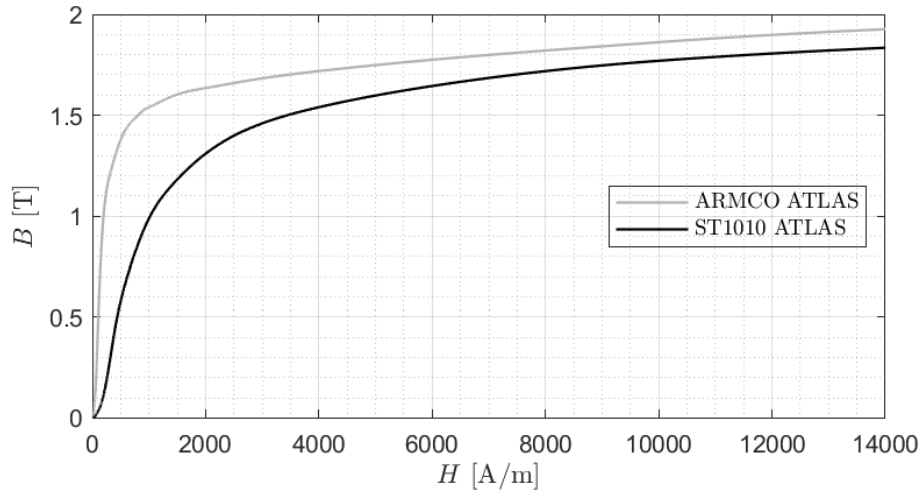
Figure 33: Best case (ARMCO ATLAS) and worst case (ST1010 ATLAS) *H-B* characteristic of iron materials commonly used to build experimental magnets.

2.6.3 The Hadron Calorimeter Magnet

The Hadron Calorimeter Magnet (HCM) has a parallelepipedal geometry with 22 magnetized iron slabs, each 8 cm thick, interleaved by 2 cm wide gaps designated for the placement of electronic detectors. The HCM foresees a 60×60 cm^2 magnetised active region where the reference flux density is 1.76 T, horizontally oriented with a computed field inhomogeneity $\Delta B/B$ smaller than 3% in 98% of the section. In Table 6 the most significant design parameters are reported, as well as all dimensions, mass and main electrical parameters. More details are given in Reference [30]. In Figure 34 the Finite Element (FEM) mesh and the simulation results for the magnetic flux density are shown.

Description		Value
Total longitudinal length (iron + gaps + coil)	[m]	2.54
Total magnetized longitudinal iron core length	[m]	1.76
Total cross-section	[m^2]	1.20×1.50
Core cross-section	[m^2]	0.60×0.60
Reference flux density (magnetized core)	[T]	1.76
$\Delta B/B$ @ 98% volume	[%]	≤ 3
Stray field [@ iron surface, @ $d >$2m]	[mT]	$[\lesssim 10 \lesssim 1]$
Current density	[A/mm^2]	0.75
Magnetomotive force	[kA]	18
Electrical power	[kW]	1.5
Total conductor mass	[t]	1.3
Total iron mass	[t]	22.5

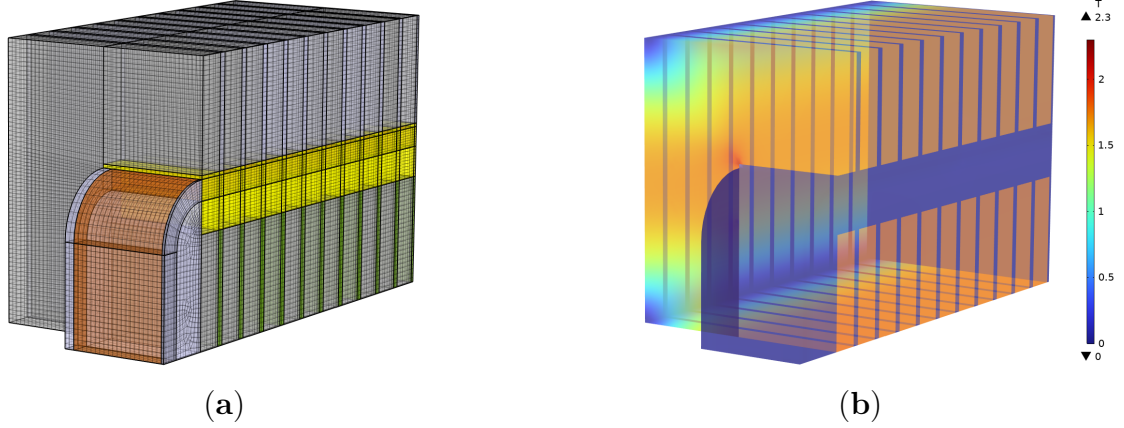Table 6: Main parameters of the Hadron Calorimeter Magnet (HCM).

Figure 34: Mesh of the HCM components: brown=coil, yellow=coil insulation and auxiliaries; green: particle detectors; gray=iron core. Magnetic flux density for the Calorimeter Magnet (expressed in [T]). The field distribution inside iron and coil is shown.

2.6.4 The flux-symmetric conical Muon System Magnet

The second part of the magnetic spectrometer system, namely the Muon System Magnet (MSM) has a special configuration, that we call *flux-symmetric conical*. Its shape is specifically designed for magnets with sloping cores, aiming to minimize their overall volume. The proposed MSM exhibits a magnetized sloping core with a reference flux density of 1.75 T in the same direction as the HCM with an overall field inhomogeneity $\Delta B/B$ lower than 3 % in 94% of the active volume.

In Table 7 most significant design parameters are reported, as well as all dimensions, mass and main electrical parameters. More details are given in [30]. In Figure 35 the FEM mesh and the simulation results for the magnetic flux density are reported.

Description		Value
Total magnetized longitudinal iron length	[m]	1.60
Total cross-section (both upstream and downstream)	[m²]	1.60×1.78
Core upstream cross-section	[m²]	0.70×0.70
Core downstream cross-section	[m²]	0.90×0.90
Return yoke thickness [upstream downstream]	[m]	[0.45 0.35]
Reference flux density (magnetized sloping core)	[T]	1.75
$\Delta B/B$ @ 94% volume	[%]	≤ 3
Stray field [@ iron surface, @ $d >$2m]	[mT]	[$\lesssim 10 \lesssim 1$]
Current density	[A/mm²]	0.74
Magnetomotive force	[kA]	21.0
Electrical power	[kW]	1.5
Total conductor mass	[t]	1.25
Total iron mass	[t]	33

Table 7: Main parameters of the Muon System Magnet (MSM).

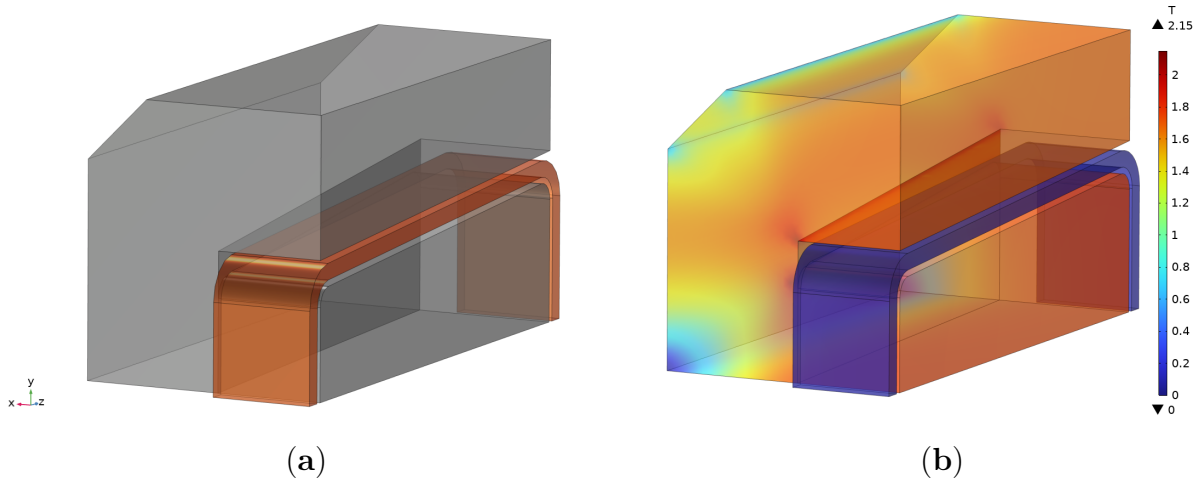(a)   (b)

Figure 35: (a) 3D view of one quarter of the whole magnet: in grey, the iron yoke; in orange, the coil. The surrounding air domain is not sketched here. (b) Modulus of magnetic flux density for the muon system magnet (expressed in [T]). The field distribution inside iron and coil can be appreciated.

Both coils are characterized by a sufficiently low current density (0.74 A/mm^2), so that air cooling is possible and standard CERN power converters can be used.

2.6.5 Construction constraints

Coil cooling Due to the low power requirements (1.5 kW) of both the MSM and HCM iron core magnets, and the large available heat exchange surfaces, it has been possible to design the coil for air cooling. This design choice simplifies the coil construction and enhances reliability. The considered current density of 0.75 A/mm^2 is significantly lower than typical values for air cooled normal conducting magnets (1 A/mm^2), ensuring that natural convection is adequate to maintain a sufficiently low temperature during steady-state operation, to avoid the overheating of sensitive components.

Mechanical issues and magnet segmentation As already mentioned, the TI18 tunnel location imposes strict dimensional constraints on the magnetic spectrometer system. Additionally, the tight tunnel and limited access openings pose challenges for the magnet assembly, with upper bounds on the dimensions of single pieces and a maximum weight limit of 1.2 tons per piece due to the crane facilities. Consequently, segmentation of the iron slices and, possibly, of the coil itself has to be considered.

As for the HCM, each single 8 cm thick slab has a mass of 1.02 tons, so naturally fitting the crane load limits. Moreover, due to construction issues, the need for accommodating the coil and the assembling/maintenance of detectors, each slab is conveniently divided into two parts, as shown in Figure 36.

With respect to the MSM, a longitudinal splitting into 32 slabs, each one 5 cm thick, is currently planned. Also in this case, the iron slabs are conveniently divided in two parts each, possibly with same shape as for the HCM. The maximum weight never exceed 1.0 tons, again meeting the crane load limits.

Final considerations are due with respect to the coils, at present of 1.3 tons (HCM) and 1.25 tons (MSM), respectively, that are slightly above the crane load limits. They can both, in principle, be divided in two separate parts to be electrically connected in series, without any big new effort required from the design point of view. Alternatively, one can consider an aluminium solution for the coil, at the price of a larger coil height (a solution that has up to now been discarded for limiting the maximum size).
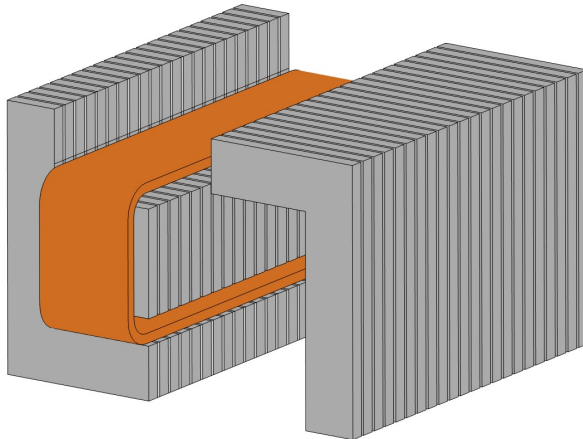

Figure 36: Segmentation of the whole HCM magnet with an upside-down F-L structure.

Cost estimate   A preliminary cost estimate is given for the HCM and the MSM AdvSND spectrometer magnets. It follows the standard approach [32] that was also used for the SHiP experiment [31]. The choice of iron core, with the corresponding electrical power (in the order of 1-2 kW), renders the power related operational costs negligible, and consequently only material costs are considered.

The supply cost is evaluated basing on present day pricing of raw materials, with specific (standard) manufacturing factors, specific for iron (magnetic structure) and copper (coil) respectively.

The estimated costs for the spectrometer system magnets are given in Table 8. It has to be noted that cost therein indicated for the power converter components is small (approximately estimated as 10–12 kCHF), since it only covers four DCCT high-accuracy current measurement units, two control electronic modules and some minor upgrade to refresh the converters, which will be provided by the CERN SY-EPC-LPC power laboratory. The other required components are readily available at CERN and can be recovered to be used for AdvSND.

2.7   Online System

This Section provides an overview of the online system concepts and data flow upgrades, in particular for Data-Acquisition (DAQ), Experiment Control (ECS), Detector Control (DCS), LHC signals and the new Trigger (TS).

The SND@LHC Online System was designed to maximize reliability and robustness during data taking and ensuring high efficiency in recording the physics processes generated during collisions. These requirements, and the location of the front-end readout (TI18) are further

	Unit cost	Units	Manufacturing factor	Cost
Hadron Calorimeter Magnet				
Coil (copper)	7.4/t	1.3 t	3	29
Magnetic structure (iron)	1.6/t	22.5 t	4	144
Muon System Magnet				
Coil (copper)	7.4/t	1.25 t	3	28
Magnetic structure (iron)	1.6/t	33 t	4	211
Power converter components (see text)				≈ 12
Total				424

Table 8: Cost estimates in kCHF for the magnets of the spectrometer system.

complicated by the fact that the experiment was designed to be operated remotely, with the shifter not necessarily located in a control room.

The SND online system is based on a modular architecture (Figure 37) that allows the integration of new subsystems. A more detailed description of the Online System (hardware
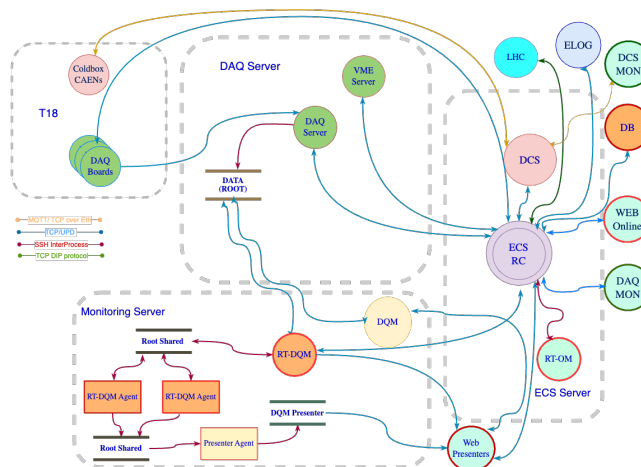

Figure 37: Simplified scheme of the SND@LHC Online system.

and software) operating in TI18 can be found in Reference [2].

The Online System can be grouped into two major categories Readout and DAQ, and Experiment Control.

2.7.1 Readout and DAQ Systems

The data acquisition system is triggerless and uses identical electronics for all detectors. This approach is not applicable to AdvSND since some detectors cannot be readout with similar electronics, and furthermore, some require a trigger signal to initiate the readout chain. However, thanks to the modular architecture of the online system, we can separate the new detectors into separated subsystems by integrating the software primitive functions of the readout and hardware control from the original online system of the experiment.

For the silicon detector we plan a dedicated server to operate the readout and a buffer to store events locally, re-using part of the CMS Tracker DAQ software.

The new detectors need a fast trigger to operate, and this will be provided by the timing detectors. A trigger board will be developed. It will:

- interface to the Trigger Timing Control (TTC) system

- generate a fast trigger signal needed to start the readout chain of the silicon detector and the drift tubes

- create a trigger timestamp record

- transfer the data to the event builder

- if required. provide an accurate time stamp for a trigger to be sent to ATLAS

This board could be a modified DAQ Board from the current detector.

2.7.2   Beam synchronization

The LHC clock (40.079 MHz bunch crossing frequency) and orbit clock (11.245 kHz revolution frequency of the LHC) signals are obtained from the LHC Beam Synchronous Timing (BST) system via optical fibres based on the TTC system.
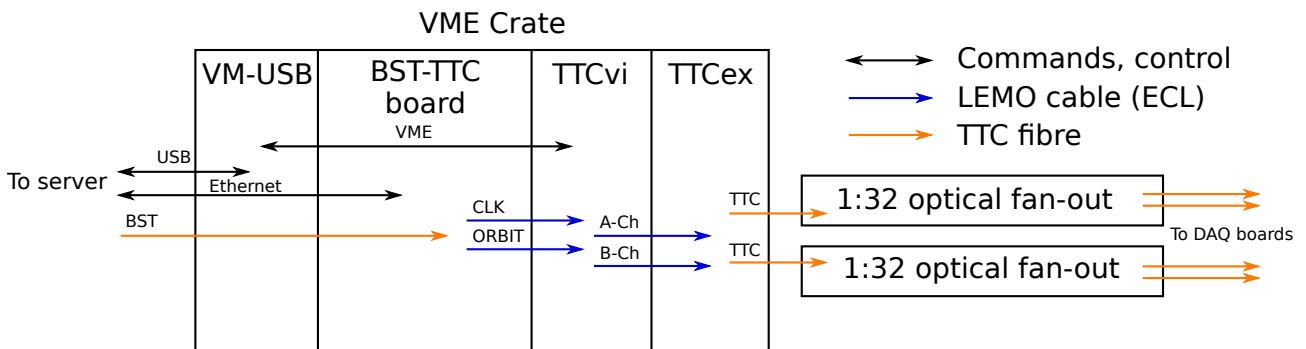

Figure 38: Simplified scheme of the SND@LHC TTC system.

The BST signal is received by a dedicated board, BST-TTC, that extracts the clock and orbit signals, cleans the clock using a Phase Lock Loop, and distributes them to the TI18 SND detector DAQ boards using the TTC system. This is necessary to have them run synchronously with the LHC bunch crossing. For the upgrade the timing system remains valid as almost all proposed detectors use the TTC either for trigger or for clock distribution.

2.7.3   DAQ Server - DS

The main function is to organize the dataflow from the detector up to the data storage. In the current detector, under the supervision of the ECS and the Run Control, the DS operates the dataflow (Figure 39). The front-end DAQ boards transmit all the recorded hits to the DS where event building is performed. Hits are grouped into events (1), based on their *timestamp*, filtered (2) and saved to disk as a ROOT file.
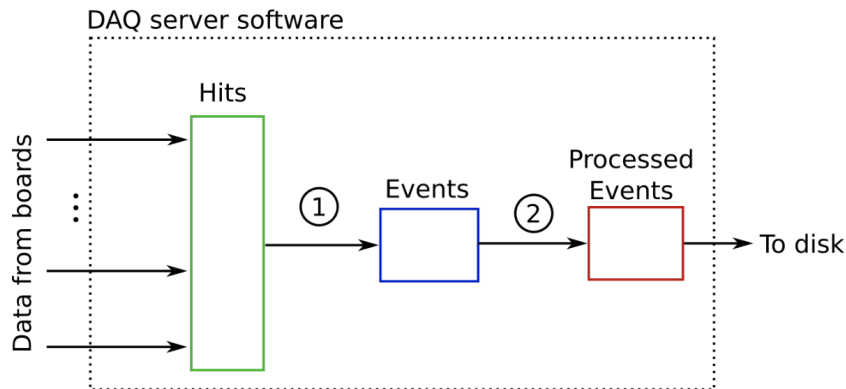
Figure 39: Schematic representation of the DS event builder.

In the upgrade all the detectors have a TTC system and thus the possibility to have a timestamp synchronized via TTC with the other detectors. In this case it could be possible to continue to operate the experiment like a trigger-less system. In this operating mode the readout dataflow can be easily implemented in the current online system architecture. This configuration needs two servers; the new one will be used for the silicon detector, the timing detectors and the drift tubes readout. On this server a local event builder will use the software packages inherited for the new detectors (i.e. from the CMS DAQ), and perform the readout of the front-end, storing events in a local shared memory buffer.

The current DS server will continue to function in its present configuration, but with events written in a local shared memory. We will introduce a Global Event Builder which will build the events from the two servers and write them to data storage via RDMA Ethernet (RoCE).

2.8 The Experiment Control

2.8.1 Detector Control System - DCS.

The DCS is in charge of controlling the detector services:the power-supplies, the cold box controller and the interface to the Detector Safety System (DSS).

In the present design the ECS has embedded DCS State Machines operating the control and monitoring of all sensitive sources (e.g. cooling, power, alarm) that can affect the data taking. DAQ and DCS monitoring agents, at low priority, monitor all the others sources in real time. All monitored DAQ and DCS sources are collected in an influx database and can be displayed on Grafana. In AdvSND we plan to adapt the current systems to operate the setup and monitor operations. We will need to monitor and control new sources and environmental conditions, like pressure and temperature for the drift tubes, the new detectors and the magnets.

2.8.2 Experiment Control System - ECS

The ECS is the top control level of the experiment's readout system, coordinating the software components and controlling all data taking operations. The ECS performs the LHC handshake, the monitoring of the sensitive sources for fast alerting and acting on hardware issues or alarms.

A hierarchical architecture is used, in which the ECS is a layer above the other online systems, preserving their autonomy to operate independently. With this architecture, the various online programs do not strictly require the ECS to operate (*e.g.* detector calibration and data taking are stand-alone processes) and new subsystem can be added in similar fashion.

The internal design and structure of the ECS will be maintained, albeit upgrading the GUI and adding new panels and adapting the Run control to deal with the new subsystems. The increase in complexity will require moving the ECS from the present Virtual Machine to a dedicated server.

Cost As we assume that we will recover (mainly from CMS) the electronics and infrastructure (like crates and racks) needed to readout and control the new elements, the cost will be dominated by the development of the new trigger boards and the acquisition of more powerful servers, and is estimated at less than 22 kCHF.

3 Detector integration

Integration studies have been performed to evaluate the feasibility of the AdvSND installation and the related impact on the current infrastructure. The proposed layout optimises the detector's acceptance with respect to varying crossing angle configurations and geometrical constraints, i.e. the TI18 tunnel's slope, height, and width. The baseline solution is shown in Figure 40.

The baseline proposal includes an enlargement of the tunnel area to allow the installation of the magnetic spectrometer. It also foresees a local crane which will enable handling the detector components during installation. Some services will need a local rerouting due to the new configuration of the experimental area. Figure 41 shows the TI18 enlargement with a rerouted drainage system. The detector will be accessible via stairs/ladder from the UJ18 level. The space between the detector and the contour of enlargement makes it possible to reach detector components for their maintenance. The MSM can be reached via a 1-meter-wide passage on the UJ18 side. The maintenance of the active layers of the HCM will be possible traversing the line of sight via a 0.7-meter passage available on the upstream side of the detector, see Figure 40. This figure also shows how we propose to reroute the ventilation duct. Cable trays will be routed along the side wall of TI18 as for the current detector. They will follow the curvature of the TI18 enlargement.

Studies were also done for the AdvSNDReduced configuration. In this case AdvSNDReduced is positioned such that no intervention is needed on the side wall of the TI18 tunnel. The installation of the detector requires the excavation of the floor: these modifications are needed for mitigating the effect of the sloping floor and to optimize the acceptance for neutrinos for the foreseen crossing angle configurations (see Figures 3 and 4). These modifications are shown in Figures 42 and 43. A crane or at leasts a jib crane will be required.

A study of how these modifications could be realized is ongoing. To not interfere with the HL-LHC and its schedule, the access to the experimental area will have to be through the TI18 tunnel from the SPS side. Preliminary inspections have shown that the tunnel is in good condition and the ongoing study is based on the assumption that all aspects related to transport and civil engineering access will be from the SPS side.
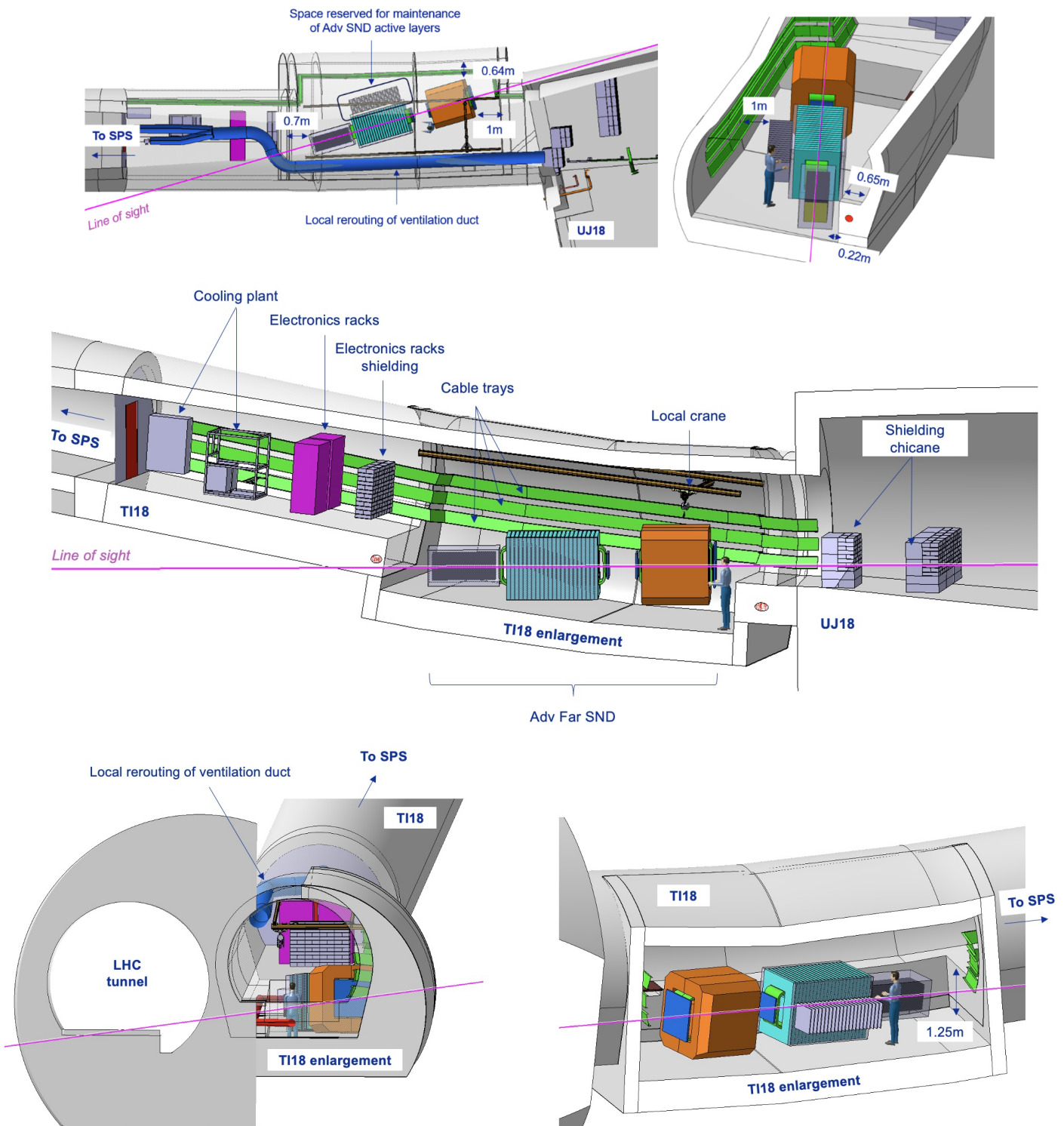
Figure 40: Various views of the baseline configuration. The rerouting of the ventilation duct and the layout of the local crane are also shown. The line of sight corresponds to the collision axis.
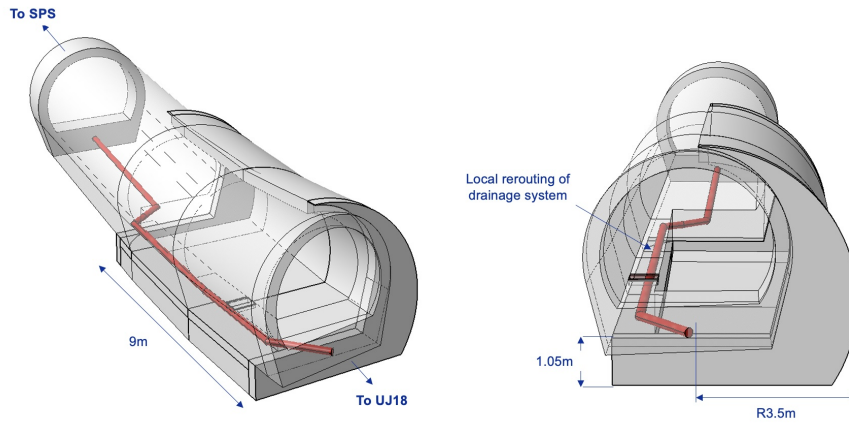
Figure 41: The AdvSND area in the baseline configuration, showing the rerouting of drainage.
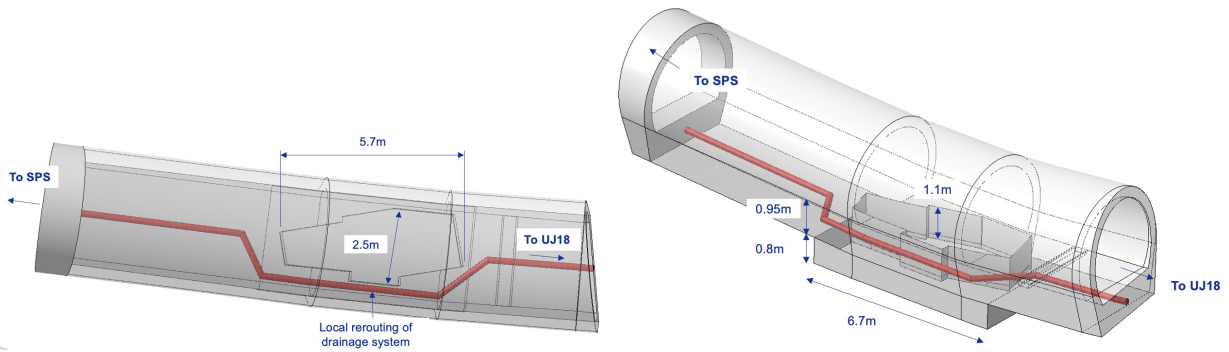

Figure 42: The minimal floor modification of the area presently occupied by SDN@LHC to optimize the acceptance under any crossing angle condition.
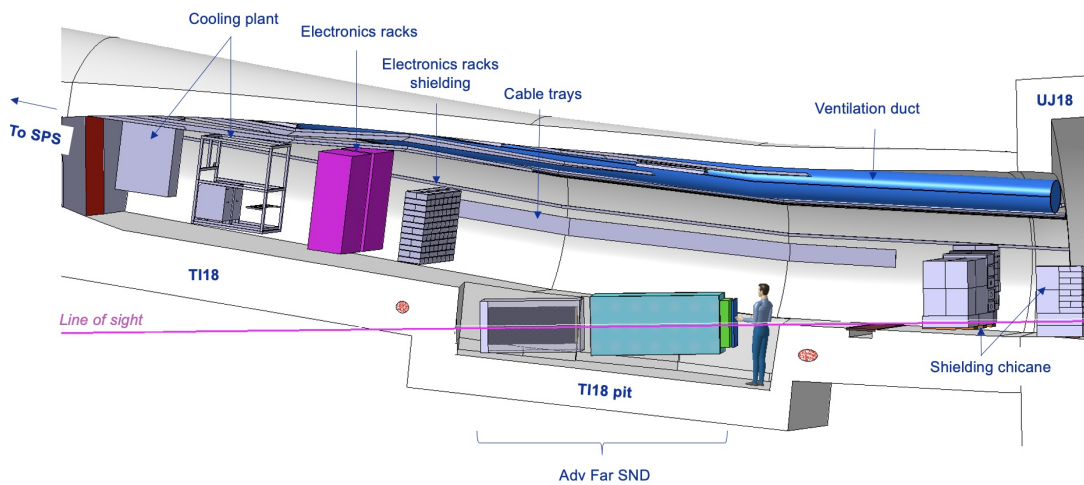

Figure 43: The experimental area for the AdvSNDReduced configuration. The line of sight corresponds to the collision axis.

4 Physics performance

4.1 Simulation software

The simulation of the AdvSND detector is handled by the FairShip software suite, developed within the SHiP collaboration, which is based on the FairRoot software framework [33].

Neutrino production in proton-proton collisions at the LHC is simulated with DPMJET3 (Dual Parton Model, including charm) [34] embedded in FLUKA [35, 36], and particle propagation towards the detector is done through the FLUKA model of the LHC accelerator in order to simulate also neutrinos from further decay of collision and re-interaction products. Figure 44 shows a view of the right side of the ATLAS insertion, as implemented in FLUKA, from the experimental cavern up to the TI18 gallery, whose slope rises from the LHC level towards the SPS. GENIE [37] is then used to simulate neutrino interactions with the detector material. The output of GENIE is input to Geant4 [38] for the particle propagation in the detector.

A model of the detector and the surrounding tunnel has been implemented in Geant4, as seen in Figure 45. The electronic detectors are implemented as sensitive volumes, with digitisation performed before the reconstruction to capture the physics of detector technologies. No mechanical supports besides the tunnel floor are included at this point.
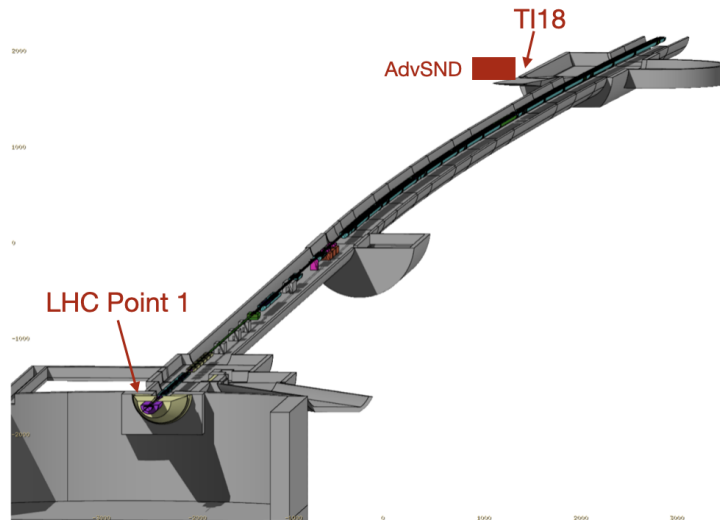

Figure 44: 3D view of the LHC Point 1 insertion towards TI18 as modeled in FLUKA. The geometry covers a length of about 500 m and includes, among others, detailed models of vacuum chambers, absorbers and magnets, provided with the respective field maps, aiming to reproduce the beam trajectory with a micron accuracy.

4.2 Muon flux

The DPMJET/FLUKA simulation for the estimate of the muon rate in TI18 has been validated using Run 3 data integrated in 2022 [4]. A 25% agreement between data and simulation was observed.

Positions and momenta of muons are recorded on a virtual scoring plane with an area of $3 \times 3 \, \mathrm{m}^2$ located 75 m upstream of the TI18 tunnel, in order to decouple the muon interactions in
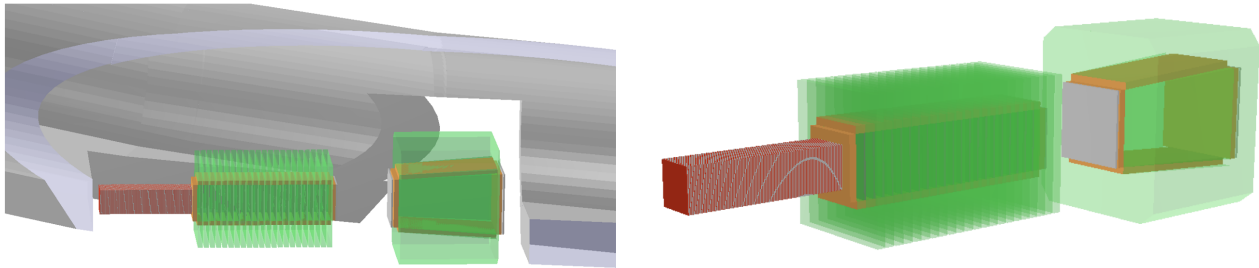
Figure 45: The AdvSND detector implemented in the GEANT4 simulation with the tunnel geometry (Left) and standalone (Right).

rock and concrete from the primary flux of muons produced at the IP and within the detector and LHC machine elements. Figure 46 shows the position of positive and negative muons at the scoring plane, while muon spectra in the AdvSND acceptance are reported in Figure 47. The integrated rate was estimated assuming an instantaneous luminosity $\mathcal{L} = 5 \times 10^{34} \text{cm}^{-2}\text{s}^{-1}$, that is the maximum luminosity expected in LHC Run 4. Expectations are reported in Table 9 for the Target, HCAL and Muon Spectrometer.

	Target (40×40 cm²)		HCAL (60×60 cm²)		Muon Spectrometer (90×90 cm²)	
μ^+	0.8 Hz/cm²	1.3 kHz	0.8 Hz/cm²	2.8 kHz	0.6 Hz/cm²	5.0 kHz
μ^-	2.4 Hz/cm²	3.8 kHz	2.0 Hz/cm²	7.2 kHz	1.3 Hz/cm²	10.5 kHz
total	3.2 Hz/cm²	5.1 kHz	2.8 Hz/cm²	10.0 kHz	1.9 Hz/cm²	15.5 kHz

Table 9: Integrated rates of muons entering in the acceptance of Target, HCAL and Muon Spectrometer.

4.3   Neutrino physics

The position of the detector was optimized to maximize the number of neutrino interactions for three possible configurations of the crossing angle: +250 μrad in the horizontal plane, +250 μrad and -250 μrad in the vertical plane. Figure 48 shows the ν_μ and ν_e interaction yields averaged over the three above mentioned configurations, evaluated for different positions of the Target center. The best configuration is the one with the Target center in $x = 2$ cm and $y = 4$ cm (see Figure 3 for the definition of the origin).

The baseline configuration for Run 4 contains a +250 μrad crossing angle in the horizontal plane. In this case the AdvSND detector covers a pseudo-rapidity region with $\eta > 7.9$ (see Figure 3, left). This configuration was used for the evaluation of the physics performance reported in this Section.

The spectra and the neutrino yield at the Target region for the three different neutrino flavours are reported in the left panel of Figure 49 and in the left column of Table 10, respectively. An integrated luminosity of 3000 fb^{-1} is assumed. The expected number of CC and
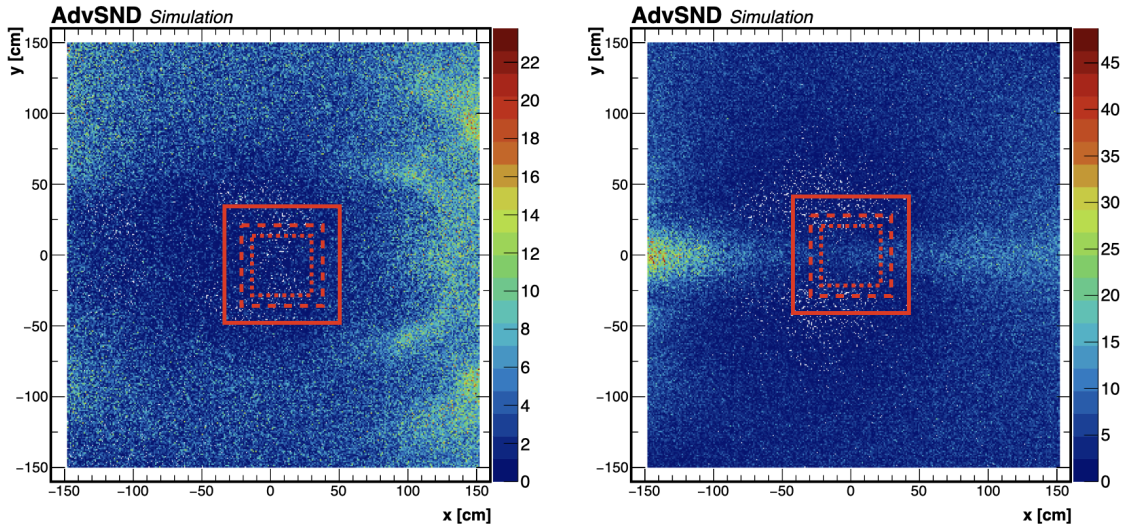
Figure 46: Position of positive (left) and negative (right) muons in the transverse plane, as recorded at a 3×3 m² scoring plane located 75 m upstream of TI18, as predicted with the DPMJET/FLUKA simulation of CERN EN-STI. Dashed and continuous lines represent the sensitive areas of the AdvSND Target and HCAL respectively.

Figure 47: Positive (left) and negative (right) muon flux in the AdvSND acceptance as a function of the energy as predicted with the DPMJET/FLUKA simulation of CERN EN-STI.

Figure 48: ν_μ (left) and ν_e (right) interaction yields as the average of the three crossing angle configurations, evaluated for different positions of the Target center.

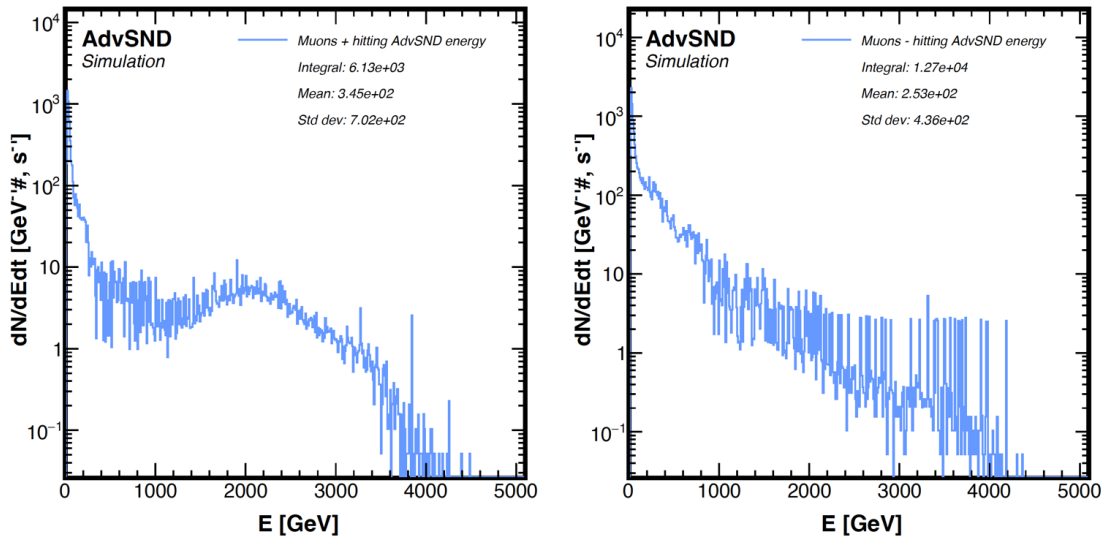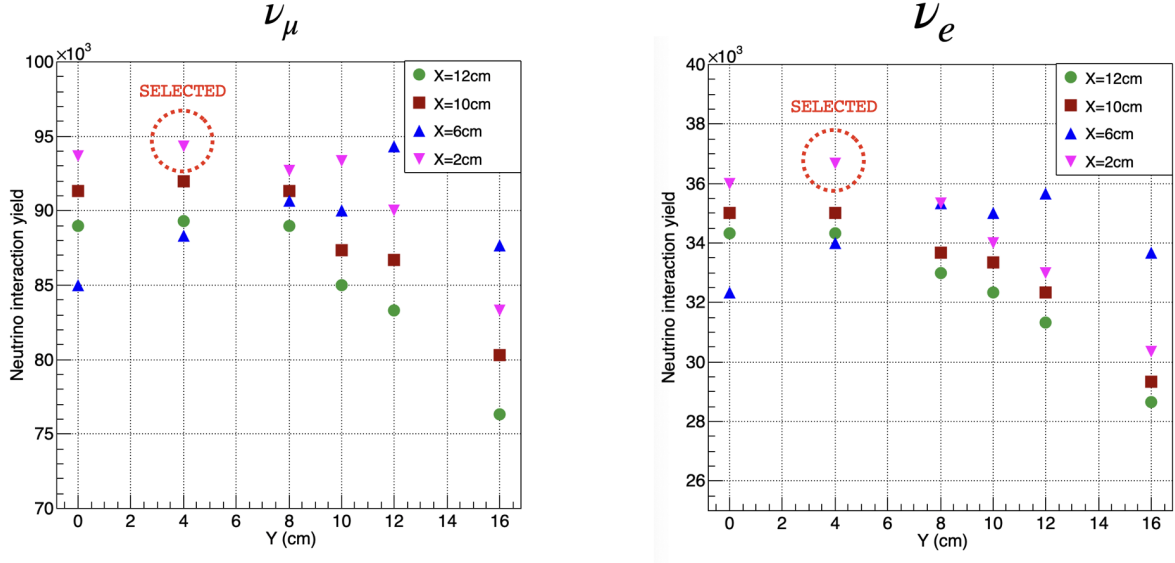Neutral Current (NC) neutrino interactions occurring in the detector Target assuming a 2 ton tungsten mass is reported in the central and right columns of Table 10, while energy spectra for Charged Current Deep Inelastic Scattering (CC DIS) interactions are shown in the right panel of Figure 49.

The neutrino component produced in charmed hadron decays was also estimated using the Pythia8 [39] generator activating hardQCD processes only, which provides a number of expected neutrino interactions a factor three less with respect to DPMJET.

It has to be noted that a large number of neutrino interactions will occur also in the HCAL. If we consider the portion of iron walls contained in the sensitive volume, having a transverse size of 60×60 cm^2 and a 4.5 ton mass, a total number of 2×10^5 muon neutrino CC DIS interactions are expected.

Flavour	ν in acceptance		CC DIS		NC DIS	
	All	not from π/K	All	not from π/K	All	not from π/K
ν_μ	8.6×10^{13}	8.2×10^{12}	1.2×10^5	3.3×10^4	3.6×10^4	1.0×10^4
$\bar{\nu}_\mu$	7.0×10^{13}	9.6×10^{12}	4.4×10^4	1.8×10^4	1.6×10^4	6.5×10^3
ν_e	1.3×10^{13}	9.1×10^{12}	4.2×10^4	3.6×10^4	1.3×10^4	1.1×10^4
$\bar{\nu}_e$	1.3×10^{13}	9.2×10^{12}	1.9×10^4	1.7×10^4	7.0×10^3	6.1×10^3
ν_τ	7.3×10^{11}	7.3×10^{11}	2.1×10^3	2.1×10^3	6.7×10^2	6.7×10^2
$\bar{\nu}_\tau$	9.4×10^{11}	9.4×10^{11}	1.2×10^3	1.2×10^2	4.6×10^2	4.6×10^2
Tot	1.8×10^{14}	3.8×10^{13}	2.3×10^5	1.1×10^5	7.3×10^4	3.5×10^4

Table 10: Number of neutrinos in the Target acceptance, CC DIS and NC-DIS neutrino interactions, assuming $3000\,\mathrm{fb}^{-1}$, as estimated with DPMJET+FLUKA and GENIE generators.
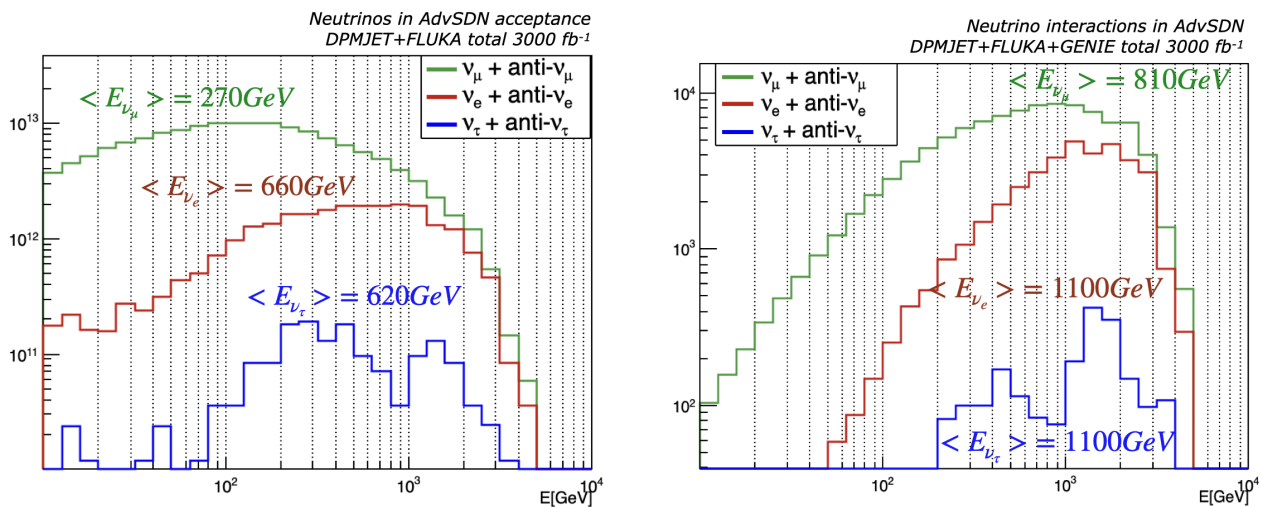
Figure 49: Energy spectra of the three neutrino flavours in the Target acceptance (left) and undergoing CC DIS interactions in the Target (right). The normalization corresponds to 3000 fb^{-1}. Average energies are also reported.

4.3.1 QCD measurements

Electron neutrinos in the AdvSND pseudo-rapidity range $\eta > 7.9$, are mostly produced by charm decays. Therefore, ν_es can be used as a probe of charm production in an angular range where the charm yield has a large uncertainty, to a large extent coming from the gluon parton distribution function (PDF). Electron neutrino measurements can thus constrain the uncertainty on the gluon PDF in the very small (below 10^{-5}) Bjorken x region. The interest therein is two-fold: firstly, the gluon PDF in this x domain will be relevant for Future Circular Collider (FCC) experiments; secondly, the measurement will reduce the uncertainty on the flux of very-high-energy (100 PeV) atmospheric neutrinos produced in charm decays, essential for the evidence of neutrinos from astrophysical sources.

The charm measurement by the current detector in Run 3 will be affected by a systematic uncertainty of 35% and by a statistical uncertainty of almost 10%. The operation in HL-LHC of the AdvSND detector will reduce the statistical uncertainty to about 1%, as is clear from Table 10. The large systematic uncertainty mostly comes from the procedure linking neutrinos to charm [1]. In order to reduce this uncertainty AdvSND will benefit from measurements performed by a proposed (for Run 5) *near* detector, which covers the pseudo-rapidity region $4.0 < \eta < 4.5$ (see Section 4.6). The comparison between neutrino measurements and LHCb direct charm measurements in that angular range [40] will allow reducing the systematic uncertainties, thus bringing this accuracy down to the level of the statistical one. Figure 50 shows charm production cross-sections in different η regions: the uncertainty of the gluon PDF provides the largest contribution.

4.3.2 Lepton flavour universality

The capability to identify all three neutrino flavours with the AdvSND detector offers a unique possibility to test Lepton Flavour Universality (LFU) in neutrino interactions. Muon-neutrino and electron-neutrino spectra in the AdvSND acceptance are shown in Figure 51. The compo-
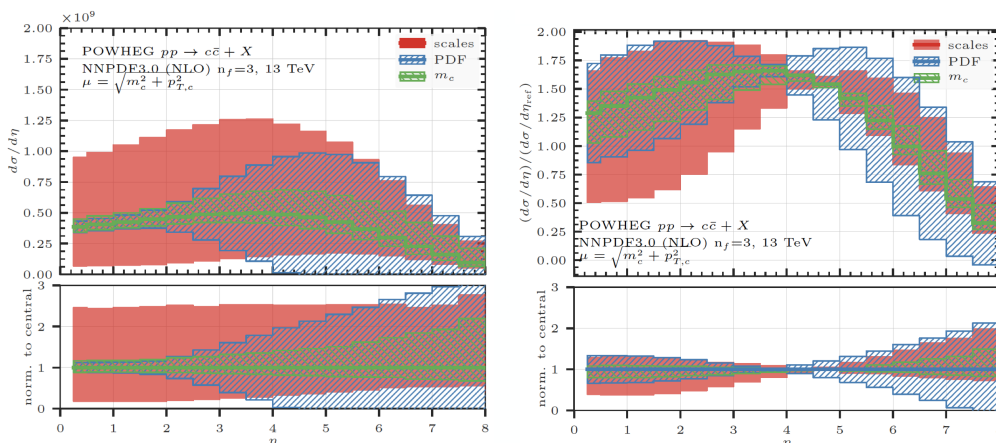
Figure 50: (Left) Differential cross-section for charm production at 13 TeV as a function of pseudo-rapidity. (Right) Ratio between the differential cross-section at 13 TeV and the differential cross-section at 7 TeV, with the latter evaluated in the pseudo-rapidity range $4 < \eta < 4.5$.

nent from heavy-quark decays is represented as the filled area.

The fraction of electron neutrinos produced in pion and kaon decays is about 30% of the total number at the Target. Due to their lower energies and hence lower cross-sections, the number of neutrino interactions from neutrinos from pions and kaons is reduced to 14%. Assuming that both tau and electron neutrinos come from the decay of charmed hadrons, the ν_e to ν_τ ratio depends only on the decay branching ratios and the charm fractions, thus becoming sensitive to the cross-section ratio of the two neutrino species and allowing for a test of the lepton flavour universality in neutrino interactions [1].

In the current run, the expected uncertainty of this measurement is dominated by a 30% statistical uncertainty due to the poor ν_τ statistics. AdvSND will reduce the statistical uncertainty to less than 5%, see Table 10. The systematic uncertainty due to the charm quark hadronization fraction into D_s mesons, f_{D_s}, was estimated to be at the 20% level [1]. It can be reduced with measurements performed at the *near* detector, since in its acceptance the different charmed hadron species, including D_s have been identified by the LHCb Collaboration.

Lepton flavour universality can also be tested with the electron to muon neutrino ratio. In this case, charm can be considered also as the source of muon neutrinos if an energy cut is applied. A tentative value of 600 GeV is assumed as the energy threshold in the SND@LHC pseudo-rapidity region, resulting in a 10% accuracy in this ratio for both systematic and statistical uncertainty. The energy threshold in AdvSND can be further optimised in order to have a lower contamination, while reducing the statistical uncertainty down to a few percent. The systematic uncertainty is also expected to be reduced thanks to measurements of the light-meson production yield in the forward region performed by the LHCf Collaboration [41] in Run 3.

4.3.3   Neutrino cross-section

The large neutrino beam energy causes the majority of neutrinos to interact via Deep Inelastic Scattering. DIS neutrino interaction cross-sections have been measured by beam dump experiments at low energies $E_\nu < 350$ GeV [42] and by Ice-Cube at high energies $E_\nu > 6.3$ TeV for muon neutrinos [43].
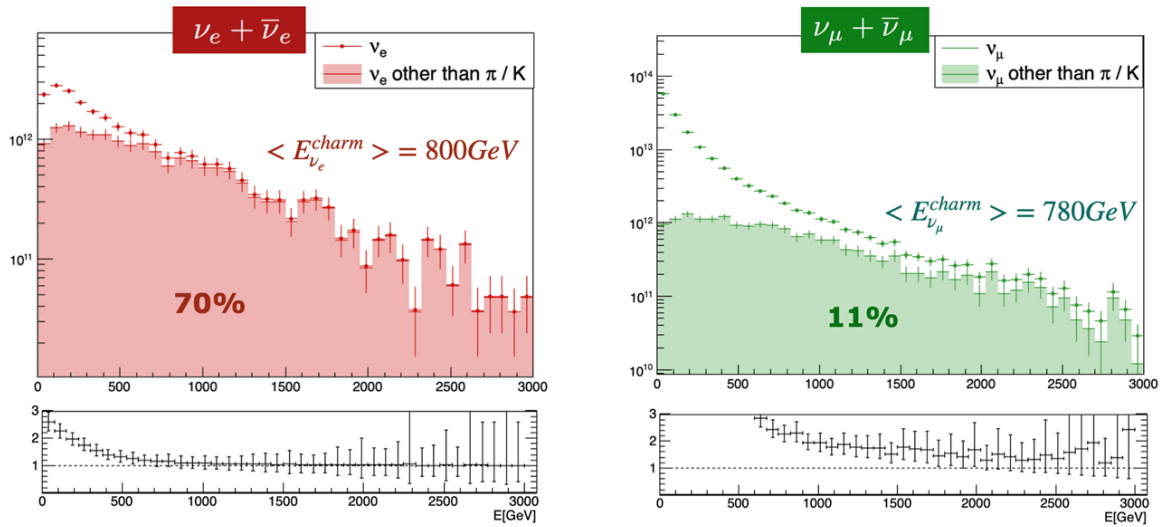
Figure 51: Energy spectrum of muon (Left) and electron (Right) neutrinos and anti-neutrinos in the AdvSND acceptance. Filled areas represent the component coming from charm decays.

AdvSND can perform cross-section measurements in the TeV range with muon neutrinos, with their flux in the forward region known with very good precision thanks to measurements of the light meson production performed in Run 3 by the LHCf Collaboration [41]. The presence of the magnetic spectrometer will allow the charge identification of muons produced in neutrino CC DIS interactions, therefore making it possible to measure neutrino and anti-neutrino cross-sections separately up to 1 TeV. For higher energies, the average neutrino energy will be measured. This is shown in Figure 52, which illustrates the AdvSND capabilities in the measurement of the $\nu_\mu N$ cross section. The reported statistical uncertainties are associated to the neutrino yields in Table 10.

4.3.4 Summary of physics results with neutrinos

Table 11 summarises the main HL-LHC physics objectives with the AdvSND detector in the analyses of neutrino interactions, compared with estimates for the current detector in Run 3. The proposed measurements are reported together with the estimated uncertainties, as described in detail in the corresponding sections.

4.4 Search for Feebly Interacting Particles (FIPs)

Due to its far-forward placement, AdvSND may probe for FIPs produced with large η. Those include the particles originating from proton-proton collisions or in decays of SM particles with a mass of the order of a GeV. Possible signatures may be scatterings off the detector material and decays of unstable particles. Particular examples are dark photons V, light dark matter candidates χ coupled to V, heavy neutral leptons, Higgs-like scalars, and axion-like particles [44].
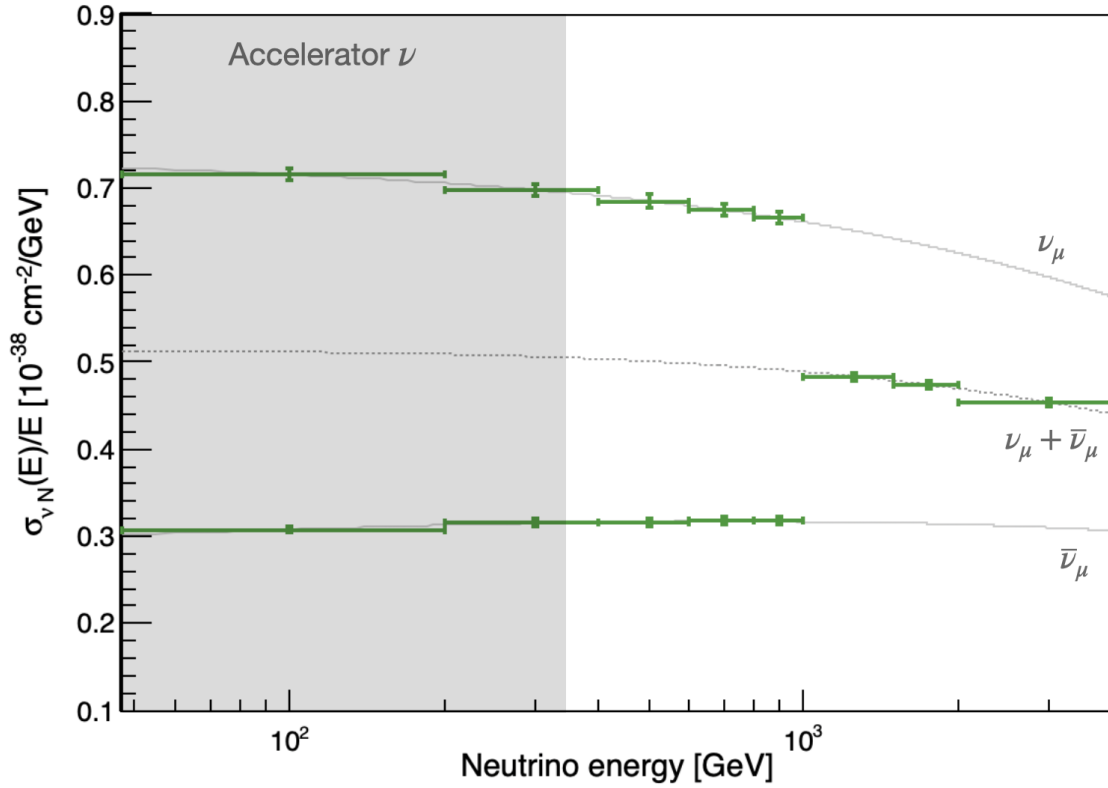
Figure 52: Expected statistical uncertainties for muon neutrino CC DIS cross-section measurements. For energies below 1 TeV AdvSND can distinguish between muon neutrinos antineutrinos. Theoretical predictions are evaluated using GENIE neutrino CC DIS cross-sections on a tungsten Target.

Measurement	Uncertainty		Uncertainty	
	Stat.	Sys.	Stat.	Sys.
Charmed hadron yield	5%	35%	1%	5%
ν_e/ν_τ ratio for LFU test	30%	22%	5%	10%
ν_e/ν_μ ratio for LFU test	10%	10%	1%	5%
ν_μ and $\overline{\nu}_\mu$ cross-section	-	-	1%	5%

Table 11: Measurements proposed by AdvSND in the analyses of neutrino interactions with HL-LHC data compared with estimates for the current detector in Run 3. Statistical and systematic uncertainties are reported.

Considering the decay signature first, the AdvSND experimental setup, while covering a comparable solid angle (Ω) to that of the current detector, it is positioned at a higher η. Since the solid angle distributions of Long-Lived Particles (LLPs) are mostly uniform in the far-forward region, the alignment of AdvSND does not significantly increase the total number of FIPs detected. However, it does influence the energy distribution of the LLPs, resulting in those within AdvSND's angular coverage possessing energies that are 2 to 3 times higher. This characteristic renders AdvSND particularly suited for detecting FIPs with relatively short proper lifetimes ($c\tau \ll 480$ m). The substantial boost these particles receive increases their decay lengths ($c\tau\gamma$), allowing them to potentially reach and decay within the distantly placed AdvSND detector.

Notably, certain FIPs, such as dark photons and $B - L$ mediators, which have lifetimes in this region and are not ruled out by previous experiments, fall within this category [44, 45]. Within the mass range of $m \lesssim 1$ GeV, these particles are chiefly produced through decays of π^0, η mesons, and proton bremsstrahlung, leading to the generation of far-forward particles. Upon reaching the detector, they may decay into either a lepton pair or a collection of hadrons, mirroring the interaction characteristics of ρ^0, ω mesons [46].

The ability of AdvSND to detect these signatures is contingent on multiple factors, including the resolution to distinguish between two tracks with minimal angular separation and the capability to differentiate signals from background noise. Figure 53 illustrates the potential 90% CL sensitivity of AdvSND to these particles, with the same assumptions done in Ref. [47] and the expected HL-LHC integrated luminosity of 3 ab^{-1}.
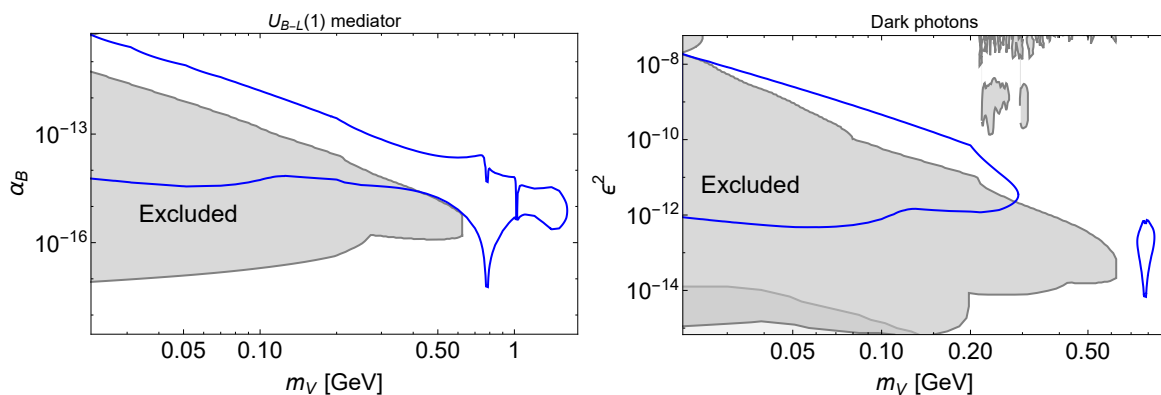

Figure 53: The iso-contours $N_{\text{ev}} = 2.3$, corresponding to 90% CL sensitivity of AdvSND in the HL-LHC (3 ab^{-1}) to decays of dark photons and $B - L$ mediators, computed in the mass-coupling^2 plane. The sensitivity is computed using `SensCalc` package [48] (and references therein). The characteristic feature of the sensitivity region is its enhancement around mass $m \approx 0.77$ GeV (it results in the rapid appearance of the sensitivity to dark photons). It occurs due to a mixing of the mediators with the ρ^0, ω mesons that leads to the resonant enhancement of the production yield around this mass.

Another signature is via scatterings, which become relevant when FIPs are stable. A natural example of such particles are potential dark matter candidates. The same particles as those that may populate the Universe may also be produced at the LHC and then scatter. FIPs may be classified depending on whether they may scatter off electrons. For example, if the particle mediating the scattering is a dark photon, scatterings may be off both electrons and nucleons. If the mediator couples to the baryon current, then only the nucleon scatterings are possible.

The classification is relevant because there are tight constraints on those scattering off electrons coming from lepton colliders and lepton beam dumps (BaBar, Belle, NA64) [47], and it is quite complicated to compete with them, especially in the light of the increased number of collisions. Namely, given the coupling of FIPs to SM particles g, the event rate at these experiments scales as g^2 – one has only to produce the FIP. The event rate with scattering scales as g^4, where an additional g^2 comes from the scattering probability.

Therefore, an attractive opportunity is to explore scatterings via leptophobic mediators. Namely, one may consider a model with a $U_B(1)$ mediator V couples to two particles χ, χ'. The effective Lagrangian takes the form

$$\mathcal{L}_{B,\text{eff}} = g\sqrt{4\pi\alpha_D}V^\mu\chi'^*\partial_\mu\chi + \text{h.c.} + \frac{g}{3}V^\mu \sum_{q=u,d,s,c,b,t} \bar{q}\gamma_\mu q \tag{1}$$

Instead of g, we will refer to $\alpha_B = g^2/4\pi$.

If $m_{\chi'} = m_\chi$, then the model corresponds to elastic dark matter (EDM); otherwise, it is inelastic (IDM). If the masses of the particles belong to the domain $m_\chi + m'_\chi < m_V$ and $\alpha_D \gg \alpha_B$, the production channels of χ, χ' resemble those of the mediator, as the latter, once being produced, immediately decays into $\chi + \chi'$ with unit probability. Two possibilities arise: for the EDM case, one may detect scatterings of χ,

$$\chi + p/n \to \chi + \text{hadrons}, \tag{2}$$

while for the IDM one, it is possible to search for a "double bang" (DB) signature – the χ scattering with subsequent displaced decay of χ' within the detector [49]:

$$\chi + p/n \to \chi' + \text{hadrons}, \quad \chi' \to \chi + \text{hadrons} \tag{3}$$

The pure scattering signature is the increase of the NC/CC ratio above its SM values ≈ 0.3, as the scatterings mimic NC scatterings of neutrino. The DB signature does not have SM analogs (assuming a perfect detection efficiency of the SM processes and also large enough spatial separation) and may be potentially background-free. To detect the DB signature, one would need to relate the two vertices, i.e., to have a detector with local timing capabilities. This is unrealistic in the case of the current detector, but may be possible with AdvSND.

Figure 54 shows the 2σ sensitivity of AdvSND to these signatures. Only inelastic scattering off protons is considered. For the EDM signature, a 10% accuracy in the NC/CC measurement is assumed. For the IDM signature, a minimal energy deposition of 600 MeV is required for the first bang; the minimal/maximal displacements $l_{\text{min/max}}$ are assumed to be between 5 and 15 cm; the lighter particle mass is assumed to be $m_\chi = 20$ MeV, to avoid direct detection constraints on DM for the EDM case that become relevant at masses $\gtrsim 100$ MeV (these bounds are absent in the IDM case [47]), while the marginalization is made over the mass splitting between χ' and χ.

Compared to the sensitivity of the current detector as reported in [47], the sensitivity of the EDM signature of AdvSND would be approximately twice better:

$$\frac{\alpha_{B,\text{lower,AdvSND}}}{\alpha_{B,\text{lower,current detector}}} \approx \sqrt{\frac{\mathcal{L}_{\text{AdvSND}}}{\mathcal{L}_{\text{current detector}}} \cdot \sqrt{\frac{N_{\text{bg,current detector}}}{N_{\text{bg,AdvSND}}}}} \simeq 2 \tag{4}$$
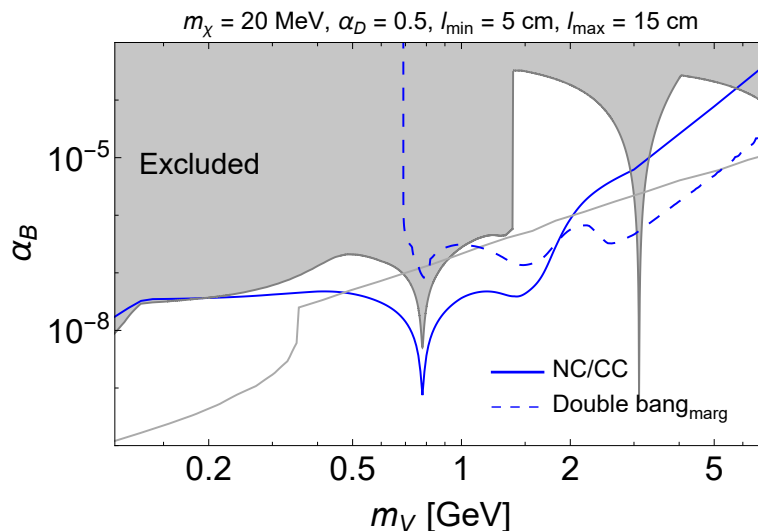
Figure 54: 2σ sensitivity of AdvSND to the models of light dark matter coupled to the baryonic mediator: the elastic DM model (EDM, solid blue), where the signature is an increase of the NC/CC ratio due to scatterings, and the inelastic DM model (IDM, dashed blue), with the signature being "double bang" – a scattering with the subsequent displaced decay. The thermal Target lines are not shown, as they are model-dependent. Namely, they may be easily changed by adding new components that are invisible in laboratory experiments. See text for details. The constraints on the B mediator have been taken from [47] and [50].

Here, $\alpha_{B,\text{lower}}(m_\chi)$ is the minimal value of the coupling that may be probed; $\mathcal{L}$ is the luminosity; N_{bg} is the expected amount of background. To understand the simplicity of the scaling, one needs to consider the expression of the number of scattering events

$$N_{\text{events}} \propto N_{\chi,\text{prod}}\epsilon_{\text{geom}} \int dE_\chi f(E_\chi)\frac{d\sigma_{\text{scatt}}(E_\chi)}{dE_\chi} \tag{5}$$

The total number of produced particles $N_{\chi,\text{prod}}$ scales as $\mathcal{L} \times \alpha_B$; the fraction of χ's flying to the detector, ϵ_{geom}, differs insignificantly due to the fact that the solid angle distribution of χ is almost isotropic in the polar coverage of the current detector and AdvSND; $\frac{d\sigma_{\text{scatt}}(E_\chi)}{dE_\chi} \propto \alpha_B^2$; the energy integral does not significantly depend on the differences of the χ's energy distributions $f(E_\chi)$ in the detector since the χ particles in the directions of the current detector and AdvSND have huge energies far above the threshold of the DIS process.

4.5 Importance of the magnet

The main purpose of the magnetic spectrometer is to measure charge and momentum of the muons produced in neutrino interactions. In doing that, it adds significant value to the physics potential of the experiment. In particular, we highlight the following points:

- The measurement of muon momentum complements the hadronic calorimeter to provide the measurement of the neutrino energy for ν_μ, $\bar{\nu}_\mu$ and ν_τ and $\bar{\nu}_\tau$, when the τ decays into a μ. The importance of measuring the neutrino energy is two-fold: for neutrino-parent identification and cross-section measurements. The ν_μ energy distribution depends strongly on the parent particle. In particular, when the parent is a charmed hadron,

the neutrino spectrum gets much harder, as shown in Figure 51. Energy is a powerful handle to identify the charmed parent and for all the associated QCD measurements. Energy is also important for cross-section measurements: the expected energy dependence is well known and the comparison of measurements with the expectation provides an important test of the Standard Model. This is particularly true for ν_μ, for which a cross section measurement is viable, given that the π production is constrained by the LHCf π^0 measurements.

- Neutrino DIS measurements with AdvSND will have an impact on the parton distributions (PDFs) of protons and heavy nuclei. Recent studies have shown that the explored kinematic region in x and Q^2 overlaps with that of the Electron-Ion Collider, and that a significant reduction of PDF uncertainties can be obtained in particular for the strangeness and the up and down valence PDFs [51]. This work shows that neutrino data improve theoretical predictions for core processes at the HL-LHC, such as Higgs and weak gauge boson production [51]. The measurement of the variables x and Q^2 for ν_μ scattering requires the measurement of the neutrino energy and of the muon momentum. The precision achievable with the designed magnet is sufficient for this kind of measurements.

- The charge identification allows the separation between $\nu_\mu/\bar{\nu}_\mu$ and $\nu_\tau/\bar{\nu}_\tau$ when the τ decays into a muon. This will allow the first direct observation of $\bar{\nu}_\tau$. Moreover, the cross-section measurements of muon neutrinos will profit of the $\nu/\bar{\nu}$ separation. Indeed, the ν_μ deep inelastic neutrino-nucleon cross-section is a factor two larger than for $\bar{\nu}_\mu$. Therefore, the systematic uncertainty of the measurement gets worse when combining $\nu/\bar{\nu}$, thus affecting the quality of the measurements.

- The study of multi-muon events will largely benefit from the charge and momentum measurement of muons. The rate of multi-muon events is much larger than the pile-up in the data currently analysed by the experiment, thus showing a clear physics signal. The study of multi-muon events is sensitive to a large variety of processes. We list here a few examples. Two opposite-sign muons are produced by resonances and therefore their yield constraints the production rate at the IP. A notable example is the $J/\Psi \to \mu^+\mu^-$ which also probes charm production in the same angular region. Another interesting process is the muon trident, i.e. $\mu^\pm N \to \mu^\pm\mu^+\mu^- N$, only measured in the early 1970s [52], with a 10.5 GeV muon beam, as a test of the Fermi statistics, given the presence of two equal-sign muons in the final state. The measurement of the muon energy is important to determine the leading one and study the needed correlations between the opening angles. This process was introduced in GEANT4 [38] only very recently, in 2022.

- The measurement of the muon momentum allows also the sensitivity to exotic physics searches, where muons are produced by new particles, e.g. $\Phi \to \mu^+\mu^-$.

4.6 Beyond Run 4

With this LOI, the SND@LHC Collaboration proposes to extend the physics case of the experiment by running an upgraded version of the detector at the HL-LHC in the same TI18 tunnel. The upgrades to be implemented are meant to improve the detector performance and overcome the geometrical constraints imposed by the tunnel geometry and the sloping floor. The proposed upgrade of the SND@LHC experiment will thus overcome the statistical limitation

of the Run 3 data, thanks to the increased integrated luminosity and to the optimal geometrical configuration. The achieved statistical precision at the end of Run 3 data taking will be such that most of the measurements will be limited by the systematic uncertainties. Charmed hadrons are the parents of all tau neutrinos, most of the electron neutrinos and most of the high-energy muon neutrinos in the angular region we intend to explore. The major source of systematic uncertainty lies in the cross-link between neutrinos and their parent, since there is no measurement of the charm yield in this angular region. The analysis procedure to obtain this cross-link requires different steps and assumptions to be made which limit the achievable precision. The strategy put forward by the Collaboration to overcome this limitation is to foresee a dedicated measurement carried out in an angular region where the charm yield is well constrained by data. Therefore, the Collaboration intends, on a longer time scale, to build a dedicated neutrino detector that will measure all neutrino species in an angular region where LHCb has measured the charm yield. The choice of the LHCb angular region is motivated to have the maximum rapidity available, i.e. the range closest to SND@LHC. Indeed, LHCb has measured the charm yield in $2.0 < \eta < 4.5$. For instance, in the range $4.0 < \eta < 4.5$ LHCb has identified about 180 thousand charmed hadrons [53]. Given that the branching ratio of semi-leptonic decays of charmed hadrons is about 10%, one expect these charmed hadrons to produce in the same angular range about 18000 ν_μs and ν_τs. The experiment aims at detecting about thousand of them for each neutrino species.

Although the measurements will have to cover the LHCb angular region, in order to profit from the high luminosity of proton-proton collisions at IP1 and IP5, the Collaboration has investigated locations around those two IPs, which would allow measurements in the pseudo-rapidity range covered by LHCb. In order to cover a significant part of the azimuthal angle, the location has to be closer to the IP than the current detector in TI18. It turned out that there are two viable options for the installation of such a detector, both around the CMS IP5, the room UJ56 and the alcove UJ57. Preliminary feasibility studies of these two locations including the radiation levels look promising. Table 12 reports the expected statistics we could accumulate in the last runs of LHC (2300 fb^{-1}) assuming a 15 ton neutrino target covering a pseudo-rapidity range $4 < \eta < 4.6$, installed in UJ57.

Given the fact that most of the statistics will be collected after Run 4, the Collaboration has envisaged a staged approach, and the deployment of a neutrino detector in one of these two identified locations is planned for LS4, such that running could start in Run 5. The staged approach allows also a better planning of resources by the Collaboration.

Flavour	ν in acceptance		CC DIS	
	All	not from π/K	All	not from π/K
$\nu_\mu + \bar{\nu}_\mu$	1.6×10^{14}	1.1×10^{13}	1.3×10^{4}	1.0×10^{3}
$\nu_e + \bar{\nu}_e$	1.9×10^{13}	1.2×10^{13}	1.6×10^{3}	1.1×10^{3}
$\nu_\tau + \bar{\nu}_\tau$	1.2×10^{12}	1.2×10^{12}	75	75
Tot	1.8×10^{14}	2.4×10^{13}	1.5×10^{4}	2.2×10^{3}

Table 12: Number of neutrinos in the acceptance of the *near* AdvSND detector and CC DIS interactions assuming $2300\,\mathrm{fb}^{-1}$, as estimated with DPMJET+FLUKA and GENIE generators.

5   Cost

An effort has been made to maximize the re-use of existing components. Our links to the CMS Collaboration allowed to negotiate re-using part of their detectors and of electronic cards which will become available in LS3, including some spare components which will be used for the assembly and operation of prototypes to be exposed to particle beams in 2024. Similarly, we are planning to profit from the existing developments originally dedicated to other LHC experiments and which will become ready on the time scale of the implementation in AdvSND. The in-kind contribution of the CMS silicon modules is equivalent to about 4 MCHF. This value is not included in Table 13 where the cost of the upgraded detector is summarized. The detailed estimation of the cost for each detector component is provided in the corresponding detector subsection. The person-power needed to assemble the proposed detectors is available in the SND@LHC collaboration and will be provided as part of the collaborative effort. We foresee the possibility to further enhance the performance of the detector by adding the new pixel MAPS modules being developed for the ALICE ITS3 upgrade: this option is subject to finding new resources. As mentioned in Section 3 the study of the cost for the civil engineering modifications of the TI18 experimental area is ongoing. We have made the footprint of AdvSND already rather compact, and we are ready to implement suggestions for further optimization coming from the ongoing study by the civil engineering group. We note that the work foreseen in the baseline configuration resembles what was already performed in 2018 in the area of the SPS accelerator dump region and the cost was of ~ 2 MCHF. This may represent a lower bound of the actual cost, given that it was carried out before the pandemic and the access was easier.

	Estimated Cost
Hadron Calorimeter Magnet	200
Detector Magnet	290
Target material (W)	330
Target Silicon Planes readout and services	240
Fast timing layers (RPC)	130
HCAL active detector	35
HCAL readout and power	15
Muon Drift tubes	70
DAQ HW	30
Total for baseline detector	1340

Table 13: Cost estimates in kCHF for the baseline components of the AdvSND. We have listed the most expensive option for the fast timing devices.

6 Comparison with the Run3 configuration

In this Section we summarize the features and performance of the upgraded detector and compare them with the option that the new detector will be installed in the Run3 configuration, i.e. in the same location where the SND@LHC detector is currently taking data, without carrying out any civil engineering work.

The Run3 configuration is affected by geometrical constraints set by the tunnel geometry and the sloping floor as outlined in Section 1. These constraints limit the longitudinal development of the detector as well as its azimuthal angle acceptance in the off-axis location. The transverse location of the upgraded detector in both the baseline and the minimal configuration are optimal for the physics reach of the experiment as the neutrino yield is maximal for both muon neutrinos and for those primarily originated by charmed hadron decays, i.e. electron and tau neutrinos. The optimization of the transverse position has also accounted for the different crossing angle configurations in the HL-LHC. The longitudinal development has been optimized to improve the calorimetric performance of the detector and to add a muon spectrometer for the measurement of the muon charge and momentum.

We have computed the expected yield of neutrino interactions if one would install the detector in the current location, without doing any civil engineering work. Table 14 shows a summary of the comparison, with the key parameters affecting the performance. The upgraded detector will be able to measure the charge and momentum of the muon while this won't be possible with the longitudinal development of the Run3 configuration. Given the additional thickness of the cooling box needed to house the silicon modules, the overall instrumented target mass cannot exceed 600 kg, while it is about 2 tons in the upgraded detector. The expected neutrino yield is estimated to be 6% of the one in the upgraded configuration (see Tab. 10). This reduction factor of ~ 16 comes from two contributions: a factor of 5 from the convolution of the azimuthal angular coverage and of the reduced flux, and a factor of 3.3 from the reduced target mass, due to the reduced longitudinal development of the detector. The costs of the detector in the two scenarios are similar, with the Run3 configuration not fully profiting of the in-kind contribution. Given that the performance would be significantly worse with a comparable effort of the Collaboration, both financially and in terms of person power, and that the Run3 configuration would not allow to fully exploit the in-kind contribution of silicon detectors, the Collaboration does not see this as a viable option.

Detector configuration	Run3	Upgrade
Muon momentum/charge	no	yes
Neutrino target mass	600 kg	2 tons
Neutrino Yield	1.4×10^4	2.3×10^5
Cost (in-kind) (MCHF)	1.05 (~ 4)	1.34 (~ 4)

Table 14: Comparison with the Run3 configuration.

7   Summary

This Letter of Intent outlines the improvements that are proposed to fully exploit the neutrino physics potential of the LHC. The results which will be obtained from Run 3 will provide the first measurement of neutrinos in an unprecedented energy range and will constrain the gluon Parton Distribution Function using neutrinos as a probe of charm production in the unexplored pseudo-rapidity domain. Nevertheless, the measurements from Run 3 will be statistically limited, given the geometrical constraints of the current detector and the expected integrated luminosity. This document presents the upgrade of the SND@LHC detector to exploit this research potential. The factor 5 increase of instantaneous luminosity foreseen by the HL-LHC is incompatible with the usage of the nuclear emulsion films as the high-resolution tracking detector in the neutrino target region and we propose to replace them by silicon trackers. Along with the increase of statistical precision, we propose significant improvements to the experimental setup: a magnetic spectrometer will allow separate identification of neutrino and anti-neutrino interactions for both muon and tau neutrinos. The addition of a magnetic spectrometer will allow the first experimental direct observation and the study of tau anti-neutrinos, while extending the range of flavour conservation tests. It will also extend the reach for the discovery of new exotic phenomena. The Collaboration is committed to the investment needed to upgrade the detector. The main requirement is to make the TI18 experimental area suitable to host the upgraded experiment. The floor needs to be modified to enhance the acceptance of the detector, also in view of the possible changes in the beam crossing angles, while the enlargement of the tunnel is needed to accommodate the magnetic spectrometer. Although our studies have so far not revealed any show stopper, the enlargement of the tunnel and related issues are currently under further investigation. The option of installing the upgraded detector in the current geometrical configuration, without performing any civil engineering work, was also examined but the expected performance of this configuration did not match the experimental effort required.

8   Acknowledgements

References

[1] **SNDLHC** Collaboration, C. Ahdida et al., *SND@LHC - Scattering and Neutrino Detector at the LHC*, Technical Proposal CERN-LHCC-2021-003, LHCC-P-016, CERN, Geneva, 2021.

[2] **SND@LHC** Collaboration, G. Acampora et al., *SND@LHC: The Scattering and Neutrino Detector at the LHC*, [arXiv:2210.02784].

[3] **SND@LHC** Collaboration, R. Albanese et al., *Observation of collider muon neutrinos with the SND@LHC experiment*, *Phys. Rev. Lett.* **131** (2023), no. 3 031802, [arXiv:2305.09383].

[4] **SND@LHC** Collaboration, R. Albanese et al., *Measurement of the muon flux at the SND@LHC experiment*, [arXiv:2310.05536].

[5] **SNDLHC** Collaboration, T. Ruf, *Estimate of the Veto System Inefficiency*, Internal Note SNDLHC-INT-2023-002, CERN, 2023.

[6] "MOU with CMS tracker approved by CMS Collaboration Board, being published."

[7] T. Schlatter et al., *Genfit/genfit: release-02-00-05*, .

[8] F. Powolny, *Characterization of time resolved photodetector systems for Positron Emission Tomography.* PhD thesis, Université de Neuchatel, Switzerland, May, 2009.

[9] P. Lecoq et al., *Factors influencing time resolution of scintillators and ways to improve them*, in *Nuclear Science Symposium Conference Record (NSS/MIC), 2009 IEEE*, pp. 1880–1885, IEEE, October, 2009.

[10] D. Perez-Benito, R. Chil, L. A. Hidalgo-Torres, and J. J. Vaquero, *Scintillator geometrical considerations for detectors based on hexagonal sipms*, *IEEE Transactions on Radiation and Plasma Medical Sciences* **7** (2023), no. 7 684–691.

[11] E. Albuquerque, R. Bugalho, V. Dubceac, L. Ferramacho, H. França, M. Firlej, T. Fiutowski, M. Gallinaro, M. Idzik, J. Moron, T. Niknejad, L. Oliveira, R. Francisco, J. C. Silva, R. Silva, M. Silveira, K. Swientek, and J. Varela, *Tofhir2: The readout asic of the cms barrel mip timing detector*, in *2020 IEEE Nuclear Science Symposium and Medical Imaging Conference (NSS/MIC)*, pp. 1–7, 2020.

[12] C. Betancourt, A. Korzenev, P. Mermod, and N. Serra, *A prototype for the ship timing detector*, *Nuclear Instruments and Methods in Physics Research Section A: Accelerators, Spectrometers, Detectors and Associated Equipment* **979** (2020) 164398.

[13] A. Korzenev, F. Barao, S. Bordoni, D. Breton, F. Cadoux, Y. Favre, M. Khabibullin, A. Khotyantsev, Y. Kudenko, T. Lux, J. Maalmi, P. Mermod, O. Mineev, and F. Sanchez, *A 4π time-of-flight detector for the nd280/t2k upgrade*, *Journal of Instrumentation* **17** (jan, 2022) P01016.

[14] C. Betancourt et al., *Application of large area SiPMs for the readout of a plastic scintillator based timing detector*, *JINST* **12** (2017), no. 11 P11023, [arXiv:1709.08972].

[15] P. Fonte, R. Ferreira Marques, J. Pinhão, N. Carolino, and A. Policarpo, *High-resolution rpcs for large tof systems*, Nuclear Instruments and Methods in Physics Research Section A: Accelerators, Spectrometers, Detectors and Associated Equipment **449** (2000), no. 1 295–301.

[16] A. Blanco, F. Clemencio, P. Fonte, C. Franco, N. Leonardo, L. Lopes, C. Loureiro, J. Saraiva, and G. Soares, *The ship timing detector based on mrpc*, Journal of Instrumentation **15** (oct, 2020) C10017.

[17] F. Carnesecchi, *Performance of the ALICE time-of-flight detector at the LHC*, Journal of Instrumentation **14** (jun, 2019) C06023–C06023.

[18] D. Belver, P. Cabanelas, E. Castro, J. A. Garzon, A. Gil, D. Gonzalez-Diaz, W. Koenig, and M. Traxler, *Performance of the low-jitter high-gain/bandwidth front-end electronics of the hades trpc wall*, IEEE Transactions on Nuclear Science **57** (Oct, 2010) 2848–2856.

[19] A. Blanco, P. Fonte, L. Lopes, and M. Pimenta, *Sealed (zero gas flow) resistive plate chambers*, The European Physical Journal Plus **138** (Nov, 2023) 1021.

[20] G. Garillot, Y. Baek, D. Hatzifotiadou, D. Kim, J. Kim, B. Min, S. Park, M. Williams, and R. Zuyeuski, *Operation of a low resistivity glass mrpc at high rate using ecological gas*, Nuclear Instruments and Methods in Physics Research Section A: Accelerators, Spectrometers, Detectors and Associated Equipment **1061** (2024) 169104.

[21] A. Neiser, J. Adamczewski-Musch, M. Hoek, W. Koenig, G. Korcyl, S. Linev, L. Maier, J. Michel, M. Palka, M. Penschuck, M. Traxler, C. Uğur, and A. Zink, *TRB3: a 264 channel high precision TDC platform and its applications*, Journal of Instrumentation **8** (dec, 2013) C12043–C12043.

[22] **NA64** Collaboration, D. "Banerjee and others", *Hcal detector description*, Tech. Rep. https://na64.web.cern.ch/node/20, CERN, 2017.

[23] **CMS** Collaboration, S. Chatrchyan et al., *The CMS experiment at the CERN LHC*, Journal of Instrumentation **3** (aug, 2008) S08004.

[24] **CMS** Collaboration, S. Chatrchyan et al., *Performance of the CMS drift tube chambers with cosmic rays*, Journal of Instrumentation **5** (mar, 2010) T03015.

[25] N. Amapane et al., *Study of muon pair production from positron annihilation at threshold energy*, Journal of Instrumentation **15** (jan, 2020) P01036.

[26] M. Migliorini, J. Pazzini, A. Triossi, M. Zanetti, and A. Zucchetta, *Muon trigger with fast Neural Networks on FPGA, a demonstrator*, Journal of Physics: Conference Series **2374** (nov, 2022) 012099.

[27] G. Paggi, *Construction and test of a cosmic ray telescope based on CMS Drift Tube chambers and data acquisition prototypes of the Phase-2 upgrade*. PhD thesis, Universita degli Studi Bologna, 2022.

[28] **CMS** Collaboration, A. Sirunyan et al., *Performance of the CMS muon detector and muon reconstruction with proton-proton collisions at $\sqrt{s}$=13 TeV*, *Journal of Instrumentation* **13** (jun, 2018) P06015.

[29] J. Sastre, C. F. Bedoya, S. Cuadrado, J. Cuchillo, D. Francia, C. de Lara, A. Navarro, R. Paz, I. Redondo, and D. Redondo, *The OBDT-theta board: time digitization for the theta view of Drift Tubes chambers*, 2024. [`arXiv:2401.03818`].

[30] **SND@LHC** Collaboration, M. De Magistris et al., *An integrated iron core conical flux-symmetric spectrometer-system for the SND@LHC upgrade*, *To be submitted to Journal of Instrumentation* (2024).

[31] **SHiP** Collaboration, C. Ahdida et al., *The Magnet of the Scattering and Neutrino Detector for the SHiP experiment at CERN*, *JINST* **15** (2020), no. 01 P01027, [`arXiv:1910.02952`].

[32] M. A. Green et al., *Cost optimization of MSU conventional room temperature magnets as a function of magnet conductor current density*, *IEEE Transactions on Applied Superconductivity* **22** (2012), no. 3 4002504–4002504.

[33] M. Al-Turany, D. Bertini, R. Karabowicz, D. Kresan, P. Malzacher, T. Stockmanns, and F. Uhlig, *The FairRoot framework*, *J. Phys. Conf. Ser.* **396** (2012) 022001.

[34] S. Roesler, R. Engel, and J. Ranft, *The Monte Carlo event generator DPMJET-III*, in *Advanced Monte Carlo for radiation physics, particle transport simulation and applications. Proceedings, Conference, MC2000, Lisbon, Portugal, October 23-26, 2000*, p. 1033, 2000. [`hep-ph/0012252`].

[35] A. Ferrari, P. R. Sala, A. Fasso, and J. Ranft, *FLUKA: A multi-particle transport code (Program version 2005)*, Tech. Rep. CERN-2005-010, SLAC-R-773, INFN-TC-05-11, CERN, INFN, 2005.

[36] T. T. Böhlen, F. Cerutti, M. P. W. Chin, A. Fassò, A. Ferrari, P. G. Ortega, A. Mairani, P. R. Sala, G. Smirnov, and V. Vlachoudis, *The FLUKA Code: Developments and Challenges for High Energy and Medical Applications*, *Nucl. Data Sheets* **120** (2014) 211.

[37] C. Andreopoulos et al., *The GENIE Neutrino Monte Carlo Generator*, *Nucl. Instrum. Meth. A* **614** (2010) 87, [`arXiv:0905.2517`].

[38] **GEANT4** Collaboration, S. Agostinelli et al., *GEANT4: A Simulation toolkit*, *Nucl. Instrum. Meth. A* **506** (2003) 250.

[39] T. Sjöstrand, S. Mrenna, and P. Z. Skands, *A brief introduction to PYTHIA 8.1*, *Comput. Phys. Commun.* **178** (2008) 852, [`arXiv:0710.3820`].

[40] **LHCb** Collaboration, R. Aaij et al., *Measurements of prompt charm production cross-sections in pp collisions at $\sqrt{s} = 5$ TeV*, *JHEP* **06** (2017) 147, [`arXiv:1610.02230`].

[41] **LHCf** Collaboration, O. Adriani et al., *Measurement of forward neutral pion transverse momentum spectra for $\sqrt{s} = 7 TeV$ proton-proton collisions at LHC*, *Phys. Rev. D* **86** (2012) 092001, [`arXiv:1205.4578`].

[42] **Particle Data Group** Collaboration, P. A. Zyla et al., *Review of Particle Physics*, *PTEP* **2020** (2020), no. 8 083C01.

[43] **IceCube** Collaboration, M. G. Aartsen et al., *Measurement of the multi-TeV neutrino cross section with IceCube using Earth absorption*, *Nature* **551** (2017) 596–600, [arXiv:1711.08119].

[44] J. Beacham et al., *Physics Beyond Colliders at CERN: Beyond the Standard Model Working Group Report*, *J. Phys. G* **47** (2020), no. 1 010501, [arXiv:1901.09966].

[45] T. Felkl, T. Li, J. Liao, and M. A. Schmidt, *Probing general U(1)' models with non-universal lepton charges at FASER/FASER2, COHERENT and long-baseline oscillation experiments*, *JHEP* **09** (2023) 168, [arXiv:2306.09569].

[46] P. Ilten, Y. Soreq, M. Williams, and W. Xue, *Serendipity in dark photon searches*, *JHEP* **06** (2018) 004, [arXiv:1801.04847].

[47] A. Boyarsky, O. Mikulenko, M. Ovchynnikov, and L. Shchutska, *Searches for new physics at SND@LHC*, *JHEP* **03** (2022) 006, [arXiv:2104.09688].

[48] M. Ovchynnikov, J.-L. Tastet, O. Mikulenko, and K. Bondarenko, *Sensitivities to feebly interacting particles: public and unified calculations*, *Phys. Rev. D* **108** (2023), no. 7 075028, [arXiv:2305.13383].

[49] M. Ferrillo, M. Ovchynnikov, F. Resnati, and A. De Roeck, *Improving the potential of BDF@SPS to search for new physics with liquid argon time projection chambers*, [arXiv:2312.14868].

[50] B. Batell, J. L. Feng, M. Fieg, A. Ismail, F. Kling, R. M. Abraham, and S. Trojanowski, *Hadrophilic dark sectors at the Forward Physics Facility*, *Phys. Rev. D* **105** (2022), no. 7 075001, [arXiv:2111.10343].

[51] J. M. Cruz-Martinez, M. Fieg, T. Giani, P. Krack, T. Mäkelä, T. Rabemananjara, and J. Rojo, *The LHC as a Neutrino-Ion Collider*, [arXiv:2309.09581].

[52] J. J. Russell, R. C. Sah, M. J. Tannenbaum, W. E. Cleland, D. G. Ryan, and D. G. Stairs, *Observation of muon trident production in lead and the statistics of the muon*, *Phys. Rev. Lett.* **26** (1971) 46–50.

[53] **LHCb** Collaboration, R. Aaij et al., *Measurements of prompt charm production cross-sections in pp collisions at $\sqrt{s} = 13$ TeV*, *JHEP* **03** (2016) 159, [arXiv:1510.01707]. [Erratum: JHEP 09, 013 (2016), Erratum: JHEP 05, 074 (2017)].